› Shifted Analyzing Plane: Field optimization for background reduction of the KATRIN experiment

Master‘s thesis
Benedikt Bieringer

First referee: Prof. Dr. C. Weinheimer
Second referee: Prof. Dr. A. Andronic

Westfälische Wilhelms-Universität Münster
Institut für Kernphysik
AG Prof. Dr. C. Weinheimer

Münster, October 2020

Declaration of Academic Integrity[1]

I hereby confirm that this thesis on “Shifted Analyzing Plane: Field optimization for background reduction of the KATRIN experiment” is solely my own work and that I have used no sources or aids other than the ones stated. All passages in my thesis for which other sources, including electronic media, have been used, be it direct quotes or content references, have been acknowledged as such and the sources cited.

(date and signature of student)

I agree to have my thesis checked in order to rule out potential similarities with other works and to have my thesis stored in a database for this purpose.

(date and signature of student)

---

[1] As found on `https://www.uni-muenster.de/imperia/md/content/math_nat_fakultaet/pruefungsamt/pruefungsamt_neu/allgemein/plagiatserkl__rung_englisch.docx`

The title page layout is adapted from an internal corporate design template of the University of Münster.

Contents

1 Introduction

Since its experimental detection in 1956 [Cow+56], the electron antineutrino has become an important observable particle in various fields, especially prominent being the recent use of neutrino detection in the context of multi-messenger astronomy. In 2015, the Nobel prize in physics was awarded to T. Kajita and A.B. McDonald for the observation of neutrino oscillation [Nob1515], implying a non-zero mass of neutrino particles. Despite their direct and indirect study in numerous experiments, e.g. as part of observed decays including neutrinos in particle accelerators, the absolute mass of the neutrino particles has yet to be determined.

The ***Ka****rlsruhe* ***Tri****tium* ***N****eutrino* experiment (KATRIN) aims at the detection or constraint on the upper limit of the electron antineutrino mass with an unprecedented sensitivity of 0.2 eV at 90 % confidence limit, and recently published the currently best constraint on the electron antineutrino mass of 1.1 eV at 90 % Confidence Limit[Ake+19]. For this, it performs integral spectroscopy on the electron endpoint region of tritium β^- decay.

To reach its specified sensitivity, a low and well understood background from electrons and detector noise, designed to be in the order of 10 mcps [KAT05], is needed. Background measurements in the implemented KATRIN setup with e.g. a recently measured background of (293 ± 1) mcps [Ake+19] during neutrino mass measurements pose the challenge of further background reduction. The most significant background component is introduced by the *main spectrometer* (MS) of*magnetic adiabatic collimator combined with an electrostatic filter* (MAC-E filter) type, which allows the integral electron spectroscopy by rejecting electrons with energies below a tunable energy using an electrostatic filter barrier. The *Shifted Analyzing Plane* (SAP) approach poses a key concept in reduction of MS induced background that utilizes the flexibility of the available spectrometer hardware to shape electric and magnetic fields inside the MS.

The thesis at hand aims at the optimization of electromagnetic fields in the spectrometer with the SAP method and it uses the variety of measured MS field settings to build background models in both physics and data-driven approaches. In the following, Chapter 2 guides the reader through the KATRIN experiment and its context in the landscape of past and present neutrino mass experiments. After this general overview, Chapter 3 introduces the current background model of the experiment. Chapter 4 then discusses the SAP method amongst further, currently investigated background reduction methods. For the implementation of SAP, Chapter 5 presents various new and extended simulation tools. With this tooling at hand, Chapter 6 provides the approach of generating settings for general MAC-E filters and employs it in the use of SAP optimizations. Measurements performed with these settings then allow for diverse background analysis results shown and discussed in Chapter 7. Using the gained knowledge and existing model assumptions, Chapter 8 follows with new background models assuming both low and high background electron starting energies. Finally, Chapter 9 concludes with an outlook.

2 The KATRIN experiment

The ***Ka****rlsruhe* ***Tri****tium* ***N****eutrino* experiment (KATRIN) is a setup aiming at a measurement of the electron antineutrino mass $m_{\overline{\nu}_e}$ to an unprecedented sensitivity of $0.2\,\mathrm{eV}$ at 90% CL by spectroscopy of the Tritium β^- decay electron endpoint. In case of a measured mass signal, a discovery potential (5σ) is reached for $m_{\overline{\nu}_e} = 0.35\,\mathrm{eV/c^2}$. To accomplish its sensitivity, the KATRIN experiment will perform tritium measurements for an accumulated time of 3 years, with maintenance and calibration phases in between [KAT05]. This section presents the KATRIN experiment from its origin and overall setup to one of its main principles, the electron spectroscopy using MAC-E filters.

The KATRIN experiment originates in the history of neutrino experiments and especially neutrino mass searches, briefly introduced in Section 2.1. The experimental setup of the electron beamline is then presented in Section 2.2. As especially relevant component for both the high signal rate and the high energy resolution of the KATRIN experiment, the detailed MAC-E filter principle for electron spectroscopy is lastly explained in Section 2.3.

2.1 History of neutrino mass experiments

The existence of the neutrino was first suggested by W. Pauli via letter in 1930 [Pau30] to explain the observed continuity of β decay energy spectra. Its experimental detection was then published by C. Cowan, Jr. and F. Reines among others in 1956 [Cow+56], with results from a liquid scintillator experiment using both a light and heavy water solution to observe inverse beta decay:

$$\overline{\nu}_\mu + \mathrm{p} \rightarrow \mathrm{e}^+ + \mathrm{n}\,.$$

where measurable photons are produced by the positron annihilation and the neutron capture in cadmium from dissolved cadmium chloride.

This gave rise to a variety of neutrino experiments, both with artificial and natural neutrino sources. Two experiments by the Brookhaven National Laboratory shall be noted here:

First, the discovery of the muon neutrino was achieved by L. Lederman, M. Schwartz and J. Steinberger in 1962 with the decay

$$\pi^{\pm} \rightarrow \mu^{\pm} + (\nu_{\mu}/\overline{\nu}_{\mu})$$

of pions produced at a synchrotron ring and muons detected in a spark chamber [Dan+62]. Second, J. Bahcall and R. Davis, Jr. determined a solar neutrino flux by counting the amount of ^{37}Ar generated via the neutrino capture

$$\nu + {}^{37}\mathrm{Cl} \rightarrow {}^{37}\mathrm{Ar} + e^{-} \ ,$$

with a count rate significantly lower than expected from theory [BD76].

The neutrino masses were found to be non-zero through the explanation of this finding by the discovery of neutrino oscillation, a concept suggested by B. Pontecorvo in 1957 [Pon57]. It was experimentally observed in multiple experiments such as 1998 by the Super-Kamiokande Collaboration [Fuk+98], using a water Cherenkov detector for differentiable detection of atmospheric electron and muon neutrinos, and 2001 by the SNO Collaboration [Ahm+01], using a heavy water Cherenkov detector for a direct measurement of solar neutrino oscillation.

In theory, the neutrino oscillation arises from identifying the three flavor neutrinos ν_{e}, ν_{μ} and ν_{τ} as superposition of three neutrino mass eigenstates. Conventionally, the neutrino mass eigenstates m_i, $i \in 1, 2, 3$ are arranged according to their amount of electron flavor in descending order [Aar+20]. The mixing of the mass eigenstates in the flavor eigenstates is described by the PMNS matrix U that was presented in 1962 by and named after Z. Maki, M. Nakagawa and S. Sakata in [MNS62], further named after B. Pontecorvo for his conceptual groundwork. The PMNS matrix elements U_{ij} and differences of the neutrino mass eigenstates can be determined from observation of neutrino oscillation for measurements with different distances from neutrino sources such as decays in the Sun, atmosphere, reactors and accelerators. This analysis currently allows two possible orderings of neutrino mass eigenstates: Either so-called *Normal Ordering* where $m_1 < m_2 < m_3$ or so-called *Inverted Ordering* with $m_3 < m_1 < m_2$. In both cases, the mass difference of the lightest and heaviest mass eigenstate is constrained to be in the order of $10^{-3}\,\mathrm{eV}$. For a more detailed aggregation of results from a combined analysis of given neutrino oscillation experiments, the reader is referred to [Tan+18, chapter 14.7].

Different experiments are also sensitive to absolute neutrino masses. In cosmology, assuming the ΛCDM model, the absolute sum of neutrino masses $\sum_i m_i$ can be confined to $< 0.59\,\mathrm{eV}$ at $95\%\,\mathrm{CL}$, and including further observed properties such as the growth rate of large scale structures, this limit can be improved up to $< 0.12\,\mathrm{eV}$ at 95% CL with the right choice of observables. ΛCDM is sensitive to the given absolute sum of neutrino masses as the abundance of the different neutrino mass eigenstates is assumed to be equal in these observables. These results can be found alongside further discussion in [Tan+18, chapter 25].

If neutrinos are Majorana particles, meaning if they are their own anti-particles, two beta decays could happen simultaneously as one neutrinoless double beta decay [Tan+18, chapter 62]. A measured rate of the $0\nu\beta\beta$ decay would allow to determine the product of squares of the effective Majorana mass $\langle m_{\beta\beta}\rangle = |\sum_i U_{ei}^2 m_i|$, the nuclear matrix element and the decay phase space. The latter two parameters can be calculated from theory, although the nuclear matrix element introduces uncertainty. Knowledge of the effective Majorana mass could potentially determine neutrino masses and hierarchy.

Direct neutrino mass measurements are significantly less model dependent than estimates from cosmology and $0\nu\beta\beta$ searches. A model-independent determination of the absolute neutrino mass would therefore also provide important input for model testing in the fields of cosmology and the possible ranges of Majorana masses. The general approach for direct observation of the neutrino mass is the measurement of decay energy spectra, utilizing the imprint of the neutrino mass, approximately described by the incoherent sum over the neutrino mass eigenstates weighted by the mixing of the neutrino involved. In case of electron neutrinos or anti-neutrinos, these decays are β decay or electron capture, with the neutrino mass $m_{\nu_e} = (\sum_i |U_{ei}|^2 m_i^2)^{1/2}$ [FS03].

Here, three types of experiments can be distinguished:

1) MAC-E filter type experiments such as *KATRIN* perform integral spectroscopy on energies of electrons released during a β^- decay. Its predecessors were experiments from *Mainz*, lending an upper limit on $m_{\overline{\nu}_e}$ of $2.3\,\mathrm{eV}$ at 95% CL [Kra+05], and *Troitsk*, lending an upper limit of $2.05\,\mathrm{eV}$ at 95% CL [Ase+11]. The KATRIN collaboration recently published a limit of $1.1\,\mathrm{eV}$ at 90% CL [Ake+19].

2) Calorimetry-based experiments absorb decay products – except neutrinos – directly at the emitter material, measuring their total energy through the temperature increase of the detector material. The current upper limit on $m_{\overline{\nu}_e}$ using this technology is $21.7\,\mathrm{eV}$ at 90% CL as published in 2003 [Arn+03].

3) With *Project 8*, a new measurement type is now researched, performing energy spectroscopy via measurement of the cyclotron frequency of decay electrons in a magnetic field [Esf+17].

For an extended description of these experiments, the reader is referred to [For14]. A summary on neutrino mass limits for all flavours can be found in [Tan+18, p. 1006ff].

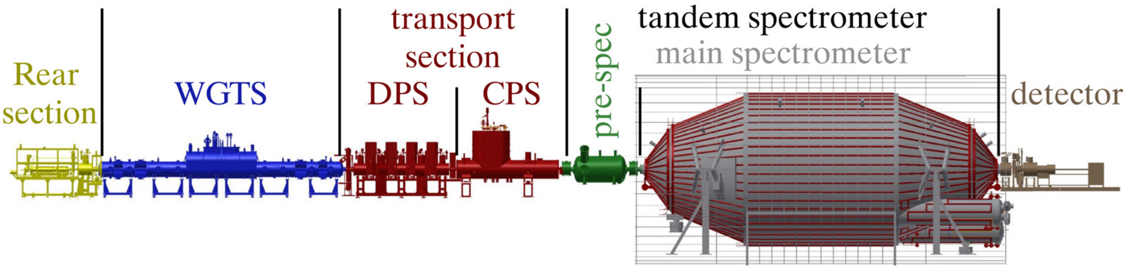

Figure 2.1: Overview of the KATRIN experimental setup. Depicted are the *Rear Section* (RS) as part of the *Control and Monitoring System* (CMS), the *Windowless Gaseous Tritium Source* (WGTS), *Differential* and *Cryogenic Pumping Sections* (DPS, CPS), the *Pre-Spectrometer* (PS) followed by the *Main Spectrometer* (MS) and finally the *DETector section* (DET). Figure from [Sch16, p. 32, fig. 2.5].

2.2 KATRIN beamline

The KATRIN experiment is a tritium decay spectroscopy experiment using a windowless gaseous tritium source for high luminosity and two MAC-E filters for high energy resolution [KAT05]. The experimental setup enclosing the 70 m long electron beamline can be seen in Fig. 2.1. A guiding fluxtube is shaped by superconducting magnets, adiabatically guiding electrons throughout the experiment in near independency of their emission angles. These magnets and designed magnetic field strengths throughout the experiment can be seen in Fig. 2.2.

In the following, the main components of the KATRIN beamline are described.

The *rear section* (RS) contains several calibration instruments and closes the rear (upstream) side of the tritium source in form of a golden *rear wall* (RW). Through a coverable hole at the rear wall center, monoenergetic photoelectrons can be introduced by the *electron gun* (E-Gun) [Beh+17], surrounded by a tunable superconducting magnet setup to steer electron beams to specific parts of the fluxtube. Further, electric potentials can be applied to the rear wall to couple with the charged plasma from the tritium source and it can be illuminated with a UV-C lamp setup [Sch16; Bie17].

The *windowless gaseous tritium source* (WGTS) provides electrons from tritium β^- decay at a rate of approximately 10^{10} electrons per second.It provides a stabilized temperature at 30 K and 100 K, allowing for regular operation with tritium and calibration modes with gaseous $^{83\mathrm{m}}$Kr, which can also be combined with tritium [HK17]. Electrons start in a magnetic field of $B_{\mathrm{WGTS}} = 2.52\,\mathrm{T}$ and an electric potential of 0 V [Kle+19].

Electrons starting in the WGTS are bound to follow magnetic field lines, either towards the rear wall – a direction commonly called “upstream” – or towards the *differential* and *cryogenic pumping section* (DPS and CPS) – named “downstream”. In this area, the tritium

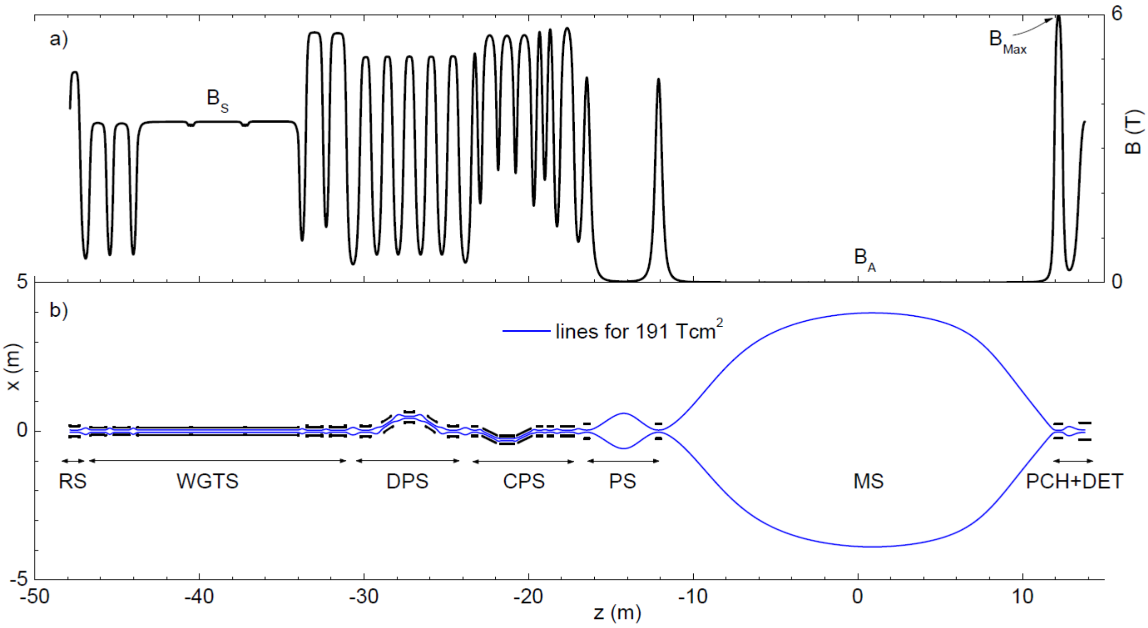

Figure 2.2: Magnetic fields inside the KATRIN fluxtube. a) Nominal fields at fluxtube center. b) Outer fluxtube and superconducting magnets of the entire beamline. Both simulations show the nominal field at 100 % magnetic field strength. Figure published under license [CC BY 3.0] in [Are+18, p. 7, fig. 3].

flow from the WGTS is reduced by more than 14 orders of magnitude, using two mechanisms: In the DPS, electrons are guided through a chicane-shaped beamtube, while tritium and ions hit walls of turbo molecular pumps. The first chicane pieces are part of the WGTS at both sides, namely DPS1-R at the rear end and DPS1-F at the front end. While DPS1-F is already retaining two orders of magnitude of tritium flow, the further DPS chicanes allow for additional 5 orders of magnitude of flow reduction. The tritium flux is suppressed by additional 7 orders of magnitude by the CPS using cryosorption in the form of adsorption of tritium on argon frost as adsorbent [Jan15].

The downstream side of the CPS houses an additional electron source: The *condensed krypton source* (CKrS) allows for a fast and precise energy calibration of the following spectrometers using conversion electrons from condensed $^{83\mathrm{m}}$Kr. While not in use, it is parked outside the beamtube [Bot12; FUL18].

In the same beamline segment, the *forward beam monitor* (FBM) [Ell19] is installed. It allows precise monitoring of electron flux from the source to the permille level, and is inserted into the outer region of the fluxtube for this task.

The remaining electrons pass through two spectrometers, namely the *pre-* and *main spectrometer* (PS, MS). Both are high-pass energy filters of MAC-E filter type, a principle that will be further elaborated in the next section. The PS is designed to filter electrons with a retarding potential 300 eV below the tritium electron endpoint, reducing the flux of non-relevant electrons entering the MS by 6 orders of magnitude. This lowers the amount of electrons ionizing residual molecules inside the MS [KAT05].

The iconic MS vessel – itself 23.3 m long with an inner diameter of 9.8 m – is then used to filter tritium electron energies around their endpoint [Val09]. Its setup will be described further in Section 2.3.4 and its contribution to measurement background will be introduced in Chapter 3.

Both MS and PS require high electric potentials with ground potential in between, which combined with the guiding magnetic field lines effectively creates a Penning trap in between the spectrometer vessels. This can lead to an accumulation of electrons from background and energy loss processes that can both leak towards the spectrometer and pose danger in form of a discharge. This is avoided by bent Inconel rods that, when triggered, wipe through the fluxtube to collect accumulated electrons [Ake+20].

As last section in the KATRIN beamline, electrons are guided towards the detector section, consisting of first the so-called *pinch magnet* (PCH), using a high magnetic field of e.g. $B_{\text{max}} = 4.24\,\text{T}$ [Ake+19] in recent measurement campaigns, magnetically reflecting electrons with large angles, as they are prone to higher energy loss arising from their larger cyclotron radii and therefore larger path lengths [Mer12].

After the PCH magnet, the *precision ultra-low current integrating normalization electrometer for low-level analysis* (PULCINELLA) is an electrometer measuring electrons emitted from an illuminated titanium disc that can be inserted to cover the entire fluxtube. This allows to calibrate the detector using the same illuminated titanium disc after its flux is measured with PULCINELLA [Har12].

Next, the *post-acceleration* electrode (PAE) [Mer12] accelerates electrons further towards the detector, increasing the electron energy over flourescence background and lowering the incidence angle of electrons on the following detector. Although the PAE can provide up to 30 kV of potential positive to ground, more than 12 kV could lead to Penning discharges of a trap expected outside the beamtube [Cor14]. In recent measurement campaigns, a 10 kV positive potential is used [Ake+19].

The *focal-plane detector* (FPD) then collects remaining electrons on 148 equiareal pixels arranged as segments of 13 rings with a total diameter of 90 mm in a magnetic field similar to the source field. Using a smaller magnetic field than at the PCH reduces the maximal incidence angle of electrons on the FPD wafer, effectively reducing backscattering. [Ams+15]

Additionally, the KATRIN experiment is equipped with a high amount of further custom-built measurement and control components such as a voltage monitoring setup featuring an

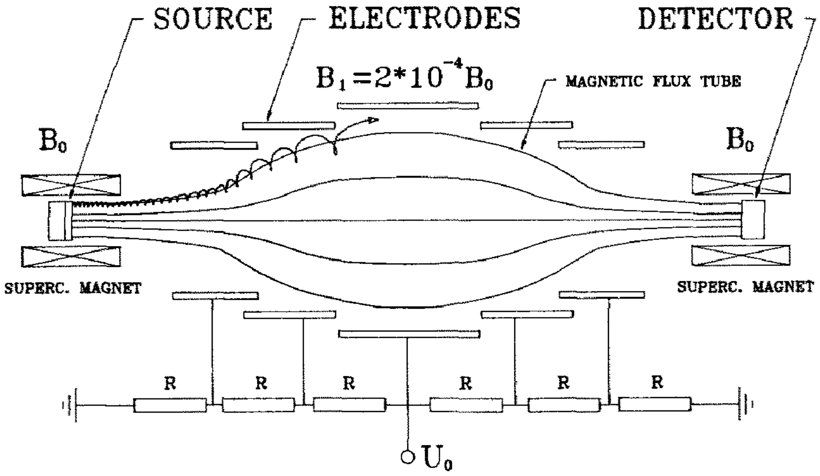

Figure 2.3: Principle of the initial MAC-E filter used in Mainz. Electrodes shape the filtering electric potential barrier inside the spectrometer while the low magnetic field inside the spectrometer collimates the electron angles in a beam emitted from a frozen tritium source. Figure from [Pic+92, p. 346, fig. 1].

additional spectrometer setup and a high-precision voltage divider, a laser raman spectroscopy unit for tritium purity measurement and mobile magnetic sensor units to measure magnetic fields around the main spectrometer. This is complemented with further individual sensors, tracking e.g. temperature and air humidity.

2.3 MAC-E filter principle

The KATRIN beamline features two MAC-E filters, *magnetic adiabatic collimators combined with electrostatic filters*, allowing for precise high-pass filtering of electron energies while maintaining a high angular acceptance. With a working principle first established 1975 in [HH76], the MAC-E filter concept was first connected to neutrino mass measurements in [LS85] with a spectrometer vessel setup that is nowadays iconic for MAC-E filter type experiments. Exemplarily, in Fig. 2.3 the initial Mainz spectrometer setup is pictured.

To discuss the working principle of MAC-E filters, first the condition for transmission of electrons is presented in Section 2.3.1. It is followed by the transmission function, explained in Section 2.3.2. Especially, the concept of an analyzing plane will become of importance, which is therefore elaborated in Section 2.3.3. MAC-E filters occur twice in the main KATRIN beamline (PS and MS) and once in the voltage monitoring system. While Section 2.3.4 focusses on the main spectrometer, the general working principles presented here apply to all spectrometers of MAC-E filter type.

Electrostatic filters work by creating an electrostatic potential barrier that rejects charged particles with low momenta in direction of the potential barrier. This filter type is prone to changing transmission properties for particles at different incidence angles, as they have different momentum components in direction of the potential barrier. MAC-E filters use adiabatic collimation to drastically lower the angular spread of incoming electrons before applying the electrostatic filtering.

2.3.1 Transmission condition

The wording of *transmission condition* is used differently in two contexts: This section uses the theory published in [Kle+19]. In both the paper and this section, and generally as the name of an inequality, the wording corresponds to the inequality describing whether an electron is transmitted at an arbitrary point inside the fluxtube. The second context of *fulfillment of the transmission condition* is further elaborated in Section 2.3.3.

To construct this inequality, the electric potential barrier inside MAC-E filters can be described using conservation of the *sum of potential and kinetic energy*, as electrons are reflected on the potential barrier once their kinetic energy $E(z)$ reaches 0, with z being the electron position along the central axis of symmetry of the beamline. The axis of symmetry and the distance r to this axis are depicted in Fig. 2.5.

Using an initial kinetic energy E_S in a spatially varying electric potential U with the electric potential U_S at the electron source position, $E(z)$ becomes

$$E(z) = E_S + qU_S - qU(z)\,. \tag{2.1}$$

Energy and momentum can be split in components associated with movement orthogonal ($E_\perp$, $p_\perp$, *transversal*) and parallel ($E_\parallel$, $p_\parallel$, *longitudinal*) to magnetic field lines using the angle θ between direction of motion and magnetic field line:

$$p^2 = p_\perp^2 + p_\parallel^2$$

where

$$p_\perp = p\sin(\theta),\ p_\parallel = p\cos(\theta)$$

and

$$E = E_\perp + E_\parallel \tag{2.2}$$

where

$$E_\perp = E\sin^2(\theta),\ E_\| = E\cos^2(\theta)\,. \tag{2.3}$$

The condition for electrons to pass a given point is: $p_\| > 0$, and hence $E_\| > 0$. Using Eqs. (2.1) to (2.3), this yields:

$$0 < E_S + qU_S - qU(z) - E_\perp(z)\,. \tag{2.4}$$

With use of natural units and the relativistic energy-momentum relation with rest mass m,

$$p^2 + m^2 = (E+m)^2\,, \tag{2.5}$$

the relation

$$p_\perp^2 + p_\|^2 = (E_\perp + E_\|)(\gamma+1)m$$

directly follows, where the relativistic γ factor is $\gamma = \frac{E}{m} + 1$.

Identifying terms by their θ dependency gives

$$p_\perp^2 = E_\perp(\gamma+1)m \tag{2.6}$$

and

$$p_\|^2 = E_\|(\gamma+1)m\,.$$

For the adiabatic invariant, a variant of the so-called magnetic moment is invariant under adiabatic motion:

$$p_\perp^2/B = \text{const.}\ . \tag{2.7}$$

Adiabatic motion applies for particles experiencing only slowly varying fields [Jac99]. From comparison to calculations not assuming adiabatic motion, it has been found that motion of tritium decay electrons in the KATRIN experiment follows the adiabatic principle. Therefore, in the following adiabatic motion is assumed, following [Kle+19].

Combining Eqs. (2.3), (2.4), (2.6) and (2.7) gives:

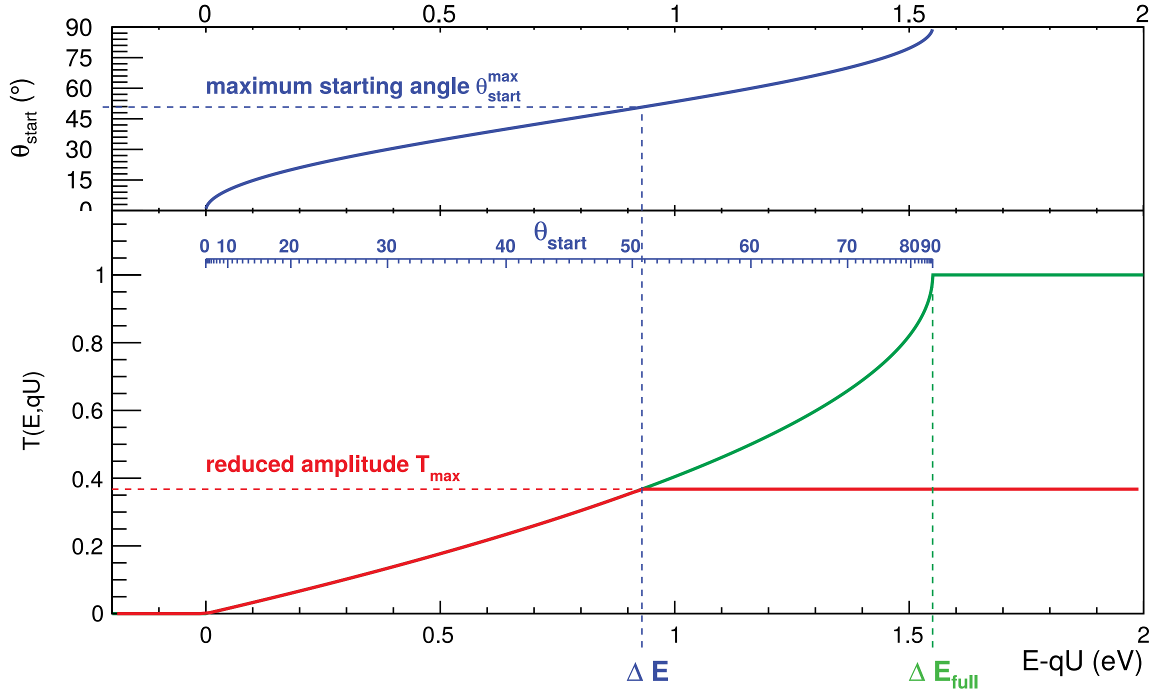

Figure 2.4: Exemplary MS transmission function for isotropically emitted electrons at $B_S = 3.6\,\mathrm{T}$ with (red) and without (green) angular filtering of PCH with $B_{\mathrm{PCH}} = 6\,\mathrm{T}$. Figure from [Zac15].

$$0 < E_S + qU_S - qU(z) - E_S \sin^2(\theta)\frac{B(z)}{B_S}\frac{\gamma_S + 1}{\gamma(z) + 1} \tag{2.8}$$

Whenever this inequality is not fulfilled along the path of an electron, this electron is reflected. Hence, this equation is called the *transmission condition.*

2.3.2 Transmission function

Inside a MAC-E filter, the magnetic field is kept small to minimize the $\sin^2(\theta)$ dependency of electron transmission, while an applied *retarding potential* defines the filter energy. With a known angular distribution of source electrons, the fraction of electrons transmitted through the detector can be calculated as a function of initial electron energies. This is called the *transmission function.*

A strong magnetic field after the MAC-E filter is used to reject high electron angles, reducing the width of the transmission function. In the KATRIN experiment, this is done by the pinch magnet at vanishing electric potential $U_{\mathrm{PCH}} = U_S = 0$. The transmission condition at this magnet is purely defined by the magnetic field at source and pinch magnet and the electron emission angle θ.

For an isotropic source of electrons starting with energy E, the transmission function is given by:

$$T(E,U) = \begin{cases} 0 & \mathcal{E} < 0 \\ 1 - \sqrt{1 - \frac{\mathcal{E}}{E}\frac{B_S}{B_A}\frac{2}{\gamma_S+1}} & 0 \leq \mathcal{E} \leq \Delta E \\ 1 - \sqrt{1 - \frac{B_S}{B_\mathrm{max}}} & \mathcal{E} > \Delta E \end{cases} ,$$

with the *surplus energy* $\mathcal{E} = E - qU_S$ and the *filter width/energy resolution* $\Delta E = \frac{B_A}{B_\mathrm{PCH}} E \frac{\gamma_S+1}{2}$ [Kle+19]. Indices $_S$ denote the source section, $_\mathrm{PCH}$ the pinch magnet and $_A$ the analyzing plane, further described in the next subsection.

Both the transmission function and the effect of the pinch magnet are shown in Fig. 2.4.

2.3.3 Analyzing plane

For electrons with high emission angles, the point of retardation is dependent on both the magnetic field and electric potential. Electrons that are not retarded until the first extremum of both, might be retarded until the second extremum. Therefore, the retardation properties of a MAC-E filter are defined by the magnetic field and electric potential between these extrema. If these extrema are at the same position or magnetic field and electric potential vary on a negligible level, the transmission properties of the MAC-E filter are purely defined by the magnetic field and electric potential at the common position of both extrema. Alternatively, this is also the case if the magnetic field is homogeneous in the range of the electric potential minimum so that the electric potential shape fully determines the longitudinal electron energy in that region. Both approaches allow to use a calibration of the MAC-E filter using monoenergetic electrons emitted with known angular distributions and energies from E-Gun, CKrS and gaseous $^{83\mathrm{m}}$Kr in the WGTS.

Since a precise calibration is crucial to reach low uncertainties on the transmission function, MAC-E filter field configurations with close field extrema and homogeneous magnetic fields at the position of electric potential extrema are used, where only a precise knowledge of fields at the electric potential extremum is needed to characterize the spectrometers' transmission properties. This requirement is called *fulfillment of the transmission condition*. The positions of these extrema span a surface inside the MAC-E filter, called the *analyzing plane* [Glü+13].

To reach high homogeneity on the analyzing plane magnetic fields and electric potentials, most MAC-E filter configuration use analyzing planes in the center of the filter with only slightly varying fields and potentials in the entire central region of the spectrometer.

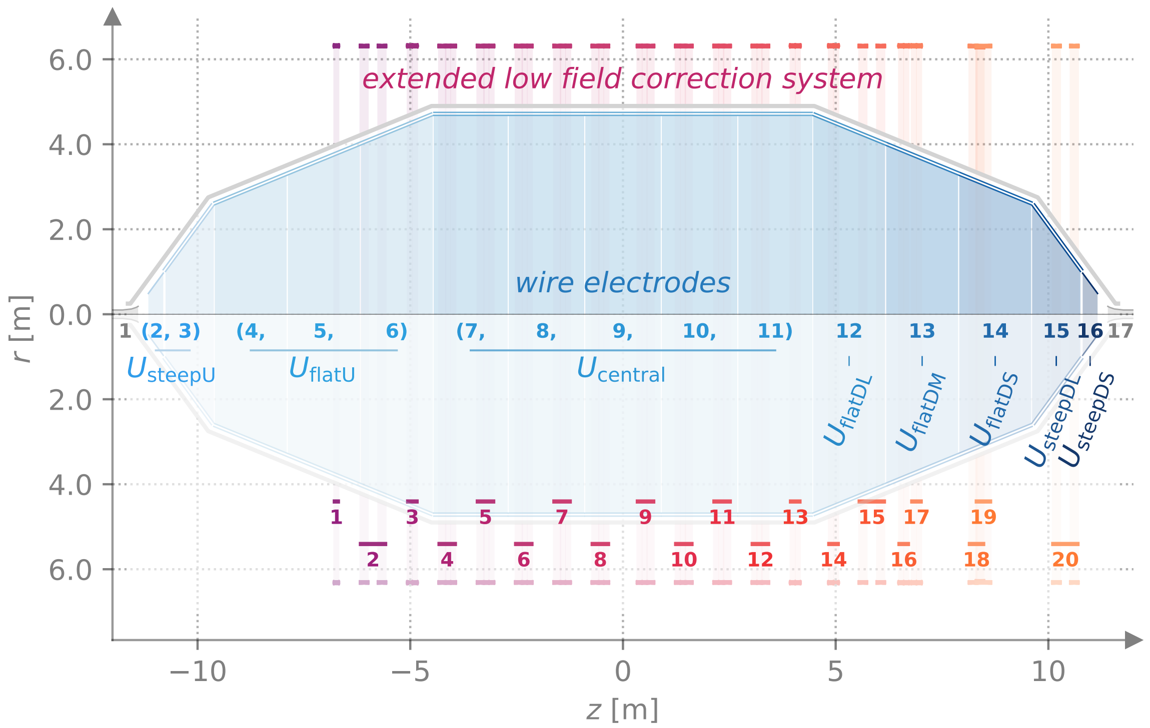

Figure 2.5: Main spectrometer including eLFCS air coils and electrodes. The groups of common variable potentials and their name are shown for electrodes 2 to 16. The potential names originate from the spectrometer side (**U**pstream, **D**ownstream), the cone type they are mounted in (steep, flat, central) and the size of the cone segment (**L**arge, **M**edium, **S**mall). Electrodes 1 and 17 are ground electrodes and therefore at a predefined potential. For the air coils, their eLFCS IDs are shown. Source of vessel geometry: [Hug08, fig. 3.2] Source of coil geometry: [Gil20]

2.3.4 KATRIN main spectrometer

The KATRIN main spectrometer is a MAC-E filter type spectrometer. Over its length of 23.3 m, an *extended low field correction system* (eLFCS) of 20 air coils allows for precise adjustment of the magnetic fields inside the spectrometer. Additional 16 horizontal and 10 vertical coils are part of the *earth magnetic field compensation system* (EMCS) [Glü+13]. To allow precisely adjustable electric potentials and for electrostatic shielding from the vessel walls, the entire inner surface is covered with roughly 650 m^2 of double-layered wire electrode modules constituting 15 isolated rings [Val10a; Hug08]. A high vacuum in the order of 10^{-11} mbar is ensured by three cascades of *turbo-molecular pumps* (TMPs) and two *non-evaporable getter* (NEG) pumps, connected to the spectrometer vessel through three pump ports of 1.7 m diameter [Are+16; Ake+19].

For each electromagnetic field setting for the KATRIN main spectrometer, the currents in all eLFCS coils can be addressed through individual supplies. For further flexibility of magnetic field configurations, the number of coils and the number of windings for specific eLFCS coils were increased during the course of this thesis, the amount of available coils and their winding counts changed over time. Short-circuits in the wire electrode system prevent using both wire electrode layers individually, and there exist also short-circuits between wire electrode modules. This leads to the freedom of setting the electric potential for all rings in form of 8 ring groups. Figure 2.5 gives an overview of components that provide parameters in electromagnetic settings and shows the used ring groups. Throughout this thesis, *MAC-E filter settings/spectrometer settings* are set values for wire electrode potentials and air coil currents.

3 KATRINs backgrounds

To reach the design sensitivity on an upper limit on the neutrino mass of 0.2 eV (90 % C.L.), the design goal for the rate of background in the KATRIN experiment was set to 10 mcps [KAT05]. In recent neutrino mass measurements, a total background in the order of 300 mcps was observed and an uncertainty on the retarding potential dependency of the background rate was introduced [Ake+19].

This raises the importance of both understanding and modeling, but also counteracting the main background sources in the KATRIN experiment. Therefore, Section 3.1 introduces known sources. The following sections discuss the most relevant background sources in further detail.

3.1 Overview

In tritium spectrum measurements, the main spectrometer filters electrons up to energies of around the tritium endpoint at 18.6 keV. With corresponding electric potentials applied to its vessel, signal electrons inside the main spectrometer have only low energies comparable to low-energetic background electrons whose energies are therefore indistinguishable from signal electrons.

Low-energetic electrons are not able to pass from outside into the fluxtube volume, as the magnetic field effectively shields the fluxtube. This was tested by measuring the correlation of background in the spectrometer to the cosmic muon flux and is called *magnetic shielding* [Alt+19]. Although the spectrometer is further operated at a pressure in the order of 10^{-11} mbar, the main spectrometer introduces background through multiple processes as depicted in Fig. 3.1.

High-energy electrons emitted inside the spectrometer mostly originate from the two radon isotopes ^{219}Rn and ^{220}Rn. These electrons are trapped, as their transversal momentum changes rapidly due to the changing magnetic field, while the kinetic energy gain inside the spectrometer due to electric potential differences is only in the order of approx. up to 200 eV, eventually causing their longitudinal momentum to reach 0. The detector can be

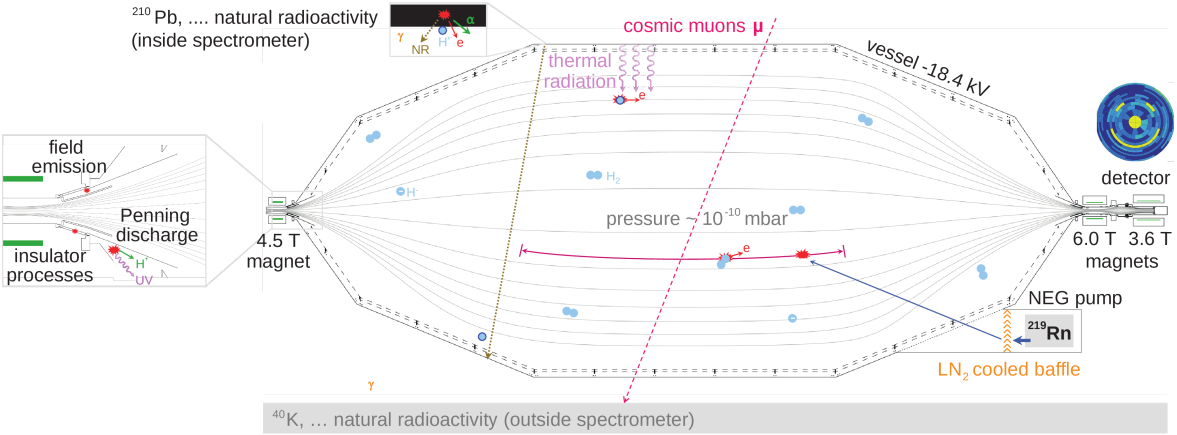

Figure 3.1: Background sources in the KATRIN main spectrometer. Magnetic field strengths and vacuum pressure changed since publication. Figure published under license [CC BY 3.0] in [KAT17, p. 2, fig. 1].

reached nevertheless by secondary electrons from ionization of residual gas molecules in the spectrometer vessel. Section 3.2 will elaborate on radon background.

Another background source are low-energy electrons emitted inside the spectrometer, arising mainly from ionization of highly excited Rydberg states. These electrons are mostly either rejected by the electrostatic barrier of the MAC-E filter if created before the analyzing plane or they pass towards the detector, also contributing to the overall background of the experiment. More on Rydberg background can be found in Section 3.3.

In the Mainz predecessor experiment, an additional background component, assumed to be Auger electrons, was of significant interest. As a similar but small background component is also observed in spectra of KATRIN background in Section 7.3, this electron source is introduced in Section 3.4.

Finally, the detector region contributes with a muon-induced background and intrinsic noise background. This background source is discussed in Section 3.5

3.2 Radon background

Radon background is mostly induced by two isotopes: First, ^{219}Rn is emitted from the two *non-evaporable getter* (NEG) pumps connected to two of the three pump ports of the main spectrometer [Frä+11]. Second, ^{220}Rn is prevalent on the inner main spectrometer surface [Mer+13]. From there, the electrically neutral radon emanates into the spectrometer volume and decays via α decay into ^{215}Po and ^{216}Po. These isotopes can now emit electrons via multiple processes, depicted in Fig. 3.2. These processes are also briefly introduced in the following. For a detailed discussion, the reader is referred to [Wan+13].

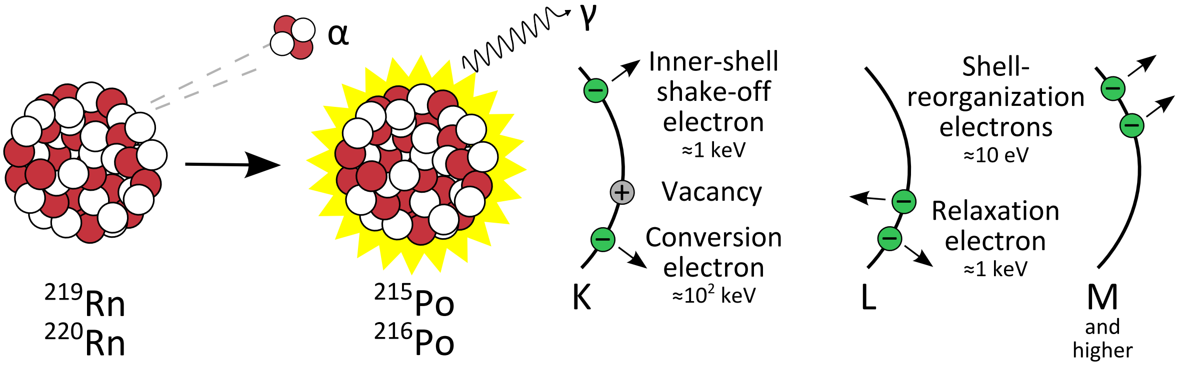

Figure 3.2: Secondary electron emission processes induced by radon α decay. Figure from [Har15, p. 84, fig. 4.1].

^{219}Rn decays to excited ^{215}Po* in 20.6 % of all α decays [Sin+13]. From there, the nucleus can perform two electromagnetic deexcitation processes: Either the energy is radiated as γ emission or, in approx. 3.3 % of ^{219}Rn α decays, this leads to *internal conversion* (IC), the emission of an inner-shell electron [Wan+13; Kra88]. While electrons can be emitted with discrete energies between nearly 40 keV to over 500 keV, the most prevalent IC process is a K-shell interaction with an energy of 178.13 keV occurring after 1.27 % of all ^{219}Rn α decays[Wan+13]. In this high energy range, electron paths inside the spectrometer can end in walls due to their cyclotron radius [Mer12, chap. 6.3.1]. The IC contribution from ^{220}Rn is negligible due to the low fraction of decays into excited ^{216}Po* of only 0.114 % [Wu07].

After α emission, the outgoing α particle can electromagnetically interact with shell electrons to either lift them into an outer shell (*shake-up*) or into continuum (*shake-off*, SO). Although shaking processes are more likely for outer shells, the SO electron energies for electrons from inner shells are significantly higher [Fre74]. Therefore, for the KATRIN experiment, only SO electrons from K, L and M shells are considered. For the comparable SO in ^{210}Po, shake-off probabilities range from $(1.65 \pm 0.16) \cdot 10^{-4}$ % [RAP75a] for SO of K-shell electrons to (1.84 ± 0.37) %[RAP75b] for M-shell electrons [Wan+13]. Energy of the SO electrons span a continuum up to “an endpoint at some tens of keV”[Har15, chap. 4.1.1].

Both IC and SO processes may leave a vacancy in inner electron shells. This vacancy can now be filled by an electron from a higher (sub-)shell. The released energy can now be emitted as an X-ray photon or transmitted into an outer *Auger electron* that might then be ejected into continuum. This relaxation process (RX) can not only occur for electrons filling the vacancy from an outer shell, but also in case of a *Coster-Kronig transition* from an outer subshell of the same shell [BA72]. Since in the process electron emission causes another vacancy that might be filled via another Auger transition, an *Auger explosion*, a cascade of non-radiative transitions, is possible to occur [Wan+13]. Auger electrons have “typical energies up to some tens of keV” [Har15, chap. 4.1.1].

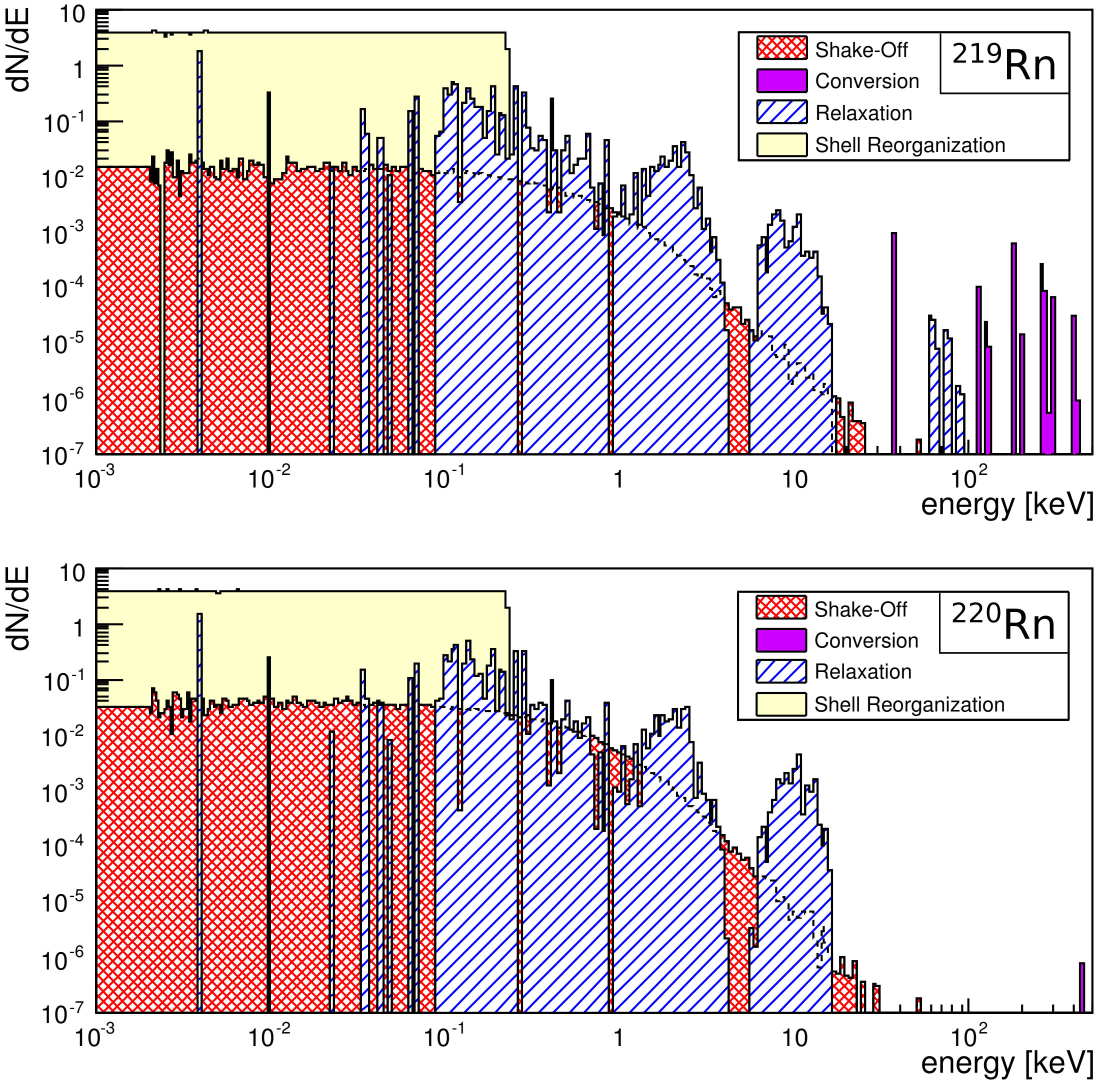

Figure 3.3: Simulated energy spectra for ^{219}Rn and ^{220}Rn. Figures published under license [CC BY 3.0] in [Wan+13, p. 12, fig. 4]

Finally, if none of the previous electron emission processes takes place, the atom is left as a higly unstable double charged negative ion, excited by the average, remaining rearrangement energy of approx. 250 eV [WKM06; Fre74]. For this model, this energy is assumed to fully be shared statistically by two outer-shell electrons. These are known to have ionization energies of 1 and 9 eV for the first and second ionization [Wan+13].

With the presented model, energy spectra were simulated for both ^{219}Rn and ^{220}Rn, as can be seen in Fig. 3.3. For background investigations at the KATRIN experiment, ^{219}Rn is of main interest with a significantly higher amount of IC electrons, a half-life of $t_{1/2} = 3.96\,\mathrm{s}$ and hence less efficient reduction through pumping, where ^{220}Rn has a significantly longer half-life time of $t_{1/2} = 55.6\,\mathrm{s}$ [Wan+13; Kir20].

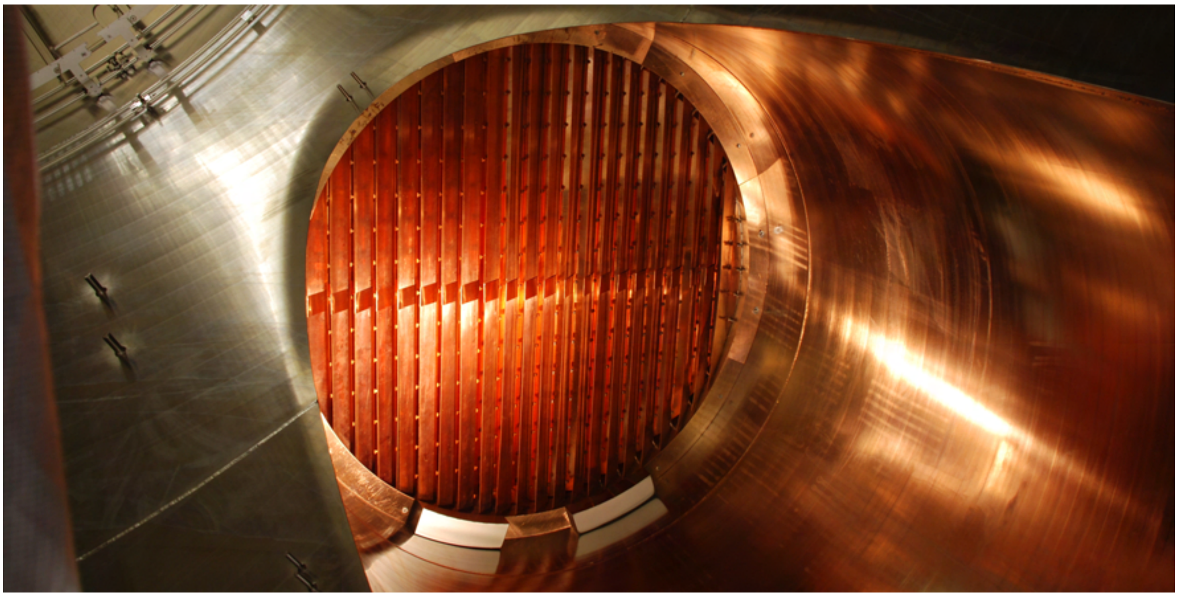

Figure 3.4: LN2 baffle in main spectrometer pump port III. Picture from [Gör14], taken by M. Zacher, 2012.

The absolute majority of primary radon background electrons from the described processes have a significant kinetic energy and are therefore magnetically trapped inside the spectrometer. Although they consequently do not contribute directly to the measured background, they can ionize residual gas molecules, leading to the emission of lower-energetic electrons that can reach the detector. Since a single trapped electron can generate multiple secondary electrons with this process, this background component brings time-correlated background events that, regarding short timescales, does not behave Poissonian.

Since the non-Poissonian behavior of this background component poses additional uncertainty on background rate measurements, a cryogenic *baffle* system was installed, reducing ^{219}Rn emanated from the NEG surfaces in the pump ports. It consists of liquid nitrogen cooled copper sheets that cover the pump ports inside the main spectrometer, as seen in Fig. 3.4. This system further acts as cryopump to enhance the general pumping efficiency of the pump ports [Gör14], and is enhanced through the recent addition of a further cooling stage.

Due to the magnetic shielding of electrons outside the fluxtube, the interaction of the emitted α particle with the walls is not a relevant source of background electrons. Another electron source would be ^{222}Rn, which is in its absolute majority pumped out of the spectrometer volume before it decays due to its relatively long half-life time [Mer+13].

It has to be noted that the presented model for electron emission after α decay assumes that the processes take place sequentially, while they can also coincide. Further, neglecting of shake-up processes and outer-shell shake-off further influence the simulated electron spectra.

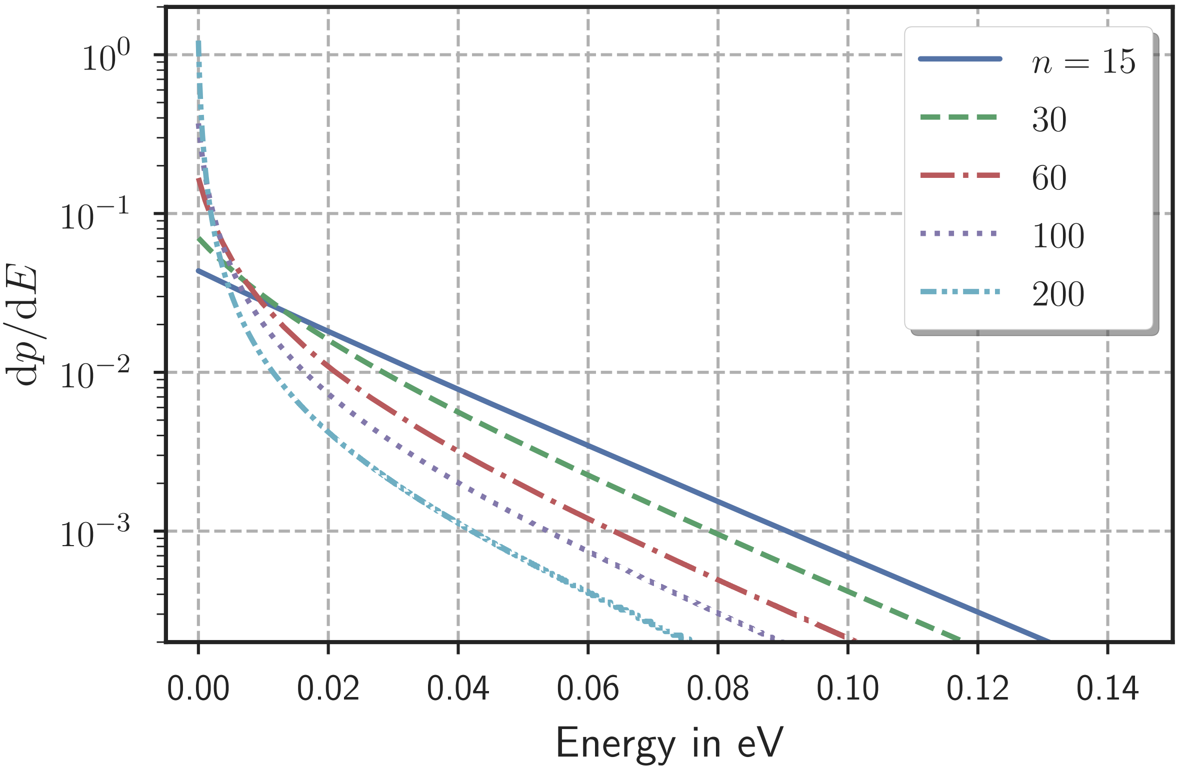

Figure 3.5: Simulated hydrogen Rydberg energy spectra for black-body radiation at 293 K and emission from different electron shells n assuming $l = 1$. Figure published under license [CC BY-SA 4.0] in [Tro19, p. 111, fig. 5.20].

3.3 Rydberg background

The Rydberg background model is an observation-driven extension of the KATRIN background model explaining low-energetic background electrons.

It is based on sputtering of ^{214}Pb alpha decay products. The resulting ^{210}Pb recoil nucleus successively performs sputtering of neutral atoms at the spectrometer vessel walls. Part of these atoms is left in a highly excited state, where black-body radiation from the vessel walls can excite electrons from these Rydberg states into vacuum. The electrons expected from this process have energies up to the order of tenths of eV [Tro19]. Exemplary simulated Rydberg energy spectra for hydrogen are shown in Fig. 3.5.

For the expected emission directions of the sputtered atoms, an angular distribution of sputtered atoms can be drawn from simulation, as shown in Fig. 3.6. While an isotropic emission would show a constant frequency in each $\Delta \cos(\alpha)$ bin, the angular distribution from simulation shows strongly forward-oriented emission.

For the reduction of this background, in between multiple measurement phases, the spectrometer section was baked at up to 350 °C with active NEG pumps [WOL09]. This also reduces the surface contamination of the baffle system described above.

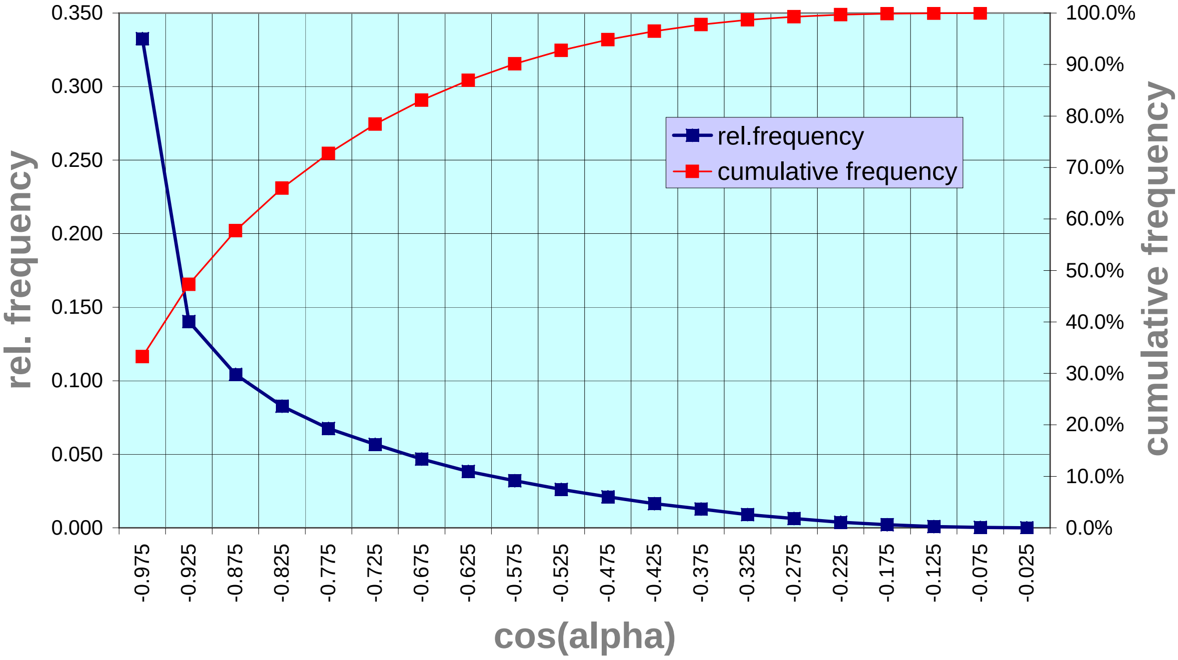

(a) Combined distribution for all particles involved in sputtering

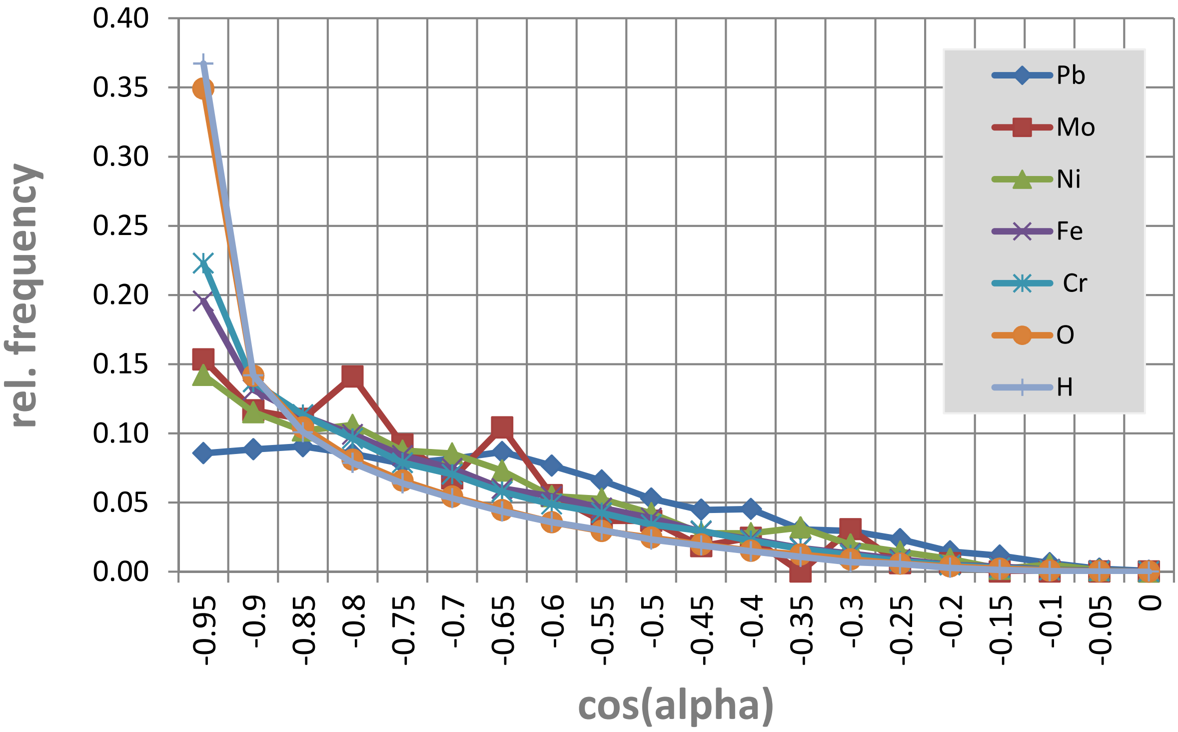

(b) Distributions by particle type

Figure 3.6: Angular distribution of sputtered particles. Figures and data kindly provided by Alexander Osipowicz, HS Fulda.

Because of the low electron energies originating from this background component, these electrons cannot non-adiabatically enter the fluxtube or overcome the analyzing plane and can therefore only be emitted in the so-called *downstream volume*, inside the fluxtube behind the analyzing plane.

3.4 Auger electron background

For the Mainz spectrometer, an additional background source was found to produce a second background peak approx. 4 to 7 keV above the main signal/background peak [Bar97], visible in background event spectra in Fig. 3.7. These were assumed to be Auger electrons originating from the electrode surfaces. In the Mainz analysis, it was noted that a similar picture would emerge for tritium contamination of the electrode surfaces.

This background source is not yet part of the KATRIN background theory. A similar background component will be further discussed in Section 7.3, where it is observed to yield a small contribution to the spectrum of background in the KATRIN experiment.

3.5 Detector background and effects

The FPD contributes with an intrinsic background shown in Fig. 3.8. It originates from multiple sources[Ams+15]:

Environmental radiation is mainly introduced by glass feedthrough insulators containing beta-decaying ^{40}K. As for all components in the KATRIN beamline, this background component is kept as low as possible by the choice of materials with low contribution to environmental radiation, and an additional copper shielding for glass feedtrough insulators was introduced.

Cosmic rays can partly be registered by the FPD. The FPD is enclosed by scintillator panels of a *muon veto system.* A coincidence trigger on scintillator events can be used to tag likely muon events with a high efficiency, assumed in simulations to be approx. 90 %.

Electronic noise introduces a background with high rates at energies $\lesssim$ 10 keV. Background in these energy ranges is not relevant, as the PAE accelerates electrons to energies above 10 keV, and therefore these events can be rejected. Since a distinct feature of this background type is its temperature dependency, it is reduced by a cooling system.

Since signal events do not occur simultaneously at multiple pixels, an additional *multi-pixel cut* rejects events that coincide over multiple FPD pixels.

Both muon veto and multi-pixel cuts are used with a coincidence window of 1.5 μs.

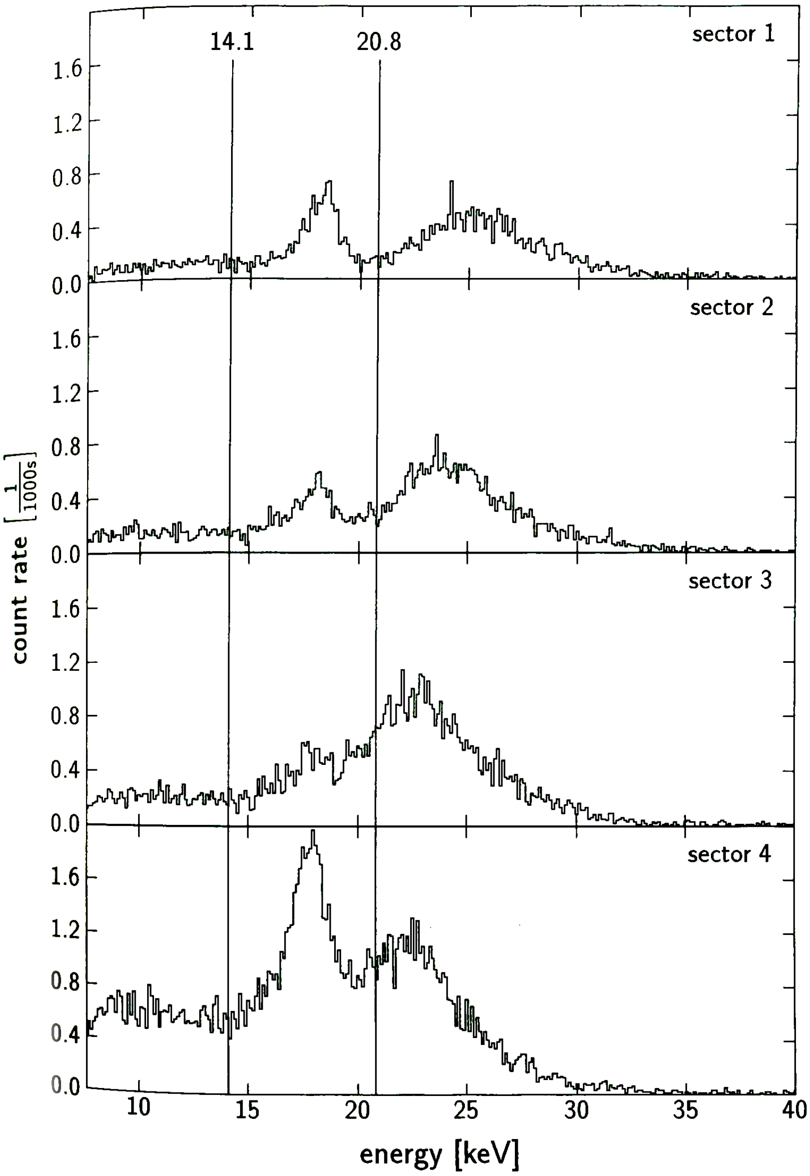

Figure 3.7: Mainz spectrometer background spectra of four inner detector segments. The volumetric background peak can be seen at signal peak position inside the marked region from 14.1 to 20.8 keV. The second peak at higher energies presumably originates from Auger electrons. Figure from [Bar97, p. 34, fig. 3.9].

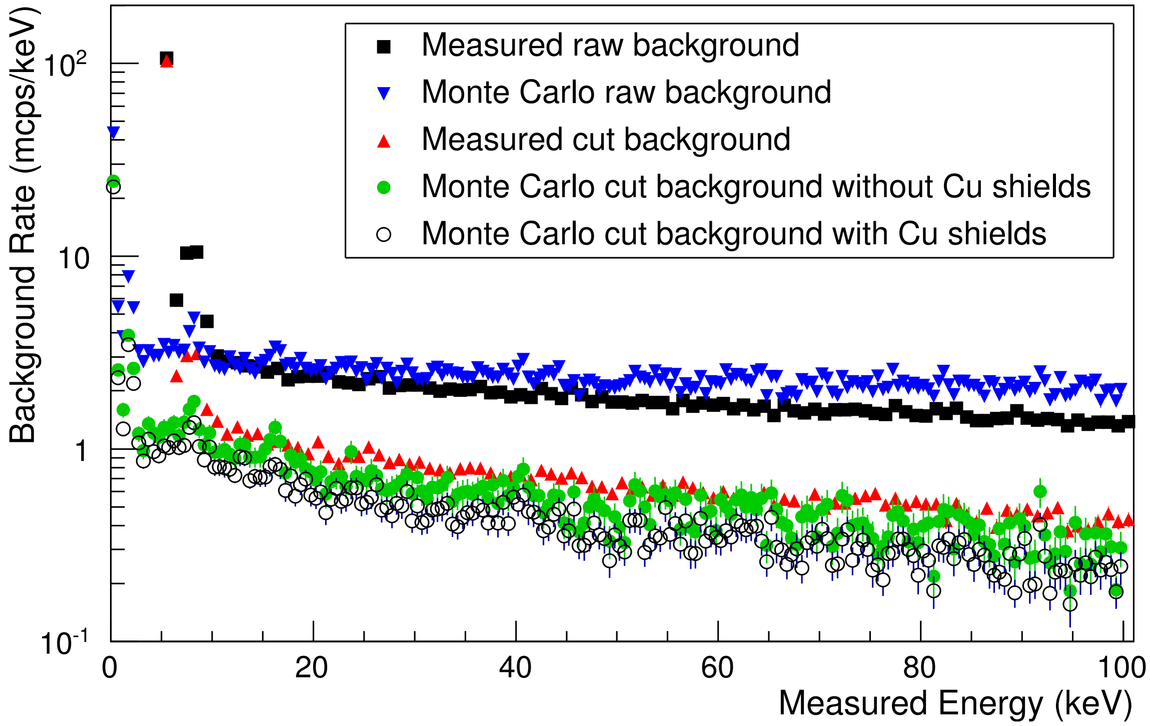

Figure 3.8: Detector background energy spectra from simulation and measurement at KIT. Channel-wise detector noise thresholds lead to deviations in measured data below 8 keV. Figure from [Ams+15, p. 57, fig. 32]

Pile-up peaks are finally not strictly a background source. Energies of multiple signals occurring simultaneously on a single pixel can wrongly be measured as a single event with a combined energy. This pile-up leads to additional peaks in the energy spectrum above the main peak.

4 Background reduction methods

In Section 3.1, two main background sources were identified: Background from secondary electrons generated by high-energetic electrons emitted and trapped inside the main spectrometer, so-called “Radon background”, and low-energetic electrons that are emitted in the main spectrometer volume and directly pass onto the detector, mainly “Rydberg background”. Since a low background rate is crucial for the design sensitivity of the KATRIN experiment, this chapter covers multiple concepts to reduce both background sources: As primary focus of this thesis, the use of *Shifted Analyzing Plane* (SAP) MAC-E filter settings is presented in Section 4.1. Three further methods for both background reduction and sensitivity optimization are discussed in Section 4.2, one using microchannel plate-based angular filtering and two methods coincidentally relying on electron *Time-of-Flight* (TOF). Due to the large amount of ideas discussed in this context, this chapter does not seek to give a complete list of possible background reduction methods.

4.1 Shifted Analyzing Plane

As main motivation for this thesis, the SAP MAC-E filter settings aim for background reduction using the already very flexible main spectrometer hardware at the KATRIN experiment. It is especially interesting since it does not require major hardware changes and is therefore easily implemented in the KATRIN setup.

The general concept of SAP is the use of new MAC-E filter settings with the analyzing plane shifted towards the detector, visualized in Fig. 4.1.

Its working principle is two-fold: For the low-energetic Rydberg background, the electric potential barrier at the analyzing plane acts as an unbreachable filter. Since low-energetic electrons also experience magnetic shielding, they can only reach the detector if emitted inside the fluxtube downstream the electric potential barrier. This volume is called *downstream volume* V_{ds}. By shifting the potential barrier as far downstream as possible, this volume is reduced and therefore also the Rydberg background is reduced.

For the high-energetic Radon electrons that cause the emission of secondary background electrons, these are stored adiabatically within the main spectrometer. Numerical studies

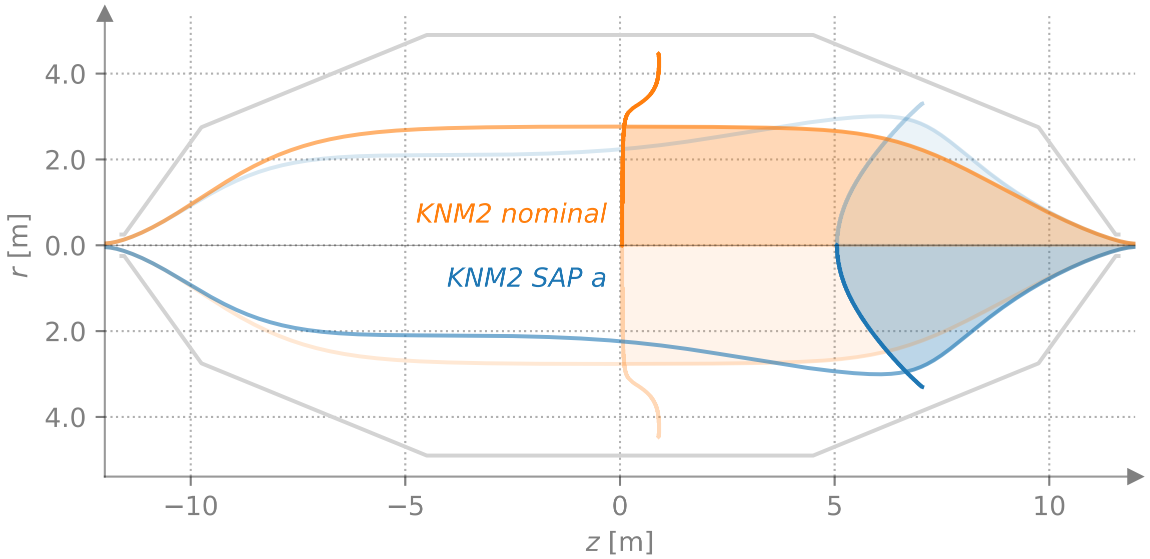

Figure 4.1: Visualization of settings “KNM2 nominal” and “KNM2 SAP a” from simulation. Field lines reaching the outer rim of the outer detector are shown as lines throughout the entire spectrometer vessel. Minimal electric potentials along magnetic field lines are indicated by additional vertical lines. The downstream volume enclosed by both surfaces is highlighted. Field simulations are performed using axisymmetric approximations assuming aligned components and further discussed in the next chapter.

for similar magnetic mirror trapping experiments[KT73] found that nonadiabatic effects can occur when shortening the distance L between the points of reflection, which causes nonadiabatic losses of stored electrons. These can be pictured as drift of the stored electrons towards outer field lines in areas of highly inhomogeneous magnetic fields. In the reduction of V_{ds}, the magnetic field along the z axis becomes rather inhomogeneous, as the fast changes in the magnetic field by the pinch magnet have to be compensated at the position of the analyzing plane by the use of air coils.

A non-relativistic calculation demonstrates the order of this effect:

For a mirror ratio of the maximal magnetic field to the minimal magnetic field of 1.5 in the trapping mirror, numerical calculations[KT73] show nonadiabatic effects for values $\epsilon = r_g/L \leq 0.05$, where r_g is the cyclotron radius. For an electron with $E_\perp = 1\,\mathrm{keV}$ and therefore a speed of $v_\perp \approx 1.876 \cdot 10^7\,\mathrm{m/s}$ in a magnetic field of $6\,\mathrm{G}$, the gyroradius is $r_g = \frac{mv\perp}{|q|B} \approx 0.18\,\mathrm{m}$. Therefore, nonadiabatic effects occur in this case roughly for L lower than or equal $3.6\,\mathrm{m}$.

Recent studies with ^{219}Rn KASSIOPEIA simulations [Kir20] confirmed the efficiency of SAP for the reduction of radon background events and in measurements using SAP, a reduced fraction of non-Poissonian background was observed.

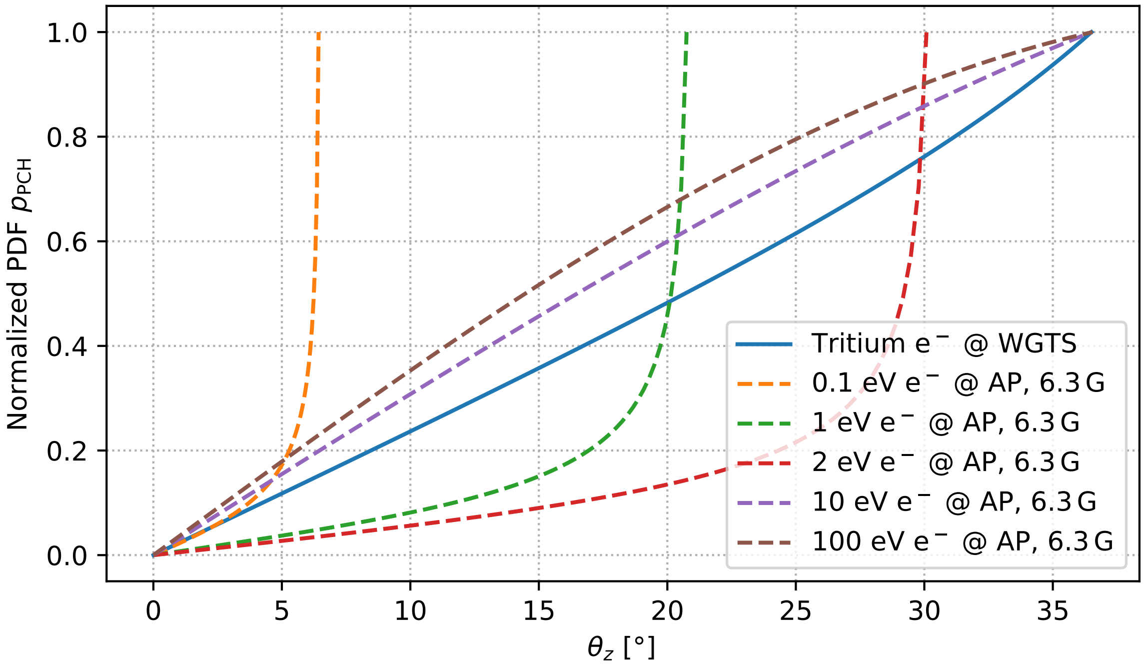

Figure 4.2: Normalized probability density function of different electron types reaching the detector at a specific angle θ_z. Tritium electrons are simulated with 18.6 keV starting energy, while background electrons at the analyzing plane (AP) start in an electric potential of -18.6 kV at a magnetic field strength of 6.3 G. No MAC-E filtering is considered. The calculations for this plot are further discussed in Appendix A.

All in all, reducing V_{ds} by shifting the analyzing plane therefore reduces both background sources, stored high-energetic radon electrons and low-energetic Rydberg background. This shift can be performed by adjusting currents of the MAC-E filter air coils and the potential offsets of the wire electrodes. Further details on the technical realization of the SAP can be found in Chapter 6.

4.2 Further methods

Many concepts on reduction of background and further improvement of $m^2_{\overline{\nu}_e}$ sensitivity were investigated in the recent past. Three especially interesting concepts are briefly introduced in the following.

Dual microchannel plate A new background reduction method based on *microchannel plates* (MCPs) is currently developed in Münster. The general concept arises from the angular distribution of signal and background electrons at the detector, shown in Fig. 4.2.

Initially, Hamish Robertson proposed the use of two shifted grids with holes that block the direct way of sight of field lines onto the detector. Therefore, only electrons with a large enough cyclotron radius would be able to pass through both grids.

The refined and currently tested approach uses two microchannel plates. The channels of the first plate are aligned with the magnetic field lines so that their walls are only hit by electrons with large enough cyclotron radius. On incident, the MCP will produce secondary electrons that are accelerated onto the second MCP, which acts as a photomultiplier-like second amplification stage before the detector.[1]

Time-focussing Time-of-Flight The *time-focussing Time-of-Flight* (tfTOF) method [Ful+] suggests the use of a third spectrometer with time-varying spectrometer vessel potentials, accelerating electrons with similar energies entering the spectrometer at different times so that they arrive simultaneously. Hence, by time window cuts, signal electrons of a specific energy range can be analyzed. Further, tfTOF allows to partly cut background electrons by arrival time.

This would, for the cost of installing a new spectrometer, promise a factor 2 improvement on the upper limit for $m^2_{\overline{\nu}_e}$.

Time-of-Flight using electron tagging If the flight duration of an electron passing the spectrometer is known, this further confines electron angle and energy. Using Time-of-Flight spectra in neutrino mass fits therefore introduces further information to improve the $m^2_{\overline{\nu}_e}$ sensitivity by over a factor of 5 assuming the designed background rate of 10 mcps [Ste+13].

A new method aims to implement this using for instance cryogenic current comparators to capture the entrance time of electrons into the spectrometer, allowing to “tag” individual electrons. This method would also allow to cut background electrons through coincidence measurements of electrons entering the spectrometer and hitting the detector. It would require current measurements in magnetic fields and vacuum to an unprecedented sensitivity and represents background reduction and sensitivity optimization methods that are currently in their early research stage.

---

[1] This approach will find further discussion in the theses of Kevin Gauda and Patrick Oelpmann.

5 Simulation methods

Since SAP configurations and background models are built using numerical electric and magnetic field calculations, quick, highly optimized calculations are key to both tasks. Calculations of magnetic field lines, magnetic fields and electric potentials are necessary for estimating various parameters such as the the analyzing plane position, downstream volume and the fields' variation over the AP.

In the following, the general abstractions from the full KATRIN beamline model performed to enable efficient simulations are covered in Section 5.1. The software stacks used for these simulations are presented in Section 5.2, covering both established software with its new optimizations and fast, newly written code. As powerful tool for rapid field calculations, zonal harmonic field expansion is explained in Section 5.3. A dedicated tool built for the spectrometer setting generation task is `gui_sap`, a graphical user interface wrapped around new and improved simulation code to allow MAC-E filter setting optimization in real time. Together with another new tool – a Python library allowing simple MAC-E filter simulations – it is presented in Section 5.4.

5.1 General assumptions

Very short simulation run times are a key feature of simulations performed for this thesis, as they enabled real-time optimization of MAC-E filter field settings and further interactive analyses. To achieve this high efficiency, multiple abstractions on the full KATRIN beamline model are performed. These are described in the following.

For all calculations in this thesis, adiabaticity is assumed. Therefore, for electron tracking, electrons are assumed to always cycle around a specific magnetic field line and Eq. (2.7) is assumed to be preserved. This is only the first order term of an asymptotic series that in total is an adiabatic invariant in electric and magnetic fields. The term varies with field inhomogeneities, an effect that occurs due to magnetron and cyclotron motion and that is more pronounced for higher energetic electrons in inhomogeneous fields [Pra+12; Nor63]. Estimated from the order of magnitude given in [Pra+12, chap. 8], this is assumed to be negligible for signal electrons in the MS analyzing plane region.

Further, for electron energy and momentum, the magnetic fields and electric potentials along this magnetic field line are used instead of the the potentials and fields at the actual positions along the electron cyclotron path around the field line. This assumes only slight variation of the fields that the electron experiences. This is true for small cyclotron radii as expected for KATRIN signal electrons. This makes it possible to abstain from calculation of cyclotron motion, which allows larger tracking step sizes and fields along a field line to be calculated once and then to be reused for different electron starting energies and angles.

For the earth magnetic field, the EMCS is assumed to fully compensate any non-axisymmetric components of the earth's magnetic field, and the remaining field in z direction is described as a constant offset of B_z of $-0.2\,\mathrm{G}$, which deviates from geophysical models by less than $1\,\%$ [Glü+13; Thé+15; Rei09].

Another approximation is the assumption of a fully axisymmetric setup. This assumes the full compensation of any non-axisymmetric components of the earth's magnetic field by the EMCS and axisymmetric alignment of all components.

Further, the calculation is performed for the case of vacuum. Since the KATRIN experiment is designed to use only a minimal amount of magnetizable components influencing the magnetic fields near the beamtube, this approximation is also valid [Rei13].

5.2 Simulation software

Speed and versatility were two main requirements for the used simulation methods, resulting in the improvement and partly rewriting of multiple simulation codes. In the following, an overview over the available field calculation codes and their advantages is given.

KASSIOPEIA The global simulation package `KASSIOPEIA` [Fur+17] is used for precise particle tracking and field simulation in KATRIN. This C++ package is designed to include any known relevant effect inside the KATRIN beamline, and is constantly compared against measurements and extended towards further detail. For `KASSIOPEIA`, the KATRIN geometry is implemented for multiple levels of abstraction, varying from full 3d models of the entire beamline to abstracted 2d axisymmetrical models. Although it was possible to accelerate the configuration file parsing by a factor of 2, loading an axisymmetric version of the MS and detector region still took approx. 25 seconds on the laptop used for simulation[1]. Although this is not significant for most use-cases with long simulation runtimes, faster loading times are necessary for real-time simulation. In the following, `KASSIOPEIA` will find it's application as reference in verification of significantly faster simulation methods.

---

[1] Associated Kasper Merge Request: !361

bfield_3d A relatively lightweight magnetic field and potential simulation application, `bfield_3d` [Fla01], allows the calculation of field lines in non-axisymmetric setups with circular coils using explicit elliptic integration. For near-axis fields and potentials, it uses a series expansion to optimize performance. Technically, this is a single-core C++ application, which benefited massively from enabling gcc compiler optimizations such as "-O3", "-fuse-linker-plugin" and "-flto" during the course of this thesis. A drastic speed improvement could also be made on the realization that `bfield_3d` simulates coils as bundles of individual windings: Coils still showed similar magnetic fields in the relevant area with significantly reduced winding counts but unchanged amount of ampere-turns. Using this knowledge especially for superconducting magnets, for which initially tens of thousands of coil windings were simulated, with a reduction to no more than 14 windings per coil, `bfield_3d` is now able to simulate magnetic fields inside the main spectrometer in the matter of a few seconds. This is a significant improvement over the previous runtime of simulations in the order of half an hour. With these optimizations on code and configuration files, `bfield_3d` provides a robust and quick method to calculate magnetic fields, field lines and potentials inside the entire main spectrometer.

adiabatic_transport For the task of calculating electric potentials as well as longitudinal and transversal energies along the field lines calculated by `bfield_3d`, the application `adiabatic_transport` is provided by Ferenc Glück[2], with adaptions by Christian Weinheimer. It features a C++-based electric potential calculation using zonal harmonic source coefficients pre-calculated from `KASSIOPEIA` simulations of a 3d main spectrometer model. The working principle of pre-calculated models using zonal harmonics will be discussed in Section 5.3. For this thesis, it was extended to calculate further information on the fly, such as information about the extremum position and value of the electric potential, the magnetic field at this potential and the total volume enclosed by the given fluxtube. Also, it now allows the calculation of any amount of steps for a single field line. Performance-wise, this technique is able to perform all relevant calculations in under a second, even for multiple field lines. Consequently, loading the zonal coefficient files took the longest in executing this application, which was solved by making this application a separate, continuously running process that only loads the source coefficients once.

magfield Since zonal harmonic field expansion proved to be highly efficient for frequent calculations with unchanged geometry, Ferenc Glück also provided C++ files for magnetic field calculation using the same methods. After wrapping it in an application with the generic

---

[2] IKP/KIT

name `magfield`[3], it allows the precalculation of expansion coefficients for a specified geometry and provides similar field information as `bfield_3d`. The use of this new application and the improved version of `adiabatic_transport` allows to calculate all relevant information on a given MAC-E filter setup in near real-time.

zonalfields2d Finally, `zonalfields2d`, a new electric and magnetic field calculation software, was also developed during the course of this thesis. It is based on the field calculation code by Ferenc Glück that can be found in `magfield` and `adiabatic_transport`, provides a common interface for calculation of electric potential and field as well as for magnetic field and magnetic vector potential, and allows magnetic field line tracking. This C++ library further features Python3 [VD09] bindings using NumPy arrays [VCV11] for high efficiency. Especially the Python bindings make this application a very simple and reliable solution for interactive analysis of MAC-E filter settings, and will consequently be used for most of the following calculations.

All of these codes were verified against at least `KASSIOPEIA` during the course of this thesis. Track calculations for a shifted analyzing plane setting were performed with a 3d `KASSIOPEIA` simulation starting tracking from the center of each detector pixel. Misalignment in the KATRIN geometry leads to differences in the tracked field lines for multiple pixel centers of the same detector ring, spanning a range of radii for field lines for each given detector ring. All magnetic field calculation codes were shown to lay within this range in the entire spectrometer section. The electric field calculation codes were compared with results from the axisymmetric `KASSIOPEIA` main spectrometer model, showing slight deviations in the order of 2 eV. This is expected, as the wire electrodes do not form a perfect Faraday cage, but allow slight penetration of the electric potential applied to the main spectrometers.

Multiple wrappers around each of these codes exist and due to the dynamic development presented here, everything except from `KASSIOPEIA` has been used for analysis at one point in the work on this thesis.

5.3 Zonal harmonic field expansion

The *zonal harmonic field expansion* (ZHFE) method for axisymmetric electric and magnetic field calculation is based on three steps: Every integration over the given geometry necessary to calculate electric and magnetic fields is moved to a precomputation step where all field information is stored in expansion coefficients. When the contribution of a geometric element

---

[3] `magfield` was already the name of a similar application by Ferenc Glück. The software discussed here is a new wrapper of his field calculation code.

to the total field is changed, e.g. because the current or potential applied to it is varied, the calculation of the resulting linear combination of precalculated fields from these elements becomes a linear combination of the expansion coefficients. Then the fields can be directly calculated from these combined coefficients.

In the following, these steps are presented further.

Step 1 (geometry precomputation) Fundamentally, ZHFE allows to describe arbitrary axisymmetric fields inside a given spherical boundary centered on the axis of symmetry by precomputable expansion coefficients that scale linearly with the field strengths they represent [Glü11a; Glü11b].

This is possible since for fields in vacuum, two uniqueness theorems hold as presented in the context of electric fields in [Gri12, chap. 3.1]. They can be stated as that for stationary electric and magnetic fields in vacuum, a Neumann boundary condition of known scalar potential for a potential on a boundary surface fully describes the field inside the enclosing volume, as long as this volume does not contain divergence and curl. Using axial symmetry, for ZHFE this can be used for two-dimensional fields in the (z, r) plane, representing the fields inside circular areas centered on the axis of symmetry z by their scalar potentials on these circles. The expansion used for ZHFE now uses Legendre polynomials to expand $V(u = \cos(\theta))$ along the angle θ referring to points on this circle. The centers are so-called *source points*, the size of these spheres is called *convergence radius* and the coefficients gained from the expansion are named *source coefficients*. The maximal possible convergence radius is limited by the geometry that is closest to the individual source point.

To keep full freedom in applying intensities to individual geometric elements, the source coefficients are calculated for each element separately, applying e.g. a unit voltage or current individually to only this element.

Step 2 (element fields combination) Maxwell's equations describe a theory where the electric and magnetic fields scale linearly with charge distribution and current density. Therefore, it is possible to describe a static electric or magnetic field by the linear combination of fields previously generated for each geometric element separately. By use of the linearity of the source coefficients with respect to the fields they represent, it is possible to abstract from a superposition of fields to a superposition of the source coefficients for these fields at a given source point. This calculation can be performed in bulk for all available source points once the intensity of each element's contribution to the total field is known.

Step 3 (calculation of field properties) Now, the combined source coefficients can be used to calculate various field properties such as the electric potential, magnetic scalar or vector potential, electric or magnetic field vectors.

5.3.1 Optimized field line tracking

Field line tracking is usually performed by an iterative method based on spacial discretization, commonly the Euler method. The precision of these methods changes with the chosen discretization step size, requiring small step sizes even if the field line is only important in a few points in space. In the following, a correction algorithm is presented that can be used to refine the fluxtube radius r_i at a given step i with position z_i. The correction algorithm itself is initially written by Ferenc Glück to find a field line from ZHFE at arbitrary z positions, and was adopted for field line tracking for this thesis.

Fundamentally, the magnetic flux $\Phi_{B,i}$ enclosed by the circle ∂S_i defined by $(r = r_i) \wedge (z = z_i)$ is required for all i to be constant[4]. This makes it possible to correct errors from an iterative method by optimizing r_i to minimize the discrepancy between the magnetic flux enclosed at step i versus step 0.

Technically, this is based on Stokes' theorem, which allows the magnetic flux to be calculated as

$$\Phi_B = \iint\limits_S \mathbf{B} \cdot d\mathbf{S} = \oint\limits_{\partial S} \mathbf{A} \cdot d\boldsymbol{\ell} \,.$$

To calculate $\Phi_{B,i}$, ∂S can be identified as the circle ∂S_i. For axially symmetric fields, non-axial components of $\mathbf{A}$ cancel in this integration, leaving

$$\Phi_{B,i} = 2\pi r_i A_z \,.$$

Now the accuracy of r_i can be measured by the value of $f(r_i) = |\Phi_{B,0} - \Phi_{B,i}(r_i)|$, which ideally would be 0. This function can now be optimized with the parameter r_i using the Newton method. Here, B_z can be used as rough approximation for $\frac{dA_z}{dr}$.

5.4 Visualization and tooling

A key component for Shifted Analyzing Plane setting generation was agility in simulation and tooling, as both new MAC-E filter settings with specific requirements were needed frequently

---

[4] as in “the amount of field lines enclosed by a fluxtube is constant”

and various possible parameters for MAC-E filter background were to be explored. From this need, a variety of small analysis codes and wrapper scripts was written for this thesis. Three new projects are especially notable:

gui_sap Due to the various optimizations in simulation codes presented in Section 5.2, a GUI tool allowing live MAC-E filter setting exploration and optimization, `gui_sap`, was created and constantly expanded. While initially wrapping `bfield_3d` for magnetic field calculation, it currently uses the ZHFE applications `adiabatic_transport` and `magfield` for field calculation and the calculation of some setting quality measures. After loading or entering a geometry description for the magnetic coil setup, all ZHFE magnetic source coefficients are calculated. The user can interactively enter or update a MAC-E filter setup, for which `gui_sap` provides and updates eight plots with information for a user-defined set of initial fluxtube radii and user-defined incidence angles and 25 parameters are additionally presented in a text-based view, six of which provide information for a second user-defined incidence angle. It has a custom-built scripting interace to allow for quick analysis of multiple settings in a common tool. The user interface for an exemplary plot is shown in Fig. 5.1. Technology-wise, `gui_sap` is based on the Python3 scripting language [VD09], PyQt5 [PyQ20] for the GUI and PyQtGraph [Cam20] as a fast plotting library.

gui_sap_presets Initially built to complement `gui_sap`, `gui_sap_presets` provides a small set of coil geometries, main spectrometer settings and a number of `gui_sap` scripts. For this thesis, it is now used as a common source for the state of relevant geometry and settings of the KATRIN experiment during relevant measurements.

zf2d4katrin While more complex analysis moved to `zonalfields2d`, the new Python3 library `zf2d4katrin` provides an interface to use geometry files from `gui_sap_presets`, using the Python3 bindings of `zonalfields2d`. Further, it contains scripts using this interface to provide new functions with mostly pre-set but highly customizable parameters that are able to calculate the minimum of the electric potential and absolute magnetic field along field lines and the volume enclosed by the fluxtube downstream the analyzing plane. With this, it is now possible to quickly create a new analysis based on MAC-E filter simulations without any boilerplate code or need for intermediate files.

As these codes were developed during the course of this thesis, various combinations of the above codes were used for various tasks.

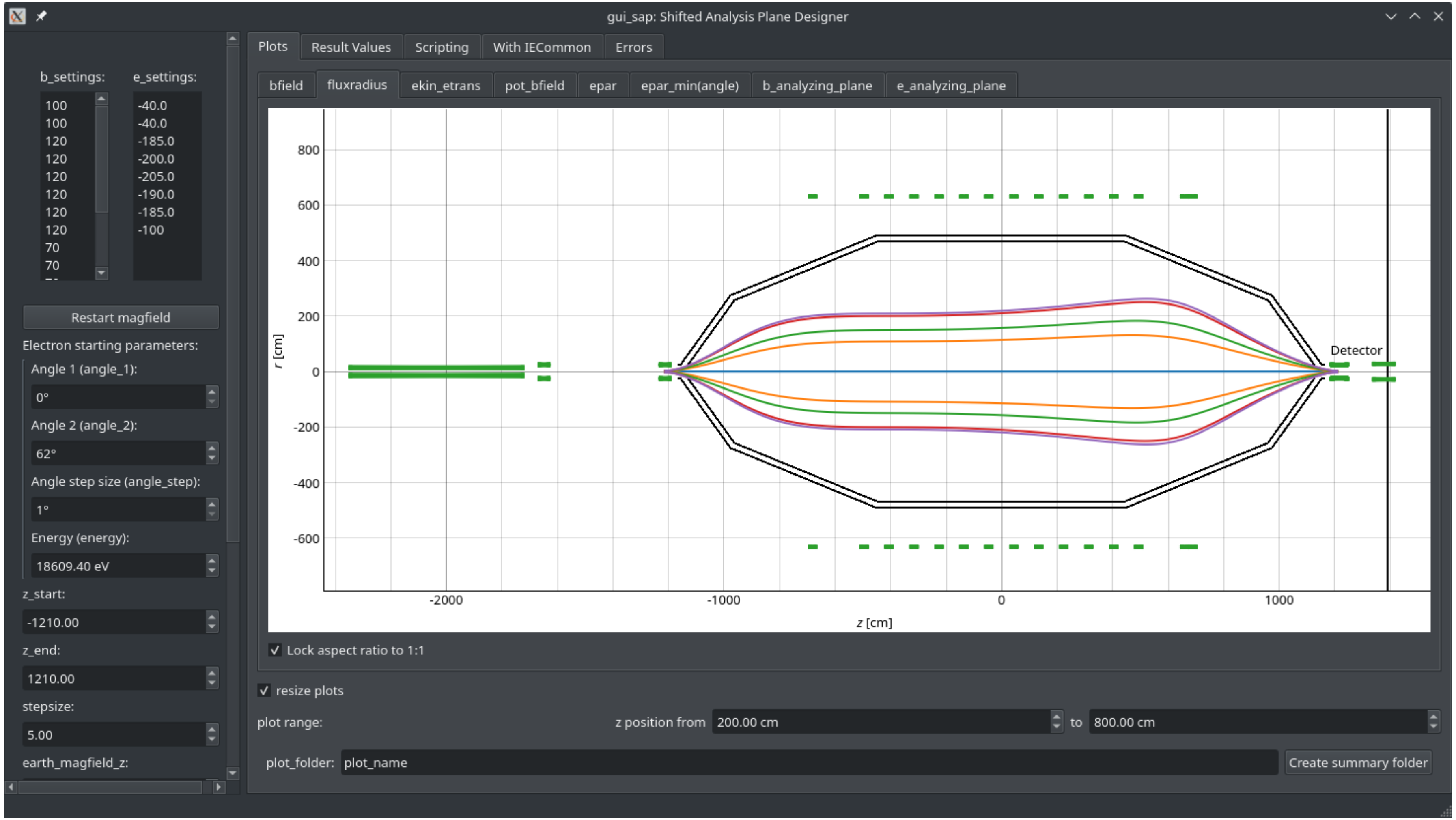

b_settings:
100
100
120
120
120
120
120
120
70
70

e_settings:
-40.0
-40.0
-185.0
-200.0
-205.0
-190.0
-185.0
-100

Electron starting parameters:
Angle 1 (angle_1): 0°
Angle 2 (angle_2): 62°
Angle step size (angle_step): 1°
Energy (energy): 18609.40 eV
z_start: -1210.00
z_end: 1210.00
stepsize: 5.00
earth_magfield_z:

☑ Lock aspect ratio to 1:1
☑ resize plots
plot range: z position from 200.00 cm to 800.00 cm
plot_folder: plot_name

Figure 5.1: Screenshot of `gui_sap` with sub-tab 'fluxradius' in 'Plots' selected directly after startup. On the left sidebar, the MAC-E filter setting and general simulation properties can be configured with live feedback in plots or numerical results shown on the right. There, also a scripting environment with customizable output, a convenience calculation from entered electrode settings to settings including the common offset voltage *IE common* and the error log can be found.

6 MAC-E filter settings

Both the SAP method and further main spectrometer background investigations require the design of advanced electromagnetic field settings for the KATRIN main spectrometer. This chapter presents the quality measures of MAC-E filter settings in Section 6.1 before guiding through the process of SAP setting design in Section 6.2 and listing two further properties of MAC-E filter settings that can be used for setting creation in Section 6.3. Section 6.4 then gives an overview on resulting SAP settings used in measurement campaigns.

6.1 Quality measures

(S)AP settings require precise optimization on multiple properties that will be introduced in the following.

SAP specifics The magnetic field and electric potential extrema of SAP settings are shifted towards the pinch magnet. This reduces the size of the downstream volume V_{ds} to reduce Rydberg background and allows for a rather longitudinally inhomogeneous magnetic field upstream the analyzing plane for Radon background reduction. Therefore, the main optimization parameters here are the z position of the analyzing plane and the resulting size of V_{ds}.

Transmission condition fulfillment As discussed in Section 2.3.3, to enable measurements of transmission properties, analyzing plane settings for tritium measurements have to be optimized for independence of electron angles on analyzing plane position and shape. For central analyzing plane settings, this can be done by maximizing the longitudinal homogeneity of the magnetic field around the electric potential minima [Glü+13]. SAP settings feature a longitudinally inhomogeneous magnetic field. Hence, the extremum positions of electric potentials and magnetic fields along given magnetic field lines are optimized to be spatially close to each other, resulting in a common (analyzing) plane of field extrema. This requires electric and magnetic fields to be optimized simultaneously for SAP settings.

Early retardation Electrons with kinetic energies close to the spectrometer potential are filtered around the position of the analyzing plane. It is possible that high-angle electrons already experience filtering further upstream in the spectrometer. This happens because in regions of higher magnetic fields, where the longitudinal energies of electrons is reduced, already a lower electric potential barrier is enough to reject high-angle electrons. The result is a modified the transmission function of the spectrometer, overlaid with an additional transmission curve for high-angle electrons and therefore a step in the transmission function. Early retardation can be avoided by asserting that electrons of all incidence angles have the minimum in longitudinal energy at the position of the analyzing plane [Val10b].

Radial inhomogeneity Radial variations in the analyzing plane fields have to be compensated in later analysis. As a given ring on the detector ideally maps onto an axisymmetrical ring on the analyzing plane, a too high variation in the transmission function along one such ring over the analyzing plane smears the transmission function, effectively reducing the energy resolution of the spectrometer. Very importantly, measurements of the analyzing plane fields are also more accurate for higher radial homogeneity, since uncertainties on positions of electron beams for field measurements are less significant.

Non-adiabaticity For very low fields, electrons are no longer guided adiabatically, making a determination of the spectrometer transmission function arbitrarily difficult. It is possible to simulate non-adiabatic effects with KASSIOPEIA to verify that the assumption of adiabaticity is fulfilled for a given setting.

Walls/Magnetic guidance Fluxtube collisions with the walls should be avoided. Otherwise, they will absorb the signal electrons and emit background electrons [Glü+13]. For SAP settings, where the analyzing plane with the smallest magnetic field is very close to the exit of the main spectrometer, the fluxtube radius is limited by the cone shape of the downstream part of the spectrometer vessel. This puts another lower bound to the magnetic field strength that turned out to be more relevant than the non-adiabaticity bound.

6.2 SAP setting design

To fulfill the requirements presented in Section 6.1, the following procedure evolved with the use of `gui_sap`:

First, a view on the fluxtube shape (as plot of $r(z)$ for a few starting radii) can be used to optimize the air coil settings. Here, the full freedom of all air coils is available. Also plotting the magnetic field strengths allows to check for unwanted second minima and the radial field inhomogeneity at the minimum position of the absolute magnetic field along the given fieldlines. After this optimization, plots of the longitudinal energy of electrons slightly above the filter energy can be used to optimize the electric potential settings. Electrons follow the field lines shown in the fluxtube plot with minimal and maximal incidence angle. To avoid potential traps and early retardation, the longitudinal energies of these electrons is optimized to only have a single minimum and the minima for both simulated starting angles are optimized to be as spatially close together as possible. For this task, also a plot showing the electric potential along the analyzing plane can be used to reduce radial inhomogeneities. Using `gui_sap`, it is also possible to view the position of the extrema of magnetic field strength and electric potential along z for multiple field lines numerically, to further align both. Once this task is finished for the electric field, it becomes an iterative process, in which it is repeated for air coil and wire electrode settings, until an optimal setting is reached by measures of the previous section.

6.3 Further properties

Apart from the quality measures discussed in Section 6.1, further properties of a MAC-E filter setting can be calculated. These are presented in the following.

Transmission function For known angular distributions of the electron source and in the case of a fulfilled transmission condition, the transmission function $T(E, qU)$ can be calculated. In all cases, the minimum of electric potential and magnetic field can be plotted as function of the e.g. the electron emission angle, giving similar information on possible early retardation effects.

Voltage dependent background slope The pinch magnet can also reject background electrons depending on their initial energy and angle. This process depends on the kinetic electron energy and for background electrons generated inside the MAC-E filter this energy is dependent on the filter potential voltage and the starting magnetic moment. Therefore, the background is overall voltage dependent, but this dependency varies for different starting energies. This effect is further explored in Section 8.2.

6.4 Settings for the KATRIN experiment

For the KATRIN experiment, various MAC-E filter settings for testing of the SAP method were developed as part of this thesis or using the tools and presets created for this thesis. Their design goals for different measurement campaigns are presented in their measurement context.

During satellite measurements to the first two *KATRIN neutrino mass* (KNM) campaigns *KNM1* and *KNM2* in 2019, SAP research and development was performed under the name *KNM1/2 SAP*. Settings are named starting with the measurement name, where the symmetric settings used for tritium spectrum scans during KNM1 and KNM2 are called *KNM1/2 nominal*. Rates measured during SAP measurements and KNM1 and KNM2 tritium scans are visualized in Fig. 6.1.

KNM1 SAP took place from 13th to 17th May 2019. For this campaign, the setting creation aimed at the test and demonstration of the expected background reduction efficiency using the SAP method and investigation on possible improvements by reduction of the field strength of superconducting magnets by a factor of 2, using 35 % magnetic field strength instead of the usual 70 %. The goal of this field strength reduction is to enlarge the influence of air coil currents on the fluxtube shape. When all magnetic field strengths are reduced by the same factor, the magnetic fluxtubes only change slightly because of the unchanged earth magnetic field, which can be corrected for. Consequently, air coils that previously ran at their maximal currents are then only used to half of their maximal currents, introducing a further range for fluxtube shape optimization.

In this measurement campaign, the small amount of previous experience on SAP measurements at the KATRIN experiment and the need to directly generate new settings after gaining more knowledge on the behavior of the superconducting magnet field strengths were two defining challenges. Both required on site implementation of further settings to directly test new assumptions on the behavior of background electrons inside the main spectrometer. Because of the unexpectedly high background of SAP settings at 35 % field strength, it was decided to switch back to a compromise field strength of 60 % superconducting magnet field strength in the spectrometer and detector section, while the entire source and transport section and magnet PS1 were driven to 70 %. Later in these measurement campaign, all superconducting magnets were set back to a field strength of 70 %. Altogether, 18 different settings were tested, of which 4 were designed in advance. 4 settings were also tested in short tritium beta scans to verify the calculated transmission functions.

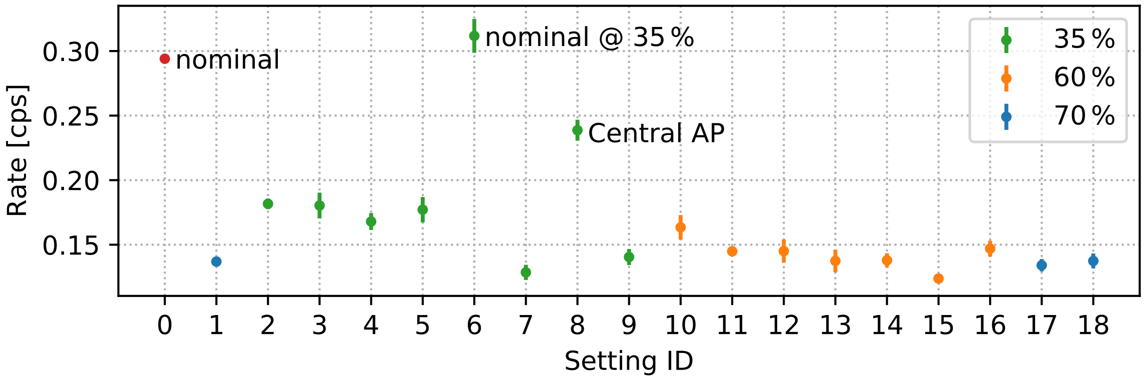

(a) KNM1 SAP measurements and KNM1 tritium scan background rate with nominal setting. Color indicates superconducting magnetic field strength, where 70 % superconducting field strength is used in neutrino mass measurements.

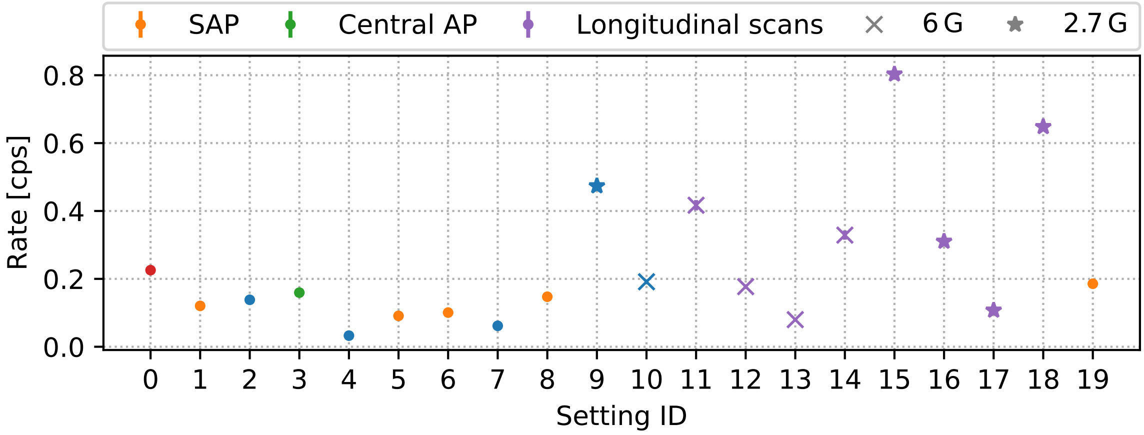

(b) KNM2 SAP measurements and KNM2 tritium scan background rate with nominal setting. Color indicates setting type. Marker type highlights measurements with air coil settings KNM2 2.7 G and KNM2 6 G.

Figure 6.1: Rates of MAC-E filter settings measured during KNM1 SAP and KNM2 SAP measurement campaigns.

This measurement phase allowed to demonstrate a background reduction of more than a factor of 2 using SAP settings in comparison to the "KNM1 nominal" setting. Further, a *Central AP* setting could be tested, which features an analyzing plane at the known central position with steeper upstream and downstream fluxtube shapes for background reduction.

KNM2 SAP took place from 11th to 15th September 2019 with one day of CKrS measurements for electric potential and magnetic field mapping of the analyzing plane of one SAP setting. With the knowledge from KNM1 SAP, this campaign aimed at both providing an SAP setting for future tritium campaigns and performing further measurements covering particular parts of the now known parameter space. For the SAP settings, two main settings were introduced, namely setting "KNM2 SAP a" and "KNM2 SAP f". While the first setting is optimized for especial homogeneity in electric potential and absolute magnetic field strength over the analyzing plane with a downstream volume of approx. $65\,\mathrm{m}^3$, the second setting reduces the downstream volume further to approx. $51\,^3$ on the cost of field homogeneity.[1]

The electric potential and magnetic field inhomogeneities of both SAP settings are shown in Fig. 6.2. Setting "KNM2 SAP a" features an expected absolute magnetic field inhomogeneity over the analyzing plane of approx. 0.22 mT with an electric potential spread of approx. 3.8 V over the analyzing plane. For setting "KNM2 SAP f", similar axisymmetric simulation assuming perfect alignment of the beamtube components leads to inhomogeneities of approx. 0.40 mT and 6.0 V.

As further reference, the electric potentials and magnetic fields along field lines inside the detector covering fluxtube can be found exemplarily for setting "KNM2 SAP a" in Fig. 6.3.

Additionally, for the KNM2 SAP measurement campaign, a new Central AP setting was tested, and the concept of *longitudinal scans* was introduced. Originating from the idea of covering as many different downstream volumes as possible while keeping the corresponding configurations as comparable as possible, longitudinal scans use two magnetic field settings and only scan over different downstream volumes by adapting the analyzing plane positions via wire electrode configurations. This concept is visualized in Fig. 6.4.

The KNM2 SAP measurement campaign featured a total of 19 settings including 8 longitudinal scan settings (4 wire electrode settings and two air coil settings), a Central AP setting, 3 SAP settings to be compared for usability in tritium scans and further test measurements for

---

[1] Downstream volume calculations performed for the entire detector, assuming no pixel cuts.

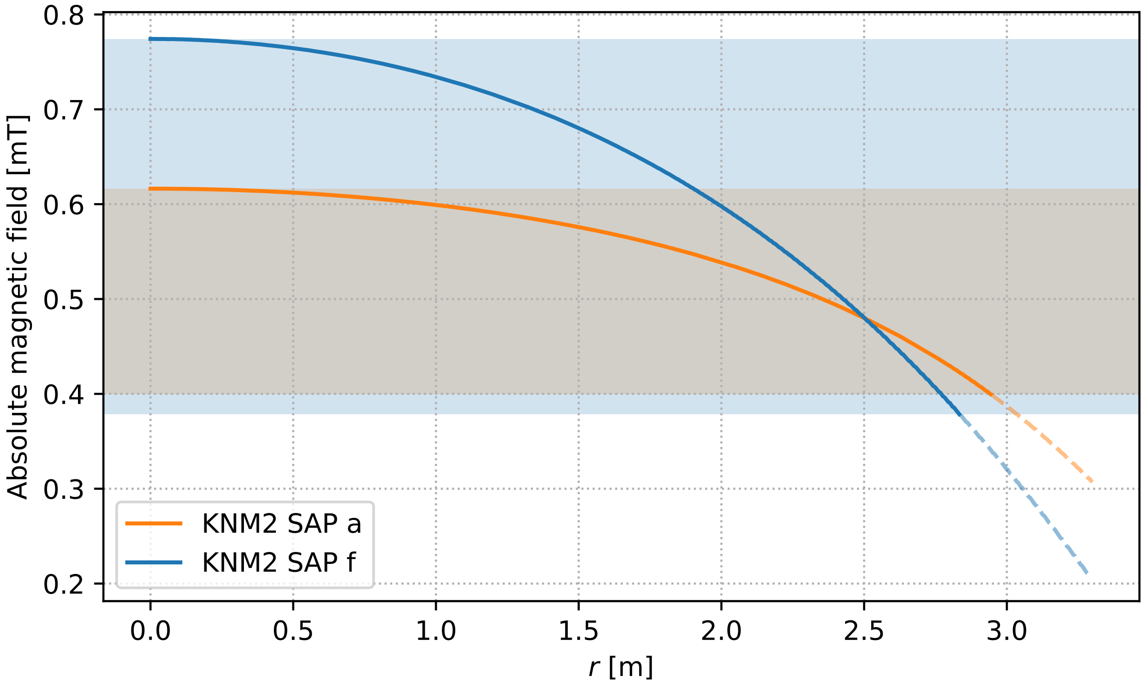

(a) Absolute magnetic field distribution.

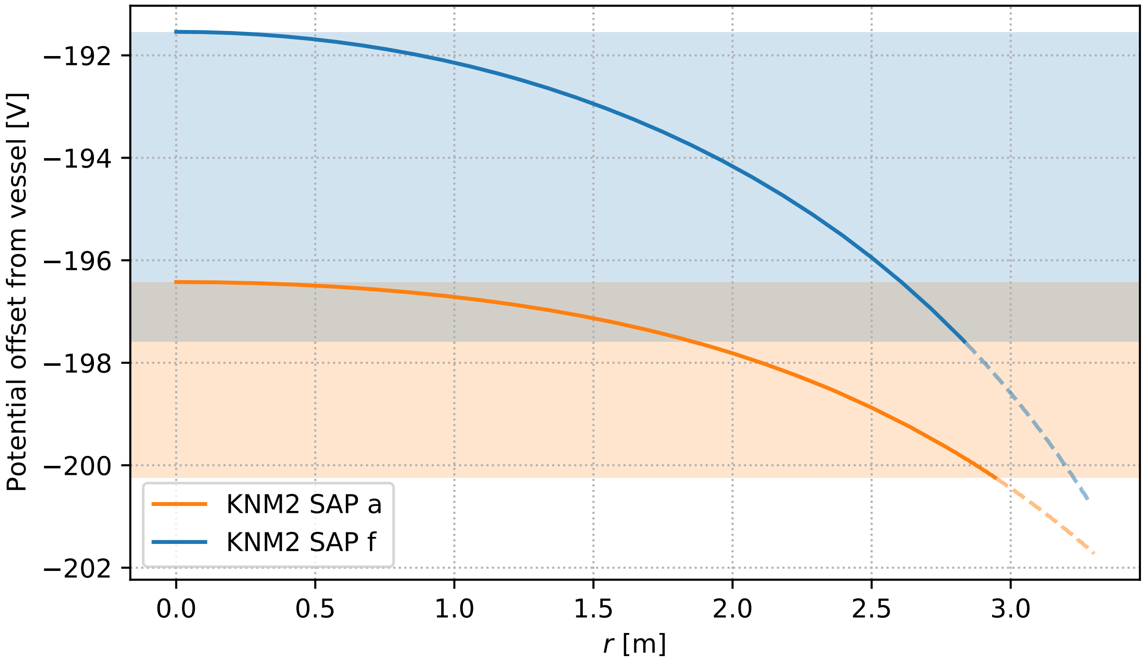

(b) Distribution of electric potential offset from vessel, simulated for a vessel potential of -18.41 kV.

Figure 6.2: Radial distributions of a) absolute magnetic field and b) electric potential over the analyzing plane for settings “KNM2 SAP a” and “KNM2 SAP f” in axisymmetric simulation. Dotted lines show the fields and potentials outside the fluxtube. Colored areas show the range of potentials and magnetic fields over the analyzing plane.

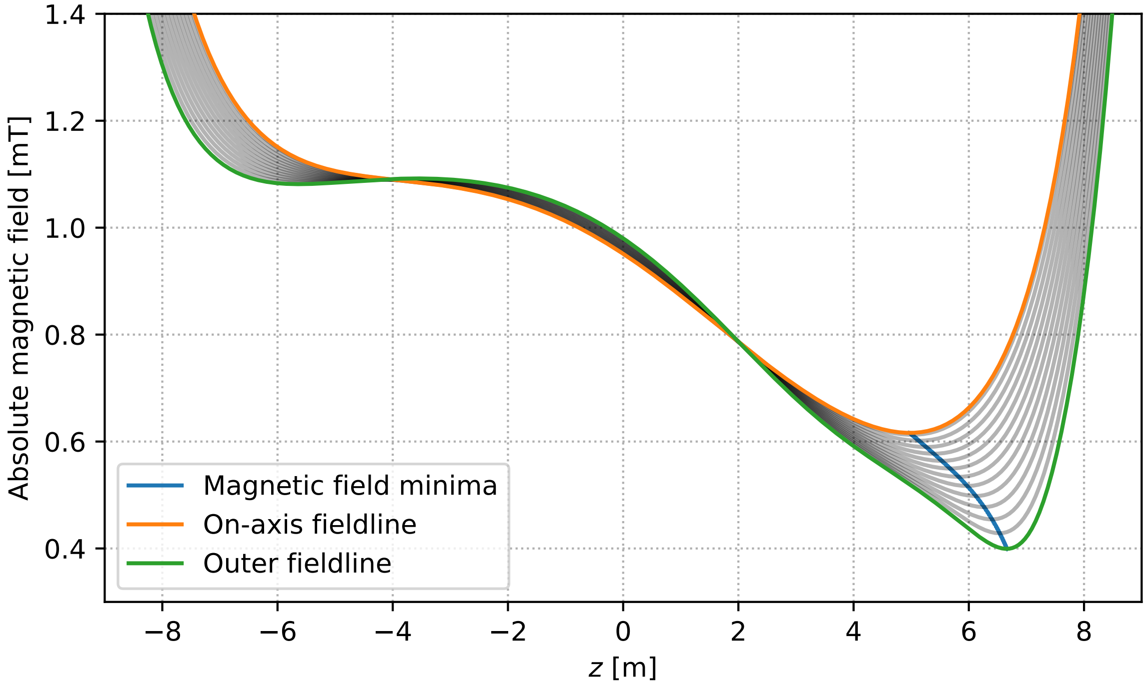

(a) Absolute magnetic field.

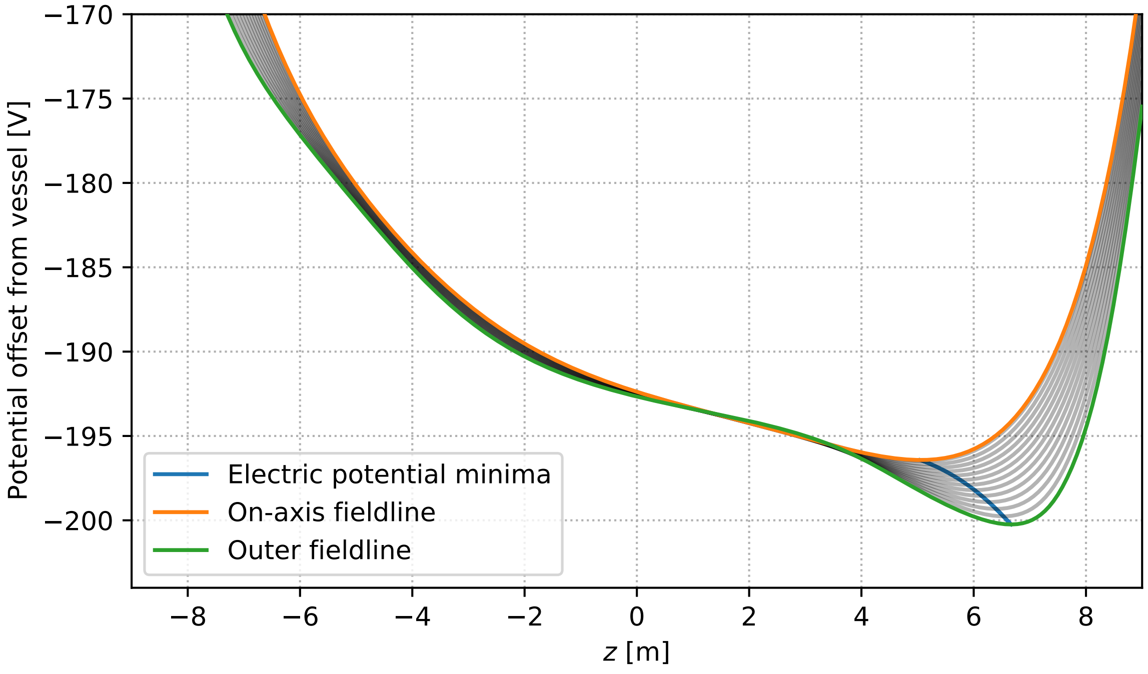

(b) Electric potential offset from vessel.

Figure 6.3: Magnetic field and electric potential of setting “KNM2 SAP a” inside the main spectrometer along different field lines. The on-axis magnetic field line and all field lines hitting the outer rims of detector pixels are shown. Minima for electric potential and absolute magnetic field are calculated along field lines. Calculation assumes axial symmetry.

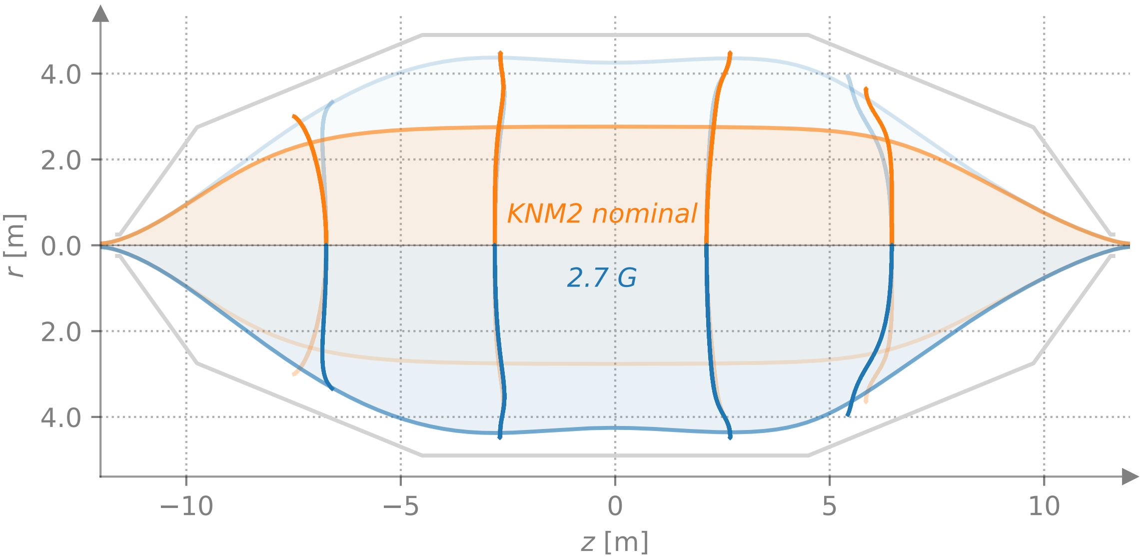

Figure 6.4: Longitudinal scan settings using "KNM2 nominal" and a 2.7 G air coil setting. Lines indicate outer fluxtube and position of electric potential extremum along field lines. The wire electrode settings used for "KNM2 nominal" and the 2.7 G setting are identical, the deviation in lines along extrema originates from different magnetic field line paths through the electric field along which the electric potential minima are searched.

information on the behavior of MS background. As in KNM1 SAP measurements, most simulations for these settings were performed during the course of this thesis in active discussion with the on-shift SAP team.

During the campaign and in the course of this thesis, the change of MAC-E filter settings was fully automated in the context of longitudinal scan measurements, enabling diverse measurements without manual operation. This allowed to re-run the longitudinal scan measurements in January of 2020.

KNM3 is the first measurement campaign to use an SAP setting in parts of their neutrino mass tritium scans. It employs a modification of "KNM2 SAP a" created during the course of this thesis to respect air coil hardware changes since KNM2 SAP measurements. Prior to the KNM3 measurements, additional studies on the SAP fields inside the spectrometer were performed outside this thesis for this setting via gaseous ^{83m}Kr in the WGTS and the E-Gun.

7 Background analysis

With the various measurements performed in the context of SAP, neutrino mass measurements and further background investigations, diverse datasets are available for analysis. This chapter focuses on the spectral and spatial analysis of measurements to discuss and extend the background model for the KATRIN experiment. Section 7.1 introduces the software used for this task. For the following analysis, Section 7.2 describes necessary detector pixel cuts. With the analysis procedure and details known, Section 7.3 gives an overview of the observed effects that are then further introduced in the following: Section 7.4 presents analysis of the ion peak effect, followed by Section 7.5 about temperature dependent background events from the FPD and Section 7.6 for the magnetic shielding effect in the MS. To close the introduction of observable effects, short remarks on further time dependencies of background rate are given in Section 7.7.

7.1 Technical realization

BEANS The KATRIN data toolchain, further described in [Kle14], allows to analyze event data locally using the `BEANS`[1] package inside the KATRIN Analysis and Simulations Package `Kasper`. The custom analysis source code compiled against this package is called a *`BEANS` script*. `BEANS` includes a variety of pre-defined, chainable analysis tasks and it is possible to create own tasks in `BEANS` scripts, making it the default tool for KATRIN event analysis. It does however iterate over every single data point. For all measurements discussed in the following, the detector is used in energy mode, where each data point corresponds to an event registered by the detector [Ams+15].

For the following analysis, multiple dimensions of the measured datasets are of interest: The energy histogram measured by the FPD can be regarded. For further analysis, events outside a given *Region of Interest* (ROI) can be discarded. Additionally, the rate per pixel and ring can be analyzed and specific pixels can be excluded. Finally, multiple data files, called *runs*, can be combined and compared against other run combinations.

---

[1] `BEANS` is a name based on the wording *Building Analysis Sequence.*

ratedownloader Parsing runs multiple times for various data combinations and ROI and pixel cuts can be slow, since the `BEANS` script has to repeatedly iterate over all corresponding events. Therefore, during the course of this thesis, `ratedownloader`, a custom, advanced `BEANS` script was created that pre-bins the events of a given run or subrun or a combination of both into JSON formatted files. This implies that if edges of ROI cuts performed with data from these JSON fiels are not coinciding with bin edges, effective ROI cut edges might be shifted insignificantly towards the nearest bin edges.

kamura A small Python script can then load these JSON files generated by `ratedownloader` into a new GUI named `kamura`, the KATRIN multidimensional rate analysis tool. With `kamura`, for all given datasets, the energy histograms and counts per pixel are visualized together with the rate trend over the included settings. Each of these visualizations is interactive and allows cuts on the data shown in the other views: Pixels can be activated and deactivated, ROIs can be selected and a box selection and deselection tool allows to include and exclude loaded runs. An additional non-interactive figure shows the rates per pixel averaged over each ring. The high interactivity of `kamura` comes with the usual cost of easy overestimation of outliers or random patterns in the datasets, an effect known as *pareidolia*. Due to the straight-forward design of `ratedownloader` and `kamura`, the use of new datasets is simple and pareidolia can therefore be mitigated by comparing an observed pattern over various independent datasets.

Technology-wise, `kamura` is a small Python3 package based on Python3, PyQt5 and PyQtGraph similar to `gui_sap`, and it uses `FPDmap`, a Python package for pixel-wise rate visualization provided by `Kasper`. For `kamura`, the Matplotlib [Hun07]-based `FPDmap` was extended, e.g. by implementing interactivity and pixel numbers.[2]

kali-slowcontrol-reader Finally, `Kasper` also provides the `kali-slowcontrol-reader`, which visualizes the readout of slowcontrol values during given runs. After adding a simple option to highlight the duration of runs in these plots, this is a quick and easy solution to check the evolution of e.g. the temperature at the detector or the main spectrometer vessel potential readout during a large set of given runs.[3]

This set of applications enables quick and interactive spectral, spatial and temporal analyses of measurement data, leading to investigations further presented in the following.

All uncertainties on background are, if not stated otherwise, propagated via Gaussian error propagation and assumed to be Poissonian. Therefore, errors on counts are calculated as the

---

[2] Associated `Kasper` merge requests: !389, !390, !394, !407

[3] Associated `Kasper` merge requests: !374

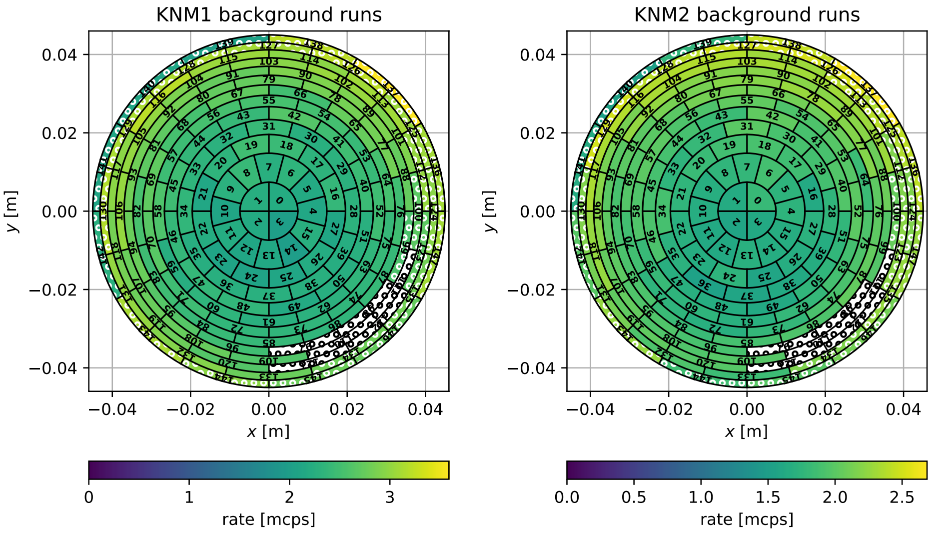

Figure 7.1: Pixel-wise rates for background runs of the KNM1 and KNM2 measurement campaigns in the 14 keV to 32 keV ROI. Dotted pixels are excluded from general analysis for the measurement campaigns respectively. White indicates hairy pixels.

square root of counts. This is not fully valid, since Radon background electrons occur in time-focused bundles, effectively slightly raising the uncertainty on rates for short measurements.

7.2 Pixel cuts

Pixel cuts are performed out of multiple reasons: The FPD wafer used for KNM1 and KNM2 measurements features 6 pixels with an elevated intrinsic background. Further pixels are excluded for alignment/shadowing, meaning the rate of signal electrons on these pixels is lower than the average rates per pixel for the innermost 8 pixel rings by more than 1 %. Around pixel 100, the shadowing comes from the FBM.

The selection of pixels included in neutrino mass analyses are called *golden pixel selection*. Between the measurement phases KNM1 and KNM2, pixel 99 was removed from the FBM cut and pixel 113 was added to the alignment cut.

The pixel distribution of background during KNM1 and KNM2 measurement campaigns is shown in Fig. 7.1. While alignment issues cannot be seen by eye, the top left pixels of the outer detector ring shows intense shadowing in both campaigns. For KNM1 it could be seen that the rates measured at pixels 140 and 141 are insensitive to the main spectrometer potential and consequently also the tritium signal electrons. The kinetic energies of electrons hitting these pixels are discussed in the next section. The FBM shadowing is not observed in background electrons, as the FBM is positioned inside the CPS and therefore not affecting the propagation of background electrons from the main spectrometer to the FPD.

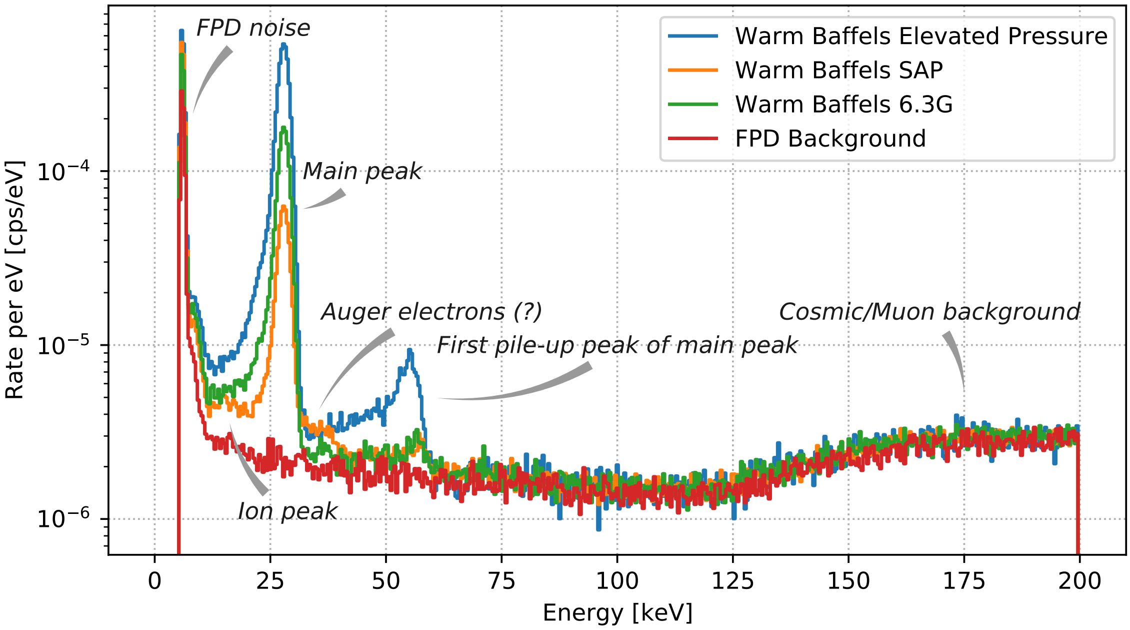

Figure 7.2: Typical histograms of electron energies measured at the FPD. FPD background was measured with deactivated PAE. The pre-KNM3 "Warm Baffles" measurement series uses warm baffles to study the properties of increased radon background. While "SAP" uses a slight variant of configuration "KNM2 SAP a", "6.3G" uses the nominal central AP setting of neutrino mass measurement campaign KNM3b. Measurements were performed independent of this thesis at the end of March 2020 with a new wafer. For this figure, 499 bins from 0 to 200 keV are used with events from all pixels.

7.3 Background electron energies at FPD

Looking at the energy distribution of background electrons, exemplarily shown in Fig. 7.2, multiple background components are visible:

FPD noise Being mostly visible for energies $\lesssim 10\,\mathrm{keV}$, the FPD electronic noise background is most significant in a region not overlapping with other background or signal electrons. It will be further discussed in Section 7.5.

Ion peak Roughly between 14 keV and 23 keV, an additional background peak is observed. Investigations with a similar peak in this region were presented end of march 2019, where the peak was shown to linearly shift with the PAE and therefore originating from negatively charged particles [Ann19]. It is further known that the height of this peak varies over time [San19]. Its current explanation and origin of its name are negatively charged ions originating from the main spectrometer. Further research on this energy region will be shown in Section 7.4.

Main peak Main spectrometer background and signal electrons arrive with approximately the accumulated energies of spectrometer vessel potential and PAE, since the energy of electrons inside the main spectrometer reaching the FPD does not exceed the 1 keV range for most of the electrons that could reach the detector.

Auger electrons (?) A small peak can be observed in e.g. the visualized SAP background measurement spectrum up to approximately 10 keV above the main peak. The peak position resembles very closely the second background peak from Section 3.4 observed in Mainz, where the background source was expected to be Auger electrons originating from surfaces inside the spectrometer.

First pile-up peak of main peak When multiple electrons arrive at nearly the same time on the same FPD pixel, they cannot be distinguished and are registered at the combined energy. The most pronounced pile-up peak consists of two electrons from the main peak arriving simultaneously. For background measurements, this effect is very low and consequently neglected.

Cosmic/Muon background Throughout the entire energy range, natural background is measured, mostly from muons. It is relatively constant over different measurements, so that one FPD background measurement series can be used to characterize this background component.

Since most signal electrons are captured around the main peak, ROI cuts from 14 keV to 32 keV are used for $m_{\overline{\nu}_e}$ analysis, with additional correction from excluded pile-up peaks.

7.4 Ion peak investigations

To investigate the ion peak, the `kamura` tool allowed the quick analysis of various measurements. While the KNM2 neutrino mass measurements were chosen to be shown in Fig. 7.3, the reader is referred to Appendix B for similar analyses for more datasets. Several visualizations contain reduced main peak and significantly elevated background for the ion background region in the top left region of the outer pixel ring and elevated rates at pixels directly above the central pixels. This observation initiated further analysis, since background effects are assumed to have a radial dependency, but no localized pixel dependency.

With custom pixel selections, histograms of pixels with elevated counts can be compared, as visible in Fig. 7.4. It can be seen that the ion peak is significant in inner rings and outer pixels

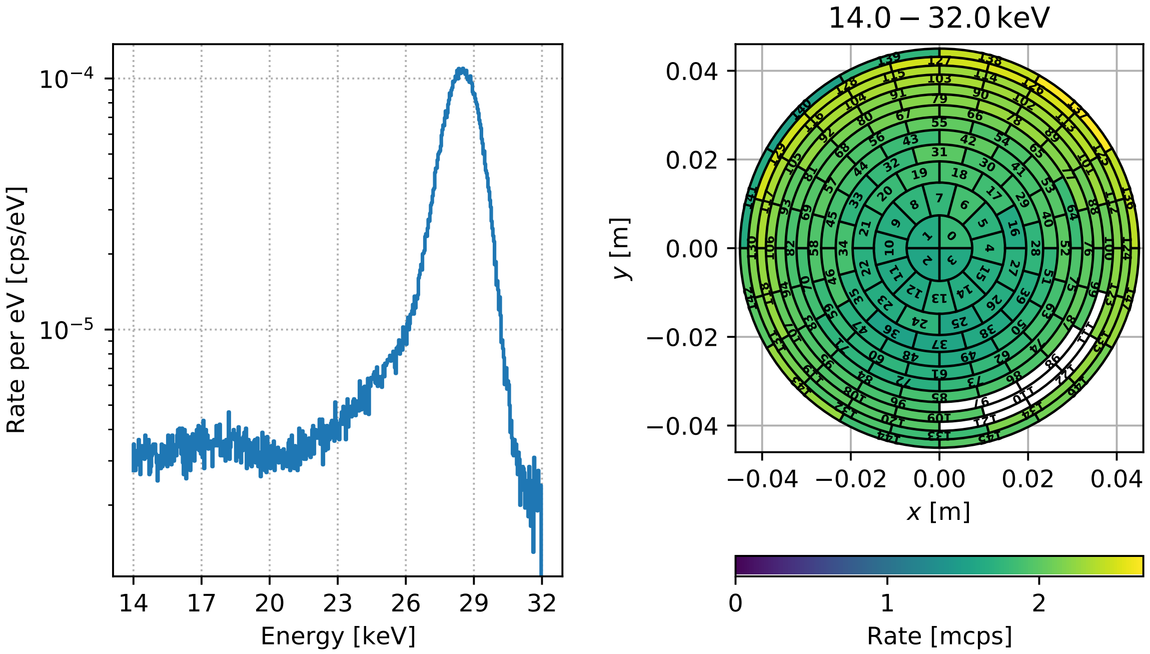

(a) Full energy range considered in terms of an FPD histogram with 499 bins from 14 keV to 32 keV, and the according distribution of pixelwise rates. Hairy pixels are excluded

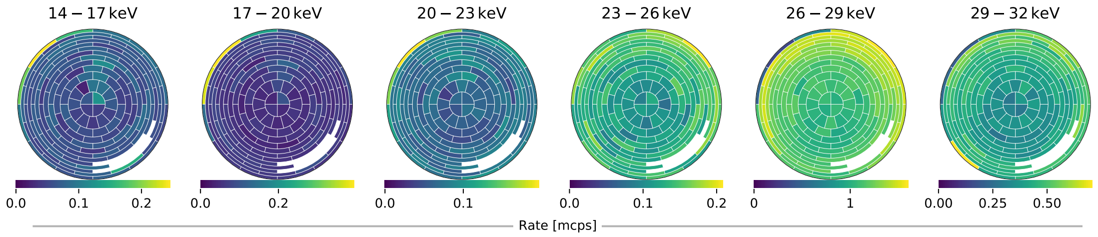

(b) Same distribution as a) for 6 sequential ROI cuts

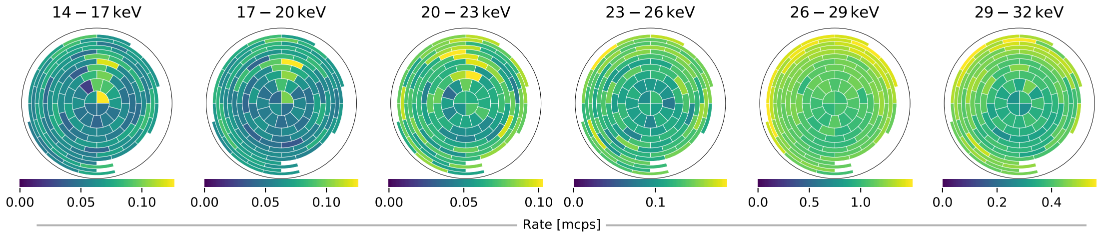

(c) KNM2 golden pixel selection

Figure 7.3: KNM2 $m_{\overline{\nu}_e}$ campaign background in FPD plots for different ROIs around ion peak and main peak.

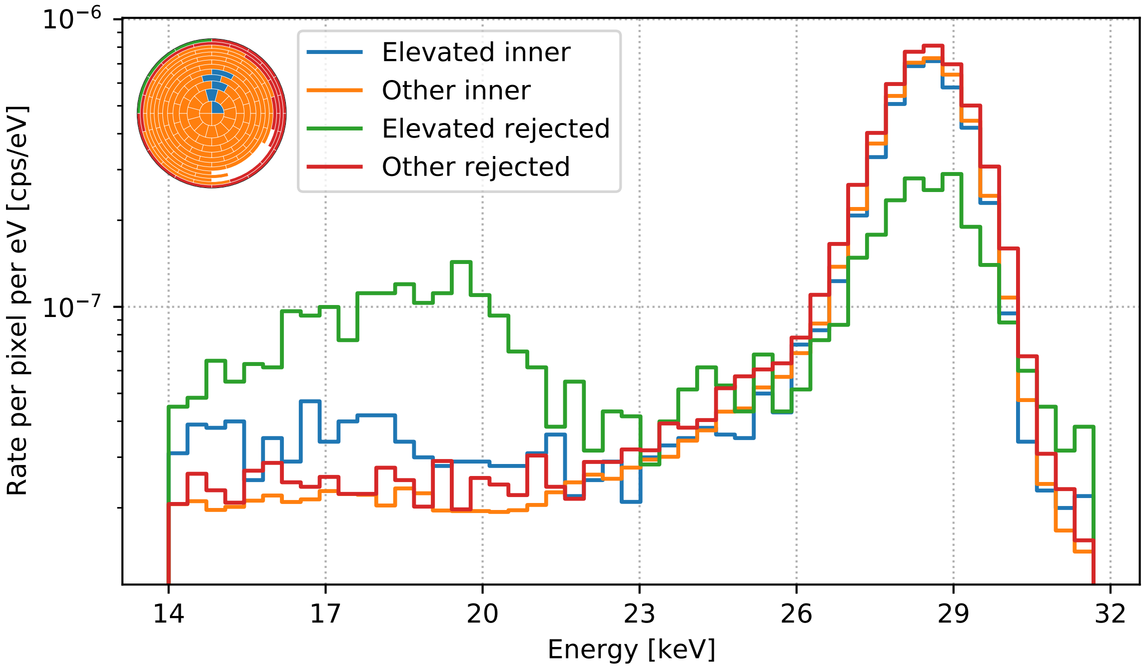

Figure 7.4: KNM2 $m_{\overline{\nu}_e}$ campaign background detector energy histogram by pixel selections. Selected are 3 pixels in the outer ring and 5 pixels inside the KNM2 golden pixel selection region that show elevated rates at energies of the ion peak. To increase statistics per bin, each 10 bins are combined, dropping the last 9 of the 499 bins from 14 keV to 32 keV. The uncertainty intervals are drawn assuming a Poissonian $\sqrt{x}$ uncertainty. This might underestimate uncertainty due to time focused radon/ion background, and it does not account for the bias by the pixel selection process.

for energies ranging from roughly 14 keV to 23 keV, the outer pixels show even an elevated background slightly beyond 23 keV. With the pixel selections from Fig. 7.4, the elevated inner pixels show a total rate per pixel of $(2.93 \pm 0.10) \cdot 10^{-4}$ cps for a ROI from 14 keV to 23 keV, in comparison to a rate of $(1.965 \pm 0.018) \cdot 10^{-4}$ cps for other inner pixels. For the rejected pixels, the elevated pixels show a rate of (7.03 ± 0.21) cps in comparison to $(2.25 \pm 0.04) \cdot 10^{-4}$ cps for other rejected pixels.

It has to be noted that the selection process of these pixels introduces a bias in this completely data-driven analysis. Therefore, this effect was studied with different run and subrun selections and further datasets, more of which are presented in Appendix B. Also, none of the datasets showed pixels with visible rate reduction in the ion peak region. Hence, this is a real effect. Further research is needed on its exact origin.

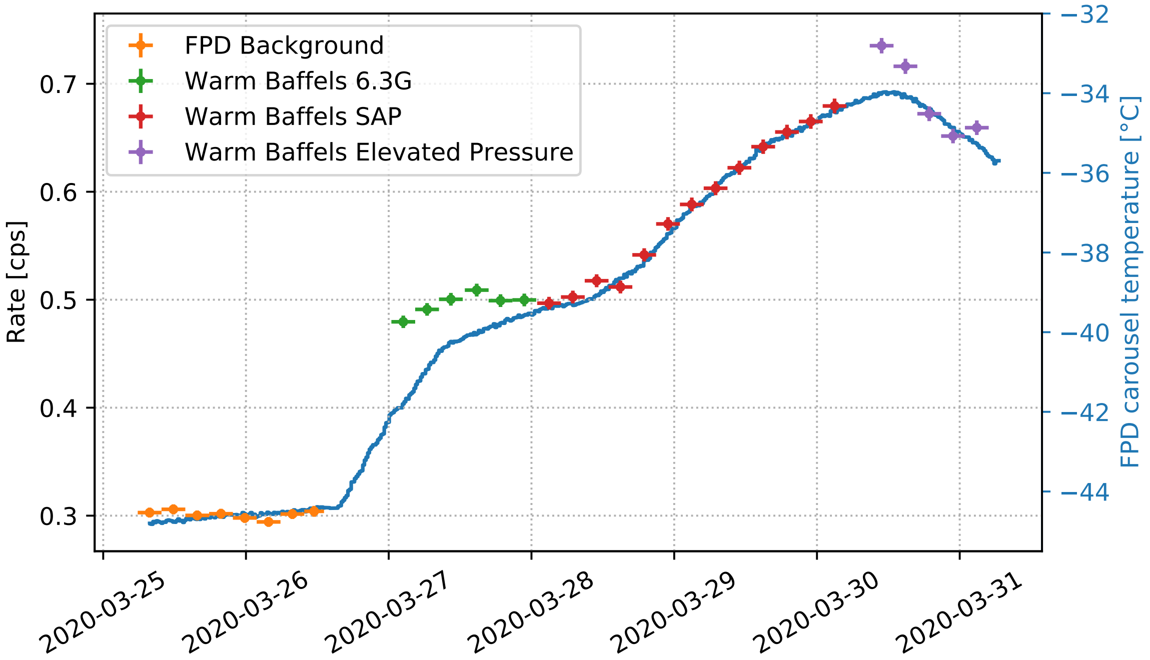

Figure 7.5: Background rates for pre-KNM3 “Warm Baffle” series at ROI 0 keV to 10 keV overlaid with FPD carousel temperature. Data points are runs, horizontal error bars indicate run lengths, vertical errorbars are Poissonian $\sqrt{x}$ uncertainties.

7.5 Temperature dependency of FPD noise

Having `kamura` as interactive analysis tool at hand, a continuous change in noise rate for FPD counts with energies $< 10\,\mathrm{keV}$ was observed, shown in Fig. 7.5. Comparing this to the the FPD electronics temperature showed a partly linear relation between electronic noise and temperature. This lead to the observation of a $> 10\,^{\circ}\mathrm{C}$ change in the principally stabilized FPD electronics temperature.

For energy regions important for background investigations, the FPD electronics temperature theoretically affects the detector resolution. In practice, comparing the main peak widths for the combined first and last 4 runs of the pre-KNM3 “Warm Baffle” series, this was insignificant, and hence is disregarded in further analysis.

7.6 Magnetic shielding in main spectrometer

For lower magnetic field settings, the magnetic shielding effect is lower, leading to negative ions and high-energy electrons being able to enter the magnetic fluxtube non-adiabatically. This increases the background of settings at 35 % and 60 % magnetic field strength. To quantify this effect, during KNM1 SAP measurements, the nominal KNM1 setting was measured at 35 % magnetic field strength. For a detector ROI from 14 keV to 32 keV and the KNM1 golden pixel selection, this leads to an increase in background rate from 291.5 ± 0.8 mcps during the KNM1 $m_{\overline{\nu}_e}$ campaign at 70 % to 311 ± 13 at 35 % magnetic field strength in KNM1 SAP. A more significant increase can be found for an SAP setting measured during KNM1 SAP measurements for both 70 % and 35 % magnetic field strength (IDs 1 and 5), where the background increased from (136 ± 4) mcps at 70 % to (174 ± 10) at 35 % magnetic field strength. This is explained by the close proximity of the magnetic fluxtube to the spectrometer walls for the SAP setting, which is the origin of high-energetic electrons and ions.

7.7 Time-dependent effects

Further efforts in background reduction like baking of the main spectrometer, installation of "subcooling", an additional cooling stage for MS baffles, but also an observed continuous time dependency of background rates makes it necessary to consider different measurement campaigns separately for the task of creating a background model. From KNM1 to KNM2 $m_{\overline{\nu}_e}$ campaigns, the background rate was reduced from (288.4 ± 0.8) mcps for KNM1 to (221.3 ± 0.6) mcps for KNM2, using the 14 keV to 32 keV ROI and a pixel cut with the same pixel selection[4].

---

[4] The pixel selection consists of coinciding KNM1 and KNM2 golden pixels.

8 Background modeling

To reduce spectrometer background with the SAP method in the KATRIN experiment, precise knowledge on the properties of measured background are important. In Section 8.1, domination of background electrons starting with negligible energies is assumed in the test of the downstream volume dependency and two approaches for background models. Section 8.2 then uses a model of homogeneous background event distribution inside the spectrometer to demonstrate the effects of finite background energies on a retarding potential dependent background slope.

For high-energetic primary Radon electrons or e.g. Auger electrons emanated from the walls, further effects have to be considered that are out of the scope of this thesis. These electrons are mostly magnetically trapped inside the main spectrometer and might leave this trap non-adiabatically as described in Section 4.1, and might also enter the magnetic flux tube due to non-adiabatic behavior in combination with large cyclotron radii. Model building with a full analysis on the effects of the measured SAP settings are left to be investigated in the future.

8.1 Low-energetic background electrons

The KATRIN background event rate is assumed to be dominated by its low-energetic Rydberg component. With its sub-eV electron energies, this background component is assumed to be reflected completely at the potential barrier of the analyzing plane, while the magnetic moment of these low-energetic electrons is so low that a magnetic mirror effect further downstream e.g. at the pinch magnet is not possible for these electrons. Therefore, the background is assumed to be significantly dependent on the downstream volume, the volume enclosed by the fluxtube downstream the analyzing plane. This dependency is studied in Section 8.1.1. For the case of spatially heterogeneous background event density inside the main spectrometer, in Section 8.1.2 models use a main spectrometer volume with segmented background event densities. Section 8.1.3 follows with a Monte Carlo-simulated background density distribution assuming exponential probability of the decay of a Rydberg atom with respect to the distance from its point of emission on the spetrometer walls.

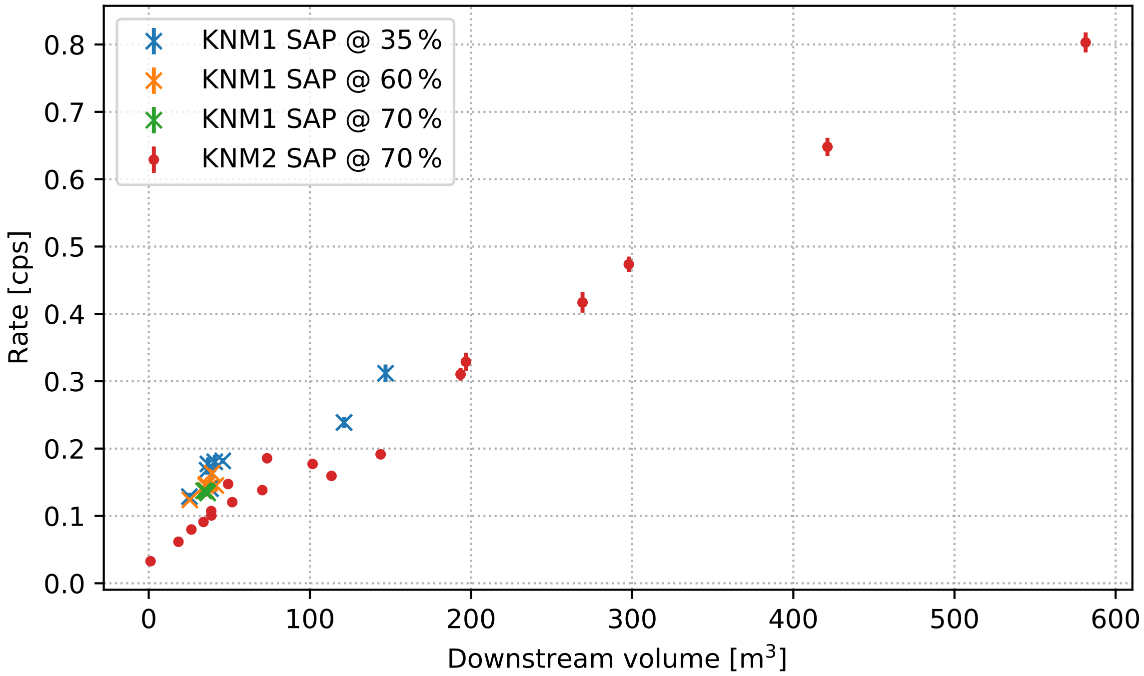

Figure 8.1: Measured rates against downstream volume for SAP measurement campaigns during KNM1 and KNM2. Calculated downstream volumes include volume reduction by excluded detector pixels. Calculations are performed axisymmetrically. Only pixels in both KNM1 and KNM2 golden pixel selections were used.

8.1.1 Direct downstream volume dependency

In Fig. 8.1, the downstream volume dependency of KNM1 and KNM2 SAP measurements are visualized. It can be seen that the plot of measured rate against downstream volume shows a high linearity, confirming the assumption that background electrons are emitted inside the spectrometer vessel volume. This also allows to give rough estimates on the performance of new main spectrometer field settings by simulating their downstream volume. Data points from KNM1 SAP measurements have overall rates that are higher than data points from KNM2 SAP measurements. KNM2 SAP measurements further feature a wider range of volumes and settings.

This allows two conclusions for further investigations: First, the downstream volume is an excellent indicator for the background of a given SAP setting. Especially the low volume part of Fig. 8.1 below a downstream volume of 50 m^3 shows rather linear behavior for KNM2 SAP measurements. Second, the KNM2 SAP measurements fulfill their goal of providing a more complete image on the behavior of various distinct settings, and are therefore used for the following background modeling.

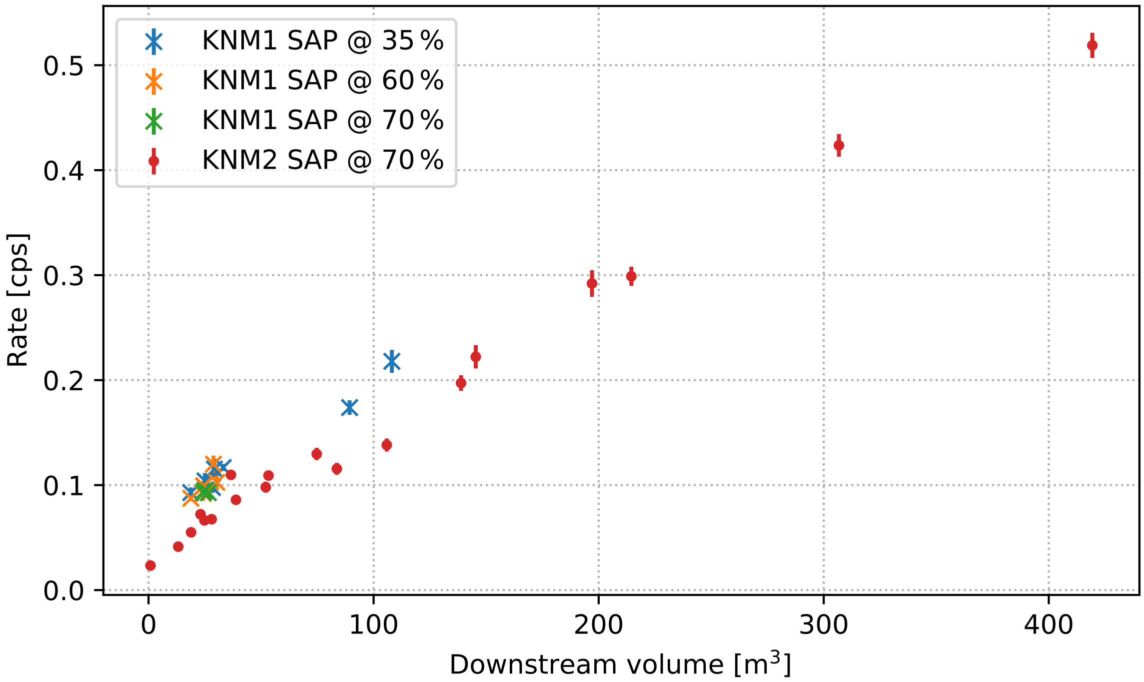

Figure 8.2: Measured rates against expected downstream volume assuming a radial detector shift by 5 mm. Settings from KNM1 SAP and KNM2 SAP measurement campaigns are shown. For the off-axis fluxtubes, 74 field lines are traced per outer limit of each detector ring. Outer 5 rings are rejected, since they contain rejected detector pixels and therefore needed a full 3d tracking. For comparison, a variant of Fig. 8.1 with the same pixel cut can be found in Appendix C.

During KNM1, the non-Poissonian background contribution was measured to be lower than during the KNM2 measurement campaign, which might increase the dependency on trap quality and thereby reduce the downstream volume dependency for KNM2 SAP measurements.

The FPD is known to be misaligned. Two preliminary analyses performed by fitting lines from CKrS measurements for the recent neutrino mass measurement campaign “KNM3” showed a radial offset from the center by 4.1 mm and 4.7 mm respectively [Ale20]. To observe possible implications of this shift to the downstream volume dependency, Fig. 8.2 shows the downstream dependency assuming an FPD shift of 5 mm off-axis. In comparison to Fig. 8.1, the overall downstream dependency is similar, which allows to conclude that for this analysis, the detector offset can be neglected. The largest differences between Fig. 8.1 and Fig. 8.2 arise from the different detector pixel selection, not the detector offset. This can be seen via comparison to Fig. C.1.

Due to the relatively linear downstream volume dependency, a rather homogeneous spatial background event distribution throughout the spectrometer can be assumed. To further

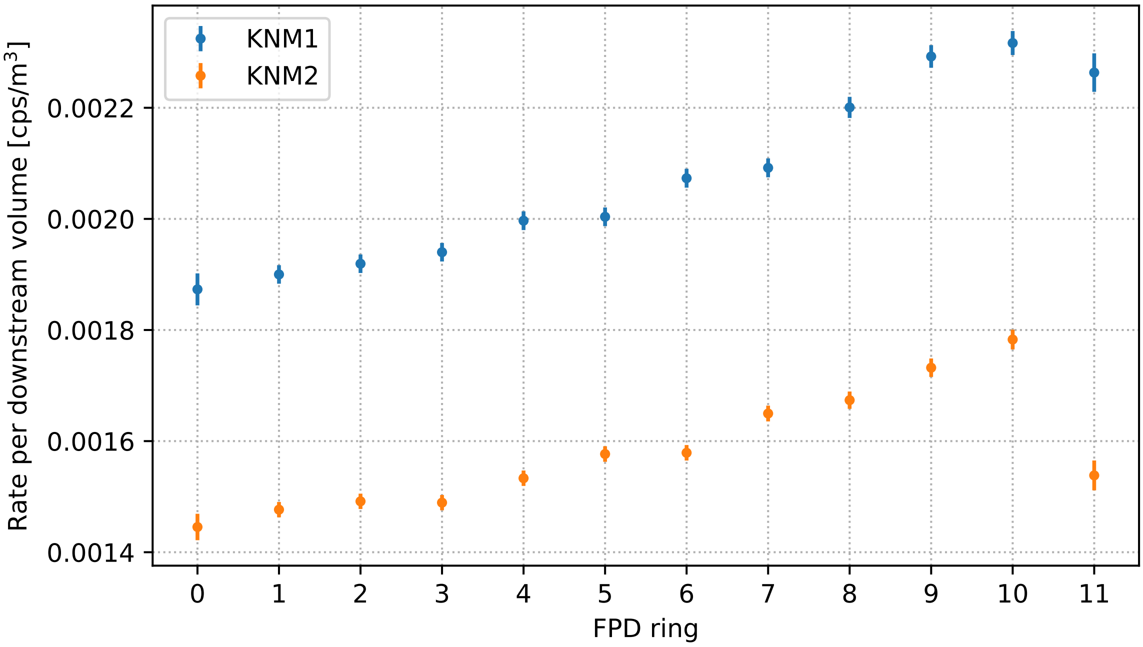

Figure 8.3: Ringwise rate per downstream volume measured in background subruns of KNM1 and KNM2 tritium measurements. Only detector pixels in both KNM1 and KNM2 golden pixel selections were used.

investigate the spatial distribution, the ringwise dependency on downstream volume can be analyzed. In Fig. 8.3, the rates per downstream volume covered by each ring during KNM1 and KNM2 neutrino mass background measurements are plotted. A similar radial dependency can be seen in both KNM1 and KNM2 tritium measurements, suggesting an increased background coming from the spectrometer walls. Especially ring 11 does not follow the pattern given by the other rings, since it only contains a very limited amount of detector pixels in the golden pixel selection which are in a region of relatively low rates, as can be seen in Fig. 7.1.

8.1.2 Segmentally homogeneous background

To study the spatial background event distribution in the main spectrometer vessel, for following models, the vessel is divided it into multiple segments with different homogeneous background event densities c_i, $i > 0$. These segments are defined by cuts along surfaces of equal minimal distance to the spectrometer walls and cuts along equal z. Additionally, a constant background c_0 is assumed for all given measurements.

To test the models, data points $d_j, j \in 1, ..., C$ are defined by the ring-wise background count rate with the corresponding Poisson uncertainty e_j, reduced by the estimated detector background rates of a dedicated measurement.[1] For the errors on the measured rates, the square root on counts is divided by the measurement duration. For the subtraction, Gaussian error propagation is used.

For each data point, a boolean 2d map for the $z - r$ plane is created, identifying parts inside the downstream volume of each detector ring for a given setting. Additional maps identify different segments in the model.

The total rate r_j estimated from a model c_i is calculated by construction of a spatial map of spectrometer background event distribution with the rates c_i at positions given by detector segment maps, with subsequent summing over positions given by the boolean map corresponding to d_j.

Coefficients c_i are found by minimization of

$$\chi^2 = \sum_{j=1}^{C} \frac{(r_j - d_j)^2}{e_j^2} ,$$

via the algorithm L-BFGS-B [MN11] through its SciPy [Vir+20] interface.

In the following, maps with a resolution of 200 segments along z between -7.110 m< z <13.925 m and 100 segments in r direction in the range $r < 4.374$ m are used, since this covers all fluxtubes covering the full FPD for all KNM2 SAP measurements.

Fits to a model with only cuts along z, another model with only cuts along distance to vessel walls and a model combining both are shown in Fig. 8.4. As cut positions along z, -1 m and 4 m are used, while for the vessel distances, 2 m, 3 m and 4 m are used. These values were selected to cover each segment with at least one data point, while areas described by more data points are also segmented further. It can be seen that model a) with only cuts along given spectrometer vessel distances shows the already observed radial dependency of background rate. The decrease of the reduced χ^2 value for model c) with additional longitudinal segmentation over model a) might indicate an unequal distribution of background events along the z axis of the main spectrometer.

Further investigation of the exemplary residual distribution of the most segmented model c) in Fig. 8.5 indicates that especially for one field configuration, setting with ID 8, shows an increased background rate compared to model c). This setting is a variation of the setting with setting ID 1 (“KNM2 SAP a”) with steeper electric potential on the upstream side. A possible explanation would therefore be an increase of secondary electron background from trapped electrons that are retarded further downstream in the setting with ID 8 in

---

[1] The detector background measurement was performed on 13th January 2020. The corresponding elog is `https://ikp-neu-katrin.ikp.kit.edu/elog/KNM2/173` .

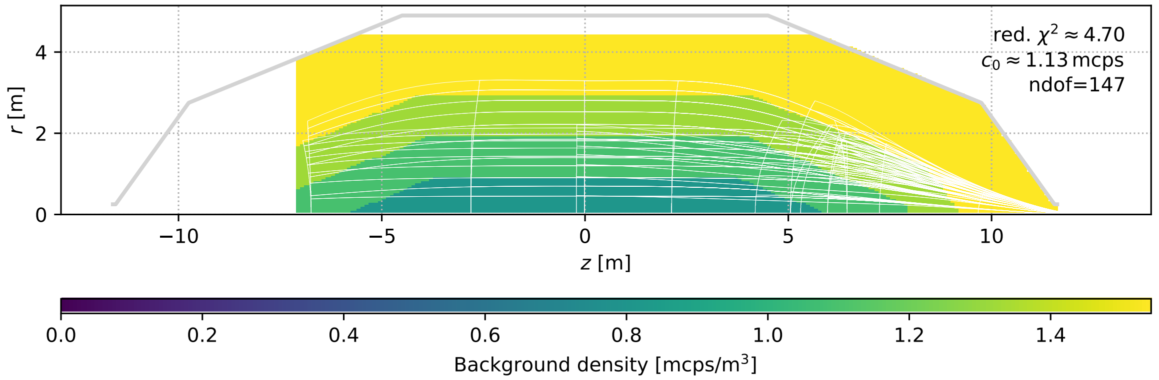

(a) Three surfaces with equal minimal distance from the walls of 2 m, 3 m and 4 m divide the spectrometer into four volumes

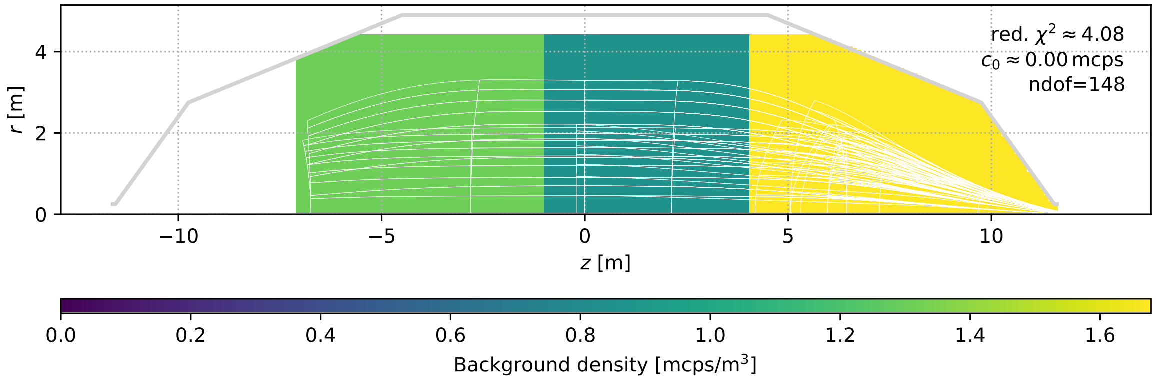

(b) Two surfaces with equal z of -1 m and 4 m divide the spectrometer into three volumes

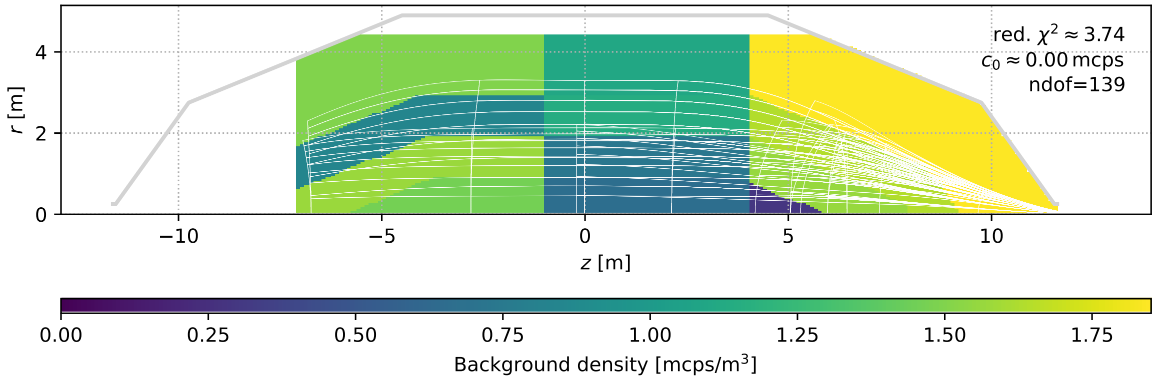

(c) Surfaces from a) and b) divide the spectrometer into 12 volumes

Figure 8.4: Background density distribution from fits of three models to KNM2 SAP measurement data. White lines indicate borders of volumes covered by a data point. Red. χ^2, constant background of each model and *number of degrees of freedom* (ndof) are indicated at the top right.

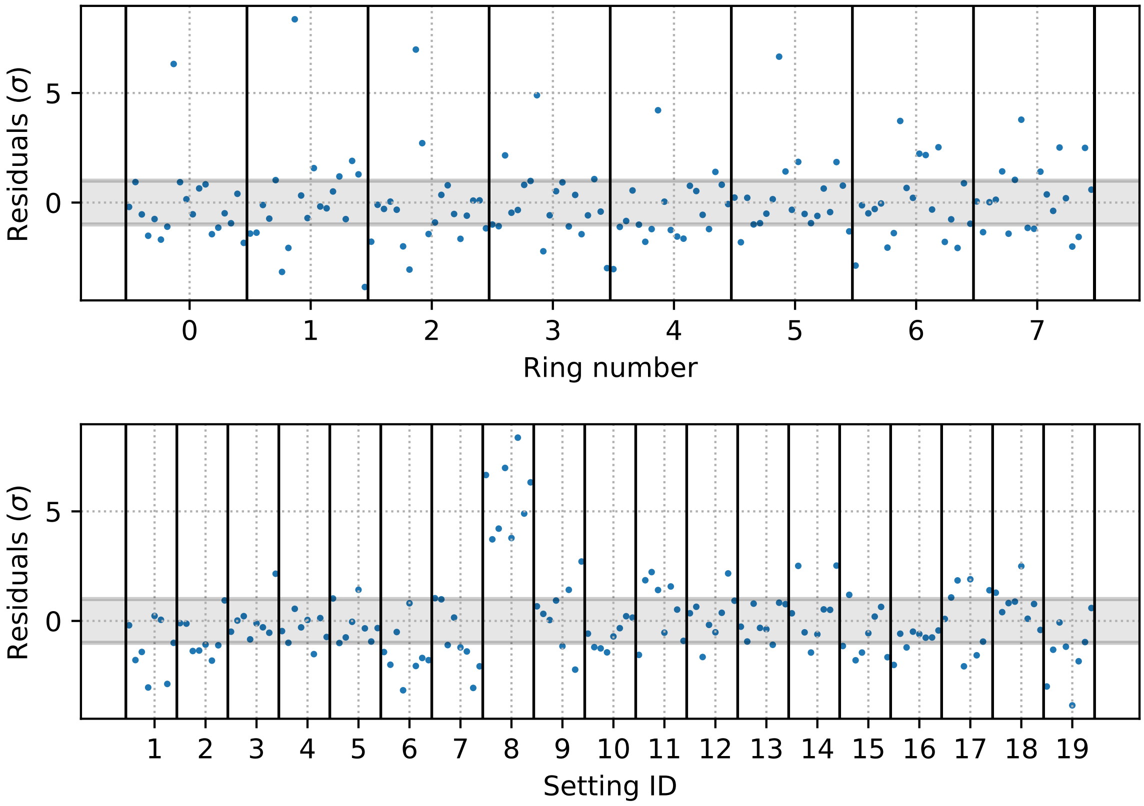

Figure 8.5: Standardized residuals for model c) from Fig. 8.4. Residuals are shown clustered by their respective fitted detector pixel ring and their setting.

comparison to the setting with ID 1, and hence a higher probability to ionize low-energetic electrons downstream the analyzing plane.

Similar residual plots and further information about these fits can be found in Appendix D.1.

8.1.3 Exponential falloff model

Rydberg atoms are emanated from sputter processes at surfaces (see Section 3.3). This model assumes the Rydberg atoms to be ionized during their propagation from the vessel walls into the main spectrometer volume, where the probability of ionization through thermal radiation is described by exponential falloff w.r.t. their propagation distance. This extends a qualitative model by Dominic Hinz.

For this analysis, traveling lengths λ are specifically sampled from probability $p(\lambda) = \exp\left(\ln(2)/b \cdot \lambda\right)$ with the free parameter b named “Half-life length”. The spectrometer model is symmetrical around $z = 0\,\mathrm{m}$, allowing background density maps to be generated in the $|z| - r$ plane. To generate these density maps, the sampled traveling lengths are applied to 1 million individual particles in a 3d simulation that is then binned into 100 x 100 bins in the $|z| - r$ plane. A

Monte Carlo approach was chosen over a numerical approach because it enables easy implementation of custom emission directions. With this method, the 3d emission direction of the particles can be isotropic as well as sampled from the simulated histogram of sputter directions shown in Fig. 3.6 a). The isotropic emission is performed by uniformly sampling $\cos(\theta)$ for starting angles θ, where the sampling from the assumed histogram is performed by splitting a uniformly random variable into parts corresponding to the value of the according histogram bin.

This model is scaled by a constant factor a. It is further possible to add a constant detector background offset c and a constant volume dependent background d.

Since only b is relevant for the Monte Carlo simulation, a scan over b is performed, where for each b, a simulation is run and subsequently the model parameters a, c and d are fitted to the data. The data is again reduced by the detector background rates and method used in Section 8.1.2. By this procedure, the least χ^2 of all models presented in this subsection were optimal for vanishing values for parameter c. This parameter is therefore excluded from the following analysis.

Using this technique, the red. χ^2 is then available as a function of b, plotted in Fig. 8.6. It can be seen that for the isotropic models a) and b), the minimal reduced χ^2 is at $b \approx 3.3\,\mathrm{m}$ and not significantly influenced by d. There, the minimal red. χ^2 is just slightly varying between the model including d and the model without it, because including d in a fit also reduces its number of degrees of freedom. Using theoretical sputter directions, the constant volume dependent background density d does lead to improvement, as it is non-zero throughout the regarded range of half-life lengths. Here the optimal red. χ^2 is found to be at $b \approx 0.7\,\mathrm{m}$.

The resulting background distributions for isotropic and theoretically based emission model configurations are shown in Fig. 8.7.

It can be seen that the isotropic emission Monte Carlo model without parameter d is a slight improvement over the previously presented, segmentally homogeneous model. Further, the Monte Carlo model is provided with a fundamental physics motivation. Its residuals, visualized in Fig. 8.8, show a distribution comparable to the residuals from the segmentally homogeneous model, also indicating that the setting with ID 8 has a higher rate than provided by the model. This underpins that the increased background rate in this setting cannot be described by the pure downstream volume dependency of low-energetic electrons.

Finally, it has to be noted that as outer rings without full detector pixel coverage are ignored in the model fitting, background events occurring especially close to the walls, like the assumed Auger background component, do not contribute significantly to the observed background rates and are therefore not relevant for the fit. Data from full coverage of the detector and

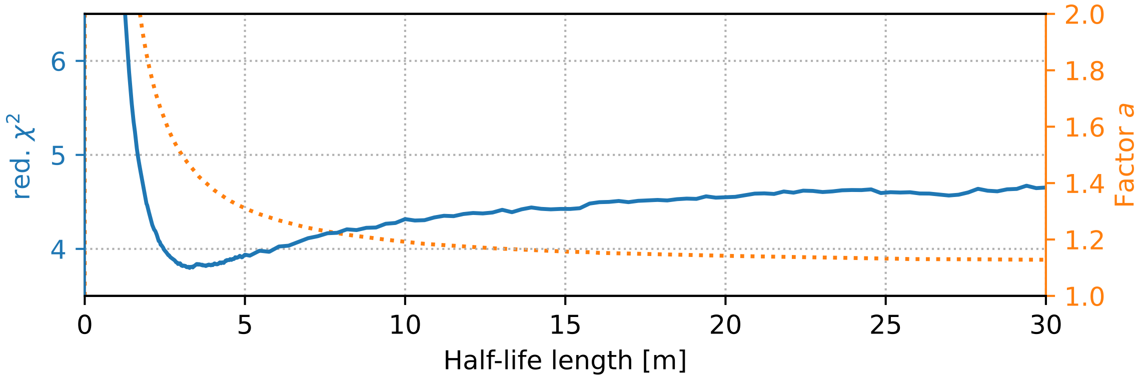

(a) Isotropic emission into vessel volume, ndof= 150

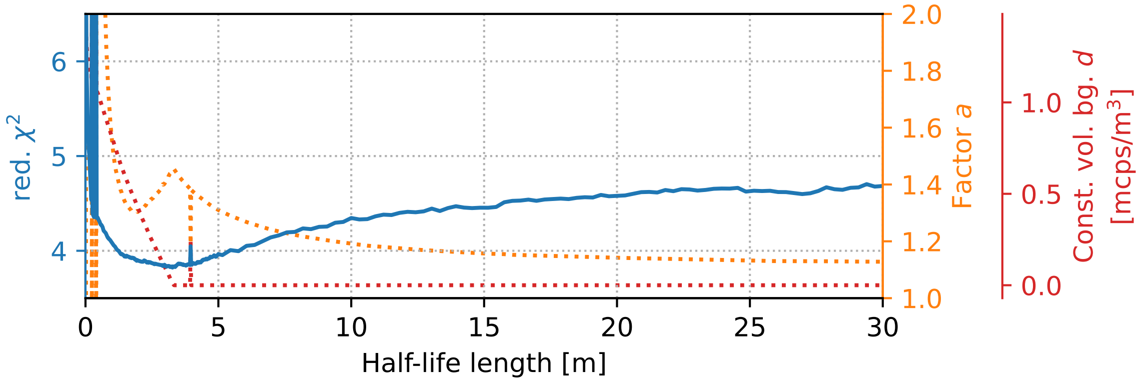

(b) Isotropic emission and constant volume dependent background density d, ndof= 149

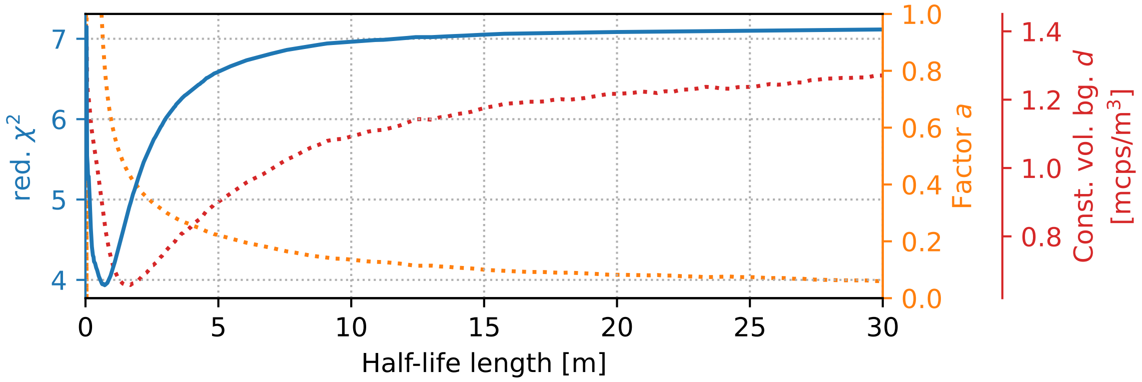

(c) Angular distribution assumed for sputtering processes and constant volume dependent background density d, ndof= 149

Figure 8.6: Best reduced χ^2 as a function of half-life length b. The *number of degrees of freedom* (ndof) for each red. χ^2 is given in the corresponding caption.

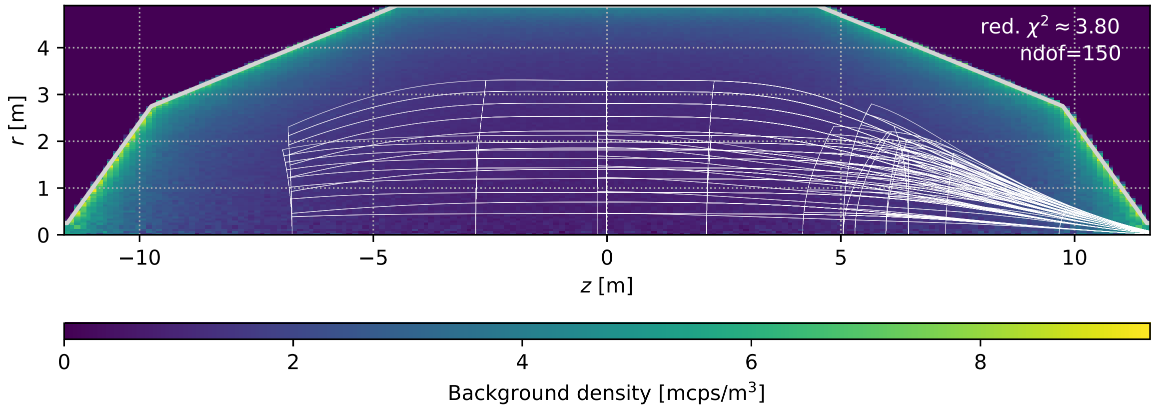

(a) Isotropic emission into vessel volume

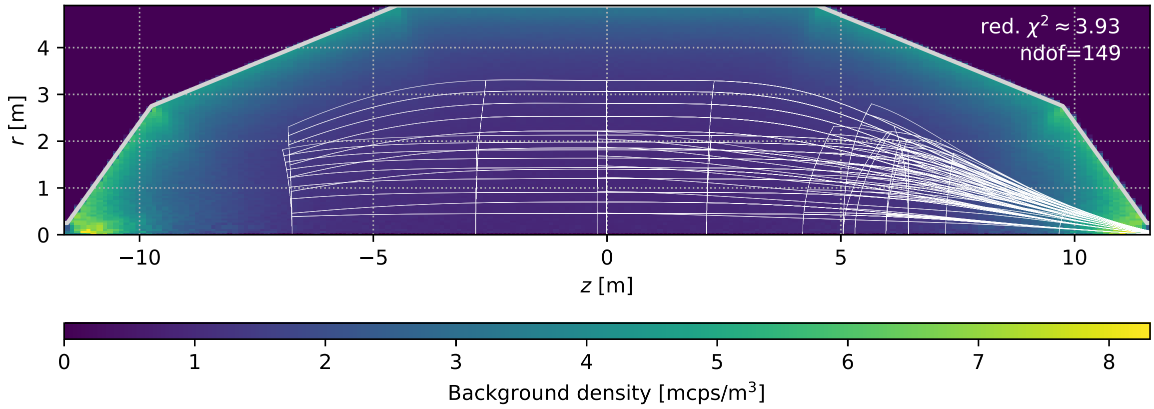

(c) Angular distribution assumed for sputtering processes and constant volume dependent background d

Figure 8.7: Background distribution, best red. χ^2 and corresponding *number of degrees of freedom* (ndof) from best fitting exponential falloff models a) and c) from Fig. 8.6.

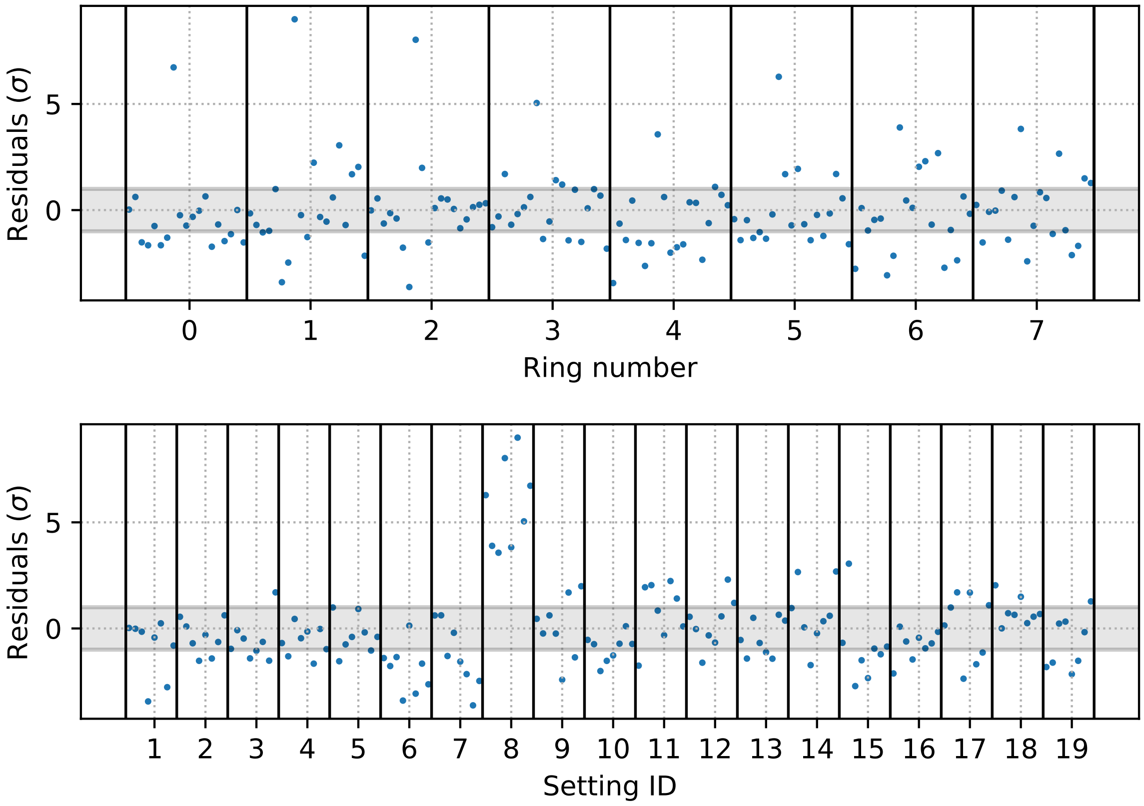

Figure 8.8: Standardized residuals for best fitting model from a) in Fig. 8.7. Residuals are shown clustered by their respective fitted detector pixel ring and their setting.

settings with fluxtubes close to the main spectrometer walls would allow a further test of this model.

Further residual plots and information on these fits can be found in Appendix D.2.

8.2 Background electrons with finite energies

A non-constant background event rate, i.e. dependent on the main spectrometer retarding potential, introduces a systematic effect into the measured tritium spectra. For neutrino mass analysis, accurate description of this effect is thereby important. In the following, the retarding potential dependency as an effect of background electrons with finite energies is numerically analyzed for a homogeneous background event distribution inside the main spectrometer and isotropic electron emission directions.

For nonzero electron starting energies, the magnetic moment is nonzero, so the orbital electron motion consumes a part of kinetic energy and if at one point of a field line trajectory, the total kinetic energy is smaller than the transversal kinetic energy needed to keep the magnetic moment, the electron is reflected. Therefore, for these electrons, a high magnetic field e.g.

in the pinch magnet or even the rise of the magnetic field around the analyzing plane might cause rejection of background electrons. Further, background electrons with nonzero starting energies might overcome the potential barrier in the analyzing plane depending on their longitudinal energies.

To analyze these effects, a numerical model is used: For 200 x 200 segments in the $z - r$ plane from $z = -12.1$ m towards the detector, the field lines crossing the center of these segments towards upstream and downstream end of the simulated range are traced. Along these field lines, for a given starting energy, the highest starting angle of electrons transmitted at each 10 cm step on these field lines is calculated. The minima of these starting angles into upstream and downstream direction are then used to calculate the amount of electrons being reflected towards and passing towards the detector for each segment, assuming homogeneous initial background electron densities with 1 count/m^3. The time period during which these electrons is emitted is not further specified. The resulting density maps are then convoluted with fluxtube masks generated for each setting and detector ring, with rings weighted according to their fraction of included detector pixels. A background electron density of 1 count/m^3 was chosen since for simulations assuming electrons with vanishing starting energy, the amount of expected counts on the FPD in [counts] is equal to the corresponding downstream volume in [m^3].

The resulting downstream volume dependency including these effects for electrons with energies between 0.01 eV to 5 eV is shown in Fig. 8.9. Since the downstream volume is calculated using segmented maps, this plot shows very minor variations from the plot for the non-energetic homogeneous downstream volume dependency shown in Section 8.1.1. The mask segmentation was tested by comparing it to results from double the amount of segments in r and z direction and finding that no relevant differences between both maps occur.

The effect of retarding potential dependency is further analyzed in the following for “KNM2 SAP a” and the “KNM2 nominal” setting.

For reference, in Fig. 8.10, the fraction of background electrons reaching the detector from initial isotropic emission at on-axis positions z is plotted to visualize the energy dependency of the background filtering in both settings.

An implication of this is that the potential of the spectrometer vessel, that so far was always arbitrarily set to -18410 V in simulations, does affect the filtering at the pinch magnet and a background slope (the retarding potential dependent background rate) arises for nonzero electron starting energies. This can be seen in Fig. 8.11, where a homogeneous, isotropic emission of events assuming a density of 1 count/m^3 is used to calculate the total amount of counts at the FPD identically as for Fig. 8.9.

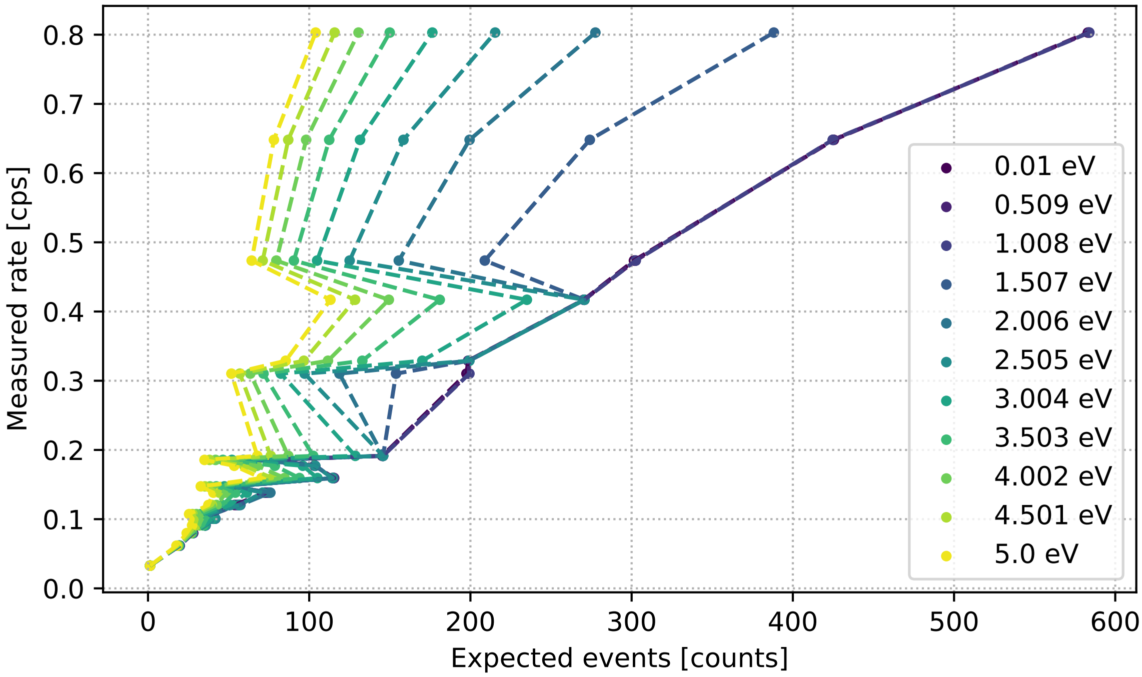

Figure 8.9: Measured rate against expected counts from simulation with electrons starting with nonzero initial energies from an isotropic, homogeneous distribution with density of 1 count/m^3, emitted over a not further specified time period. Color indicates initial energy.

Using this simulation, the vessel potential dependent background slope in this model can be calculated, as shown in Fig. 8.12. It can be seen that the background slope is vanishing for slow electrons. For low vessel potentials, the vessel potential introduced slope for low electron energies is more intense than for high vessel potentials.

Auxiliary figures on this topic can be found in Appendix E.

The described approach is the first estimate of a background slope. It might be possible to limit the amount of low-energetic electrons by measuring the vessel potential dependent background slope, although for this, the spatial distribution of background events inside the spectrometer had to be known more precisely, since the assumption of a homogeneous background distribution seems to be invalidated by Fig. 8.9, where some patterns in downstream volume dependency remain for all given initial electron energies. Trapped electrons, neglected in this simulation, might eventually escape towards source or detector. Since they are constantly introduced into the spectrometer, they might pose a further background component.

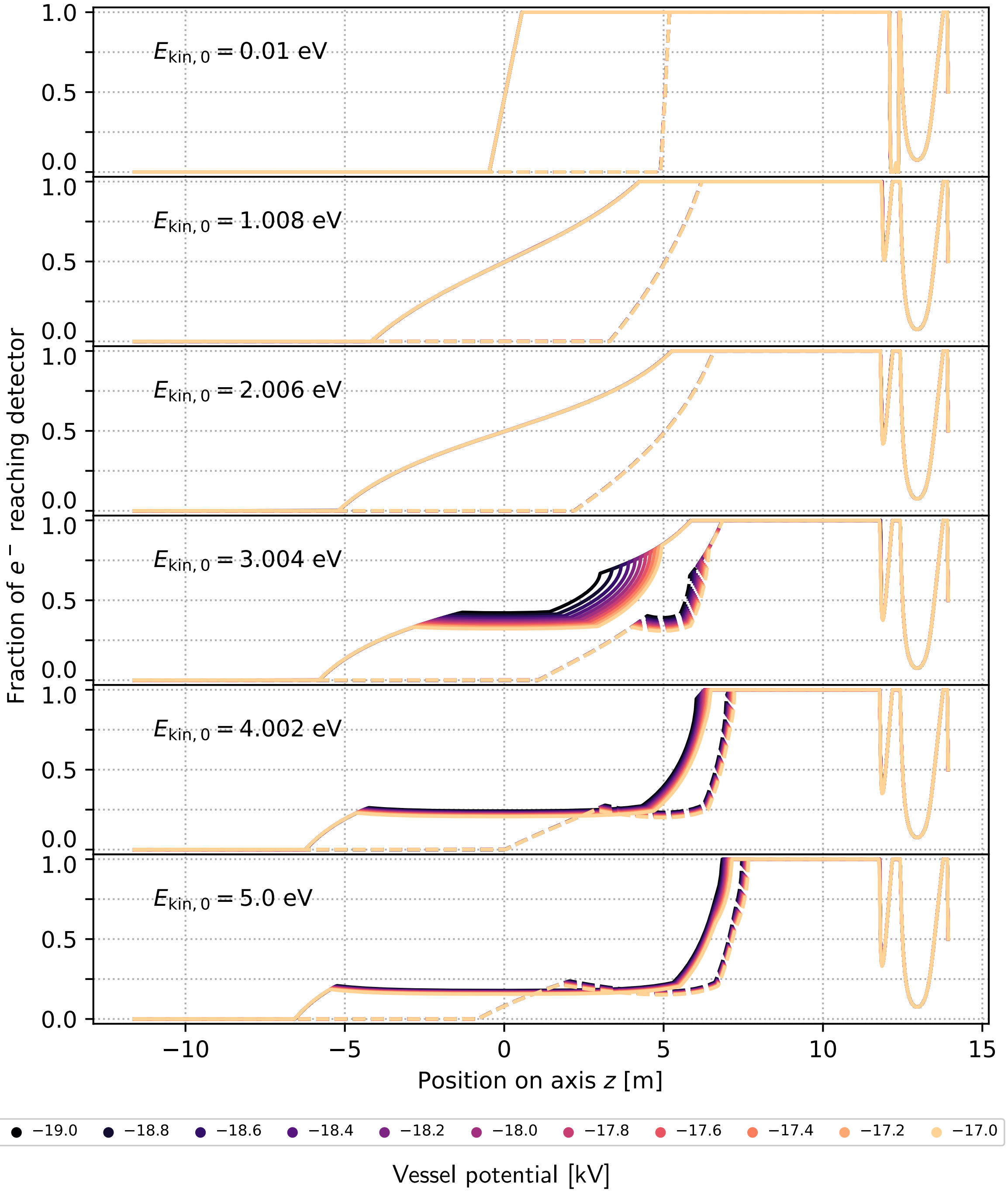

Figure 8.10: Fraction of electrons reaching the FPD from initial on-axis position z in settings "KNM2 SAP a" (dashed line) and "KNM2 nominal" (continuous line). The fraction is calculated for isotropic emission from 1000 equidistant points along z.

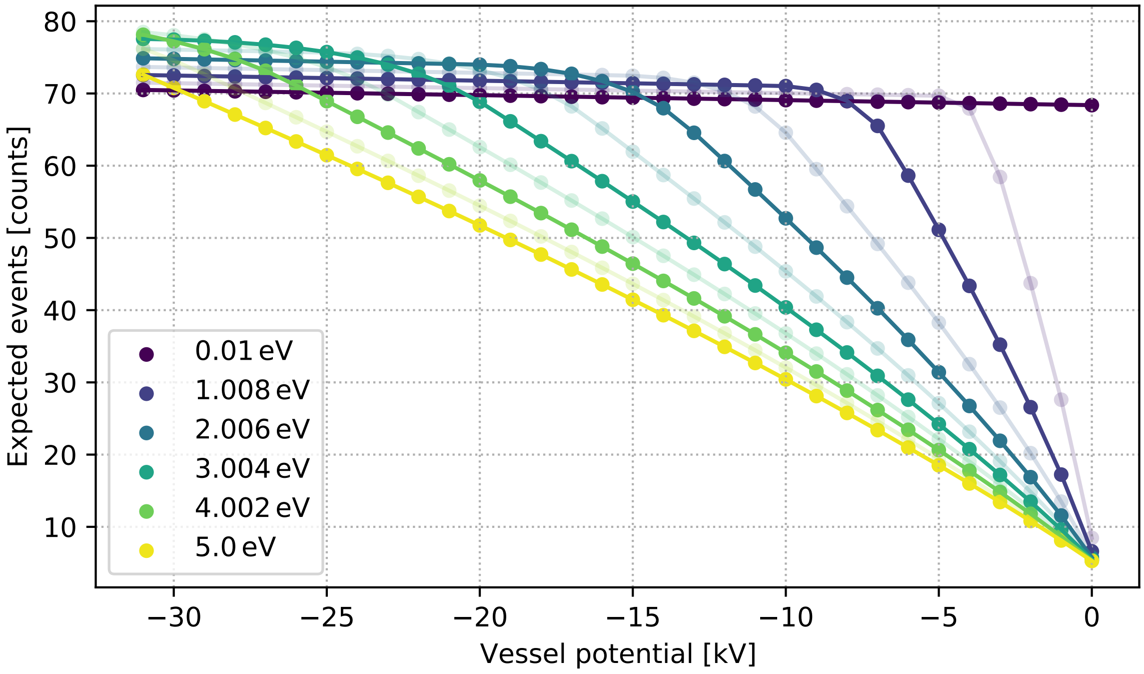

(a) Setting "KNM2 SAP a"

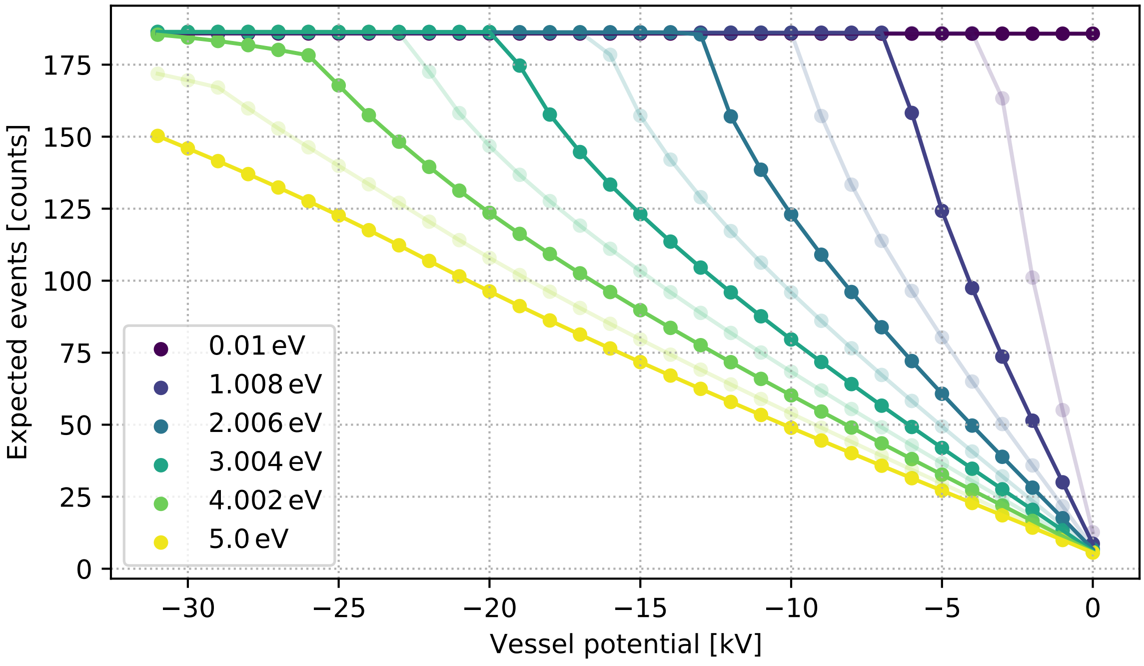

(b) Setting "KNM2 nominal"

Figure 8.11: Expected background counts from simulation for 11 initial electron energies between 0.01 eV and 5 eV from an isotropic, homogeneous distribution with density of 1 count/m^3, emitted over a not further specified time period. 5 of the lines are translucent for visibility.

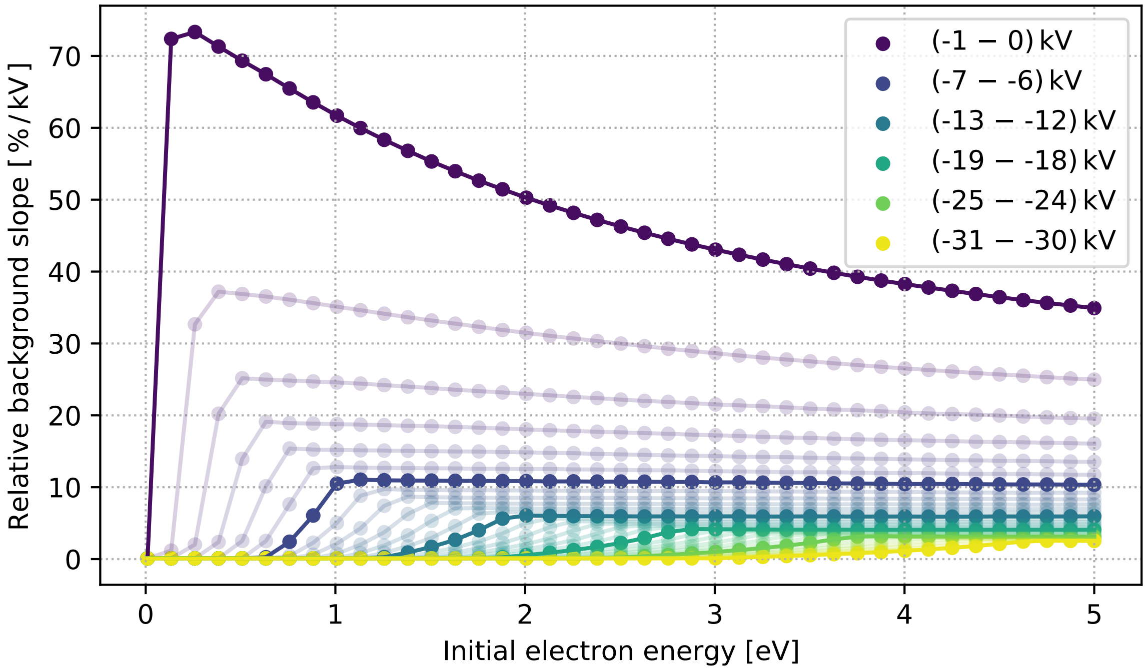

(a) Setting “KNM2 SAP a”

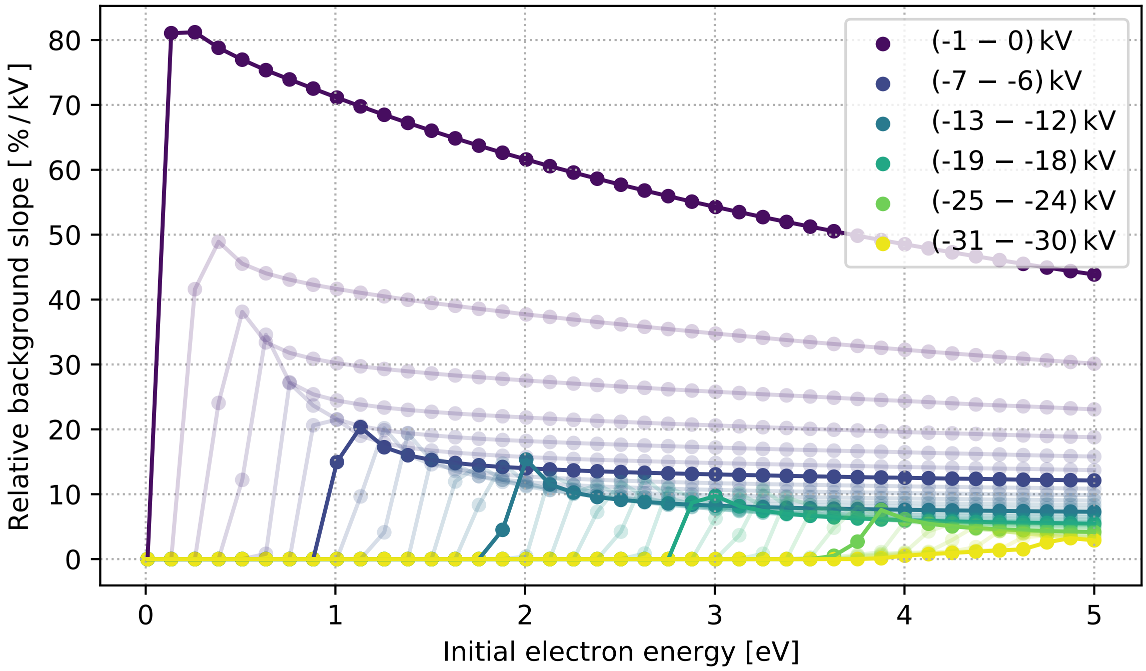

(b) Setting “KNM2 nominal”

Figure 8.12: Expected background slopes from simulation for two spectrometer settings. Relative change $(c(U_i) - c(U_i + 1\,\text{kV}))/c(U_i)/(1\,\text{kV})$ of detector counts $c(U_i)$ for 31 vessel potentials U_i ranging from -31 kV to -1 kV are plotted. 6 vessel potential steps are plotted opaque, with 5 steps plotted translucently in between.

9 Conclusion and outlook

In this thesis, the *shifted analyzing plane* (SAP) approach for background reduction in the KATRIN experiment was studied, tested with measurement data, and its properties with respect to background reduction were investigated. This includes the derivation and optimization of diverse electromagnetic field configurations for the KATRIN main spectrometer and a detailed testing of various physics-motivated and data-driven background models and parametrizations.

It was shown that the KATRIN experiment, as currently leading experiment for the absolute measurement of neutrino masses, has two important background sources: Radon background introduces high-energetic electrons into the spectrometer that are trapped and cause the emission of further, low-energetic background electrons. Rydberg background directly introduces low-energetic background electrons. Both backgrounds can be reduced with the SAP method, as its higher longitudinal magnetic field inhomogeneity reduces electron trapping through the introduction of non-adiabatic trapping losses and low-energetic electrons are only collected in the so-called downstream volume, the reduction of which is the main feature of the SAP method.

For this method, electromagnetic field settings for the KATRIN main spectrometer were generated. Special simulation and visualization software was written and the performance of given software was radically enhanced. A new software based on zonal harmonics field expansion algorithms by Ferenc Glück, `zonalfields2d`, was written and allows the implementation of further simulation-centered scripts and software with ease. The use of zonal harmonic field expansion enables real-time electromagnetic field setting optimization and analysis. The ability to quickly gain intuition for setting optimization while generating new settings “on the fly” became especially useful in the design of spectrometer settings, leading to a new approach in the optimization of SAP spectrometer settings.

Such settings were implemented and measured for two SAP measurement campaigns. During these campaigns, it was possible to introduce knowledge gained from SAP setting optimization into the decision on design criteria and measurement concepts for spectrometer settings. The software developed for this thesis enables the immediate implementation of new settings, allowing to interactively react to findings during SAP measurements. With the reduction of the spectrometer background of at least a factor of two for SAP settings in both measurement campaigns, the KATRIN collaboration decided to use the SAP method in tritium β^- electron spectrum measurements.

For significant parts of the recent tritium spectrum measurement campaign KNM3 and as exclusive configuration for the current tritium spectrum measurement campaign KNM4, further SAP settings were designed over the course of this thesis that are currently in use.

Further, diverse data sets, majorly collected in the context of SAP, were investigated with the self-written software `kamura`, providing quick and interactive analysis of measured electron energies and rate distribution over detector pixels. An overview over the entire detector background spectrum was given for SAP and traditional settings. Similarities were drawn between a currently undescribed effect and a background peak measured in Mainz, assigned to Auger electrons. Further analysis was performed for the ion peak, which was shown to primarily occur at special pixels, and the detector noise floor, of which the observation of its temperature dependency pointed to the instability of the detector temperature.

Models for the background event rates of an SAP measurement campaign were extended and established by using the downstream volume of a spectrometer setting as as fiducial volume for measured low-energetic background electrons. Both data-driven simulations with segmentation of spectrometers and the spectrometer background decay distribution using a physics-motivated background model both led to a reduced $\chi^2 < 4$.

Additionally, theoretical assumptions and simulations with a homogeneous and isotropic background emission model were shown to yield a retarding voltage dependency of spectrometer background for non-zero initial background electron energies, shown for settings representative for both the most common SAP settings and unshifted, “nominal” settings recently used for tritium spectrum measurement.

Further research to improve the given models could include the different Radon trapping properties of MAC-E filter settings in simulations. The retarding potential dependency could also be exploited to gain information on background electron energy spectra and thereby about the background composition. For this, the influence of non-homogeneous distribution of background events inside the main spectrometer on this dependency has to be analyzed. Both the improved models and the measured downstream volume dependency allow for automated optimization of SAP settings for optimal sensitivity on the electron antineutrino mass. Additionally, investigating the retarding potential dependency of given background promises further information on the currently unknown systematic “background slope”, allowing for better precision in neutrino mass analysis of KATRIN data.

A Angular distribution at detector

This chapter describes the analysis for Fig. 4.2. Rydberg background and tritium signal electrons are assumed to be emitted homogeneously, meaning every point on a unit sphere represents an equally likely emission direction. For a given angle of emission against the z-axis (the axis of symmetry) θ_S, this results in the following probability density function for emission into direction θ_S:

$$p_S(\theta_S) = 2\pi \sin(\theta_S)/A_{\text{unit sphere}} = 1/2 \sin(\theta_S)$$

Here, the PDF is described as the circumference of a circle described by points on a unit sphere in direction of θ_S as fraction of the total area of the unit sphere.

To calculate the probability of electrons at the detector, we resolve the transmission condition Eq. (2.8) for $\sin^2(\theta)$ ($_z$ is used to indicate properties of the electron path at position z):

$$\sin^2(\theta_S) < (1 + e \cdot (U_z - U_S)/E_{\text{kin,initial}}) \frac{B_S}{B_z} \frac{\gamma_z + 1}{\gamma_S + 1} := a$$

This leads to electrons passing position a maximal angle θ_S of

$$\hat{\theta_S} = \begin{cases} 90\,^\circ & a \geq 1 \\ \arcsin(\sqrt{a}) & a < 1 \end{cases} .$$

With this, the filtering of electrons at the pinch magnet can be calculated, constraining angles θ_S of electrons reaching the detector to the range of $0\,^\circ$ to $\hat{\theta_S}$. In this calculation, signal and background electrons are assumed not to be retarded by the MAC-E filter, which is true for very low-energetic background electrons (see Chapter 8) and signal electrons with energies significantly above the retarding potential.

Use of the chain rule on integrals of p_S and the angular PDF p_z at z with the use of the fact that $P_S(\theta_S \leq x) = P_z(\theta_z(\theta_S) \leq x)$ lead to:

$$p_z(\theta_z) = p_S(\theta_S(\theta_z)) \frac{d\theta_S}{d\theta_z} .$$

Table A.1: Magnetic field strengths and electric potentials used in this chapter

Component	**Mag. field strength** [T]	**El. potential** [kV]
WGTS	2.52 [Ake+19]	0
AP	$6.3 \cdot 10^{-4}$ [Ake+19]	-18.6
PCH	4.24 [Ake+19]	0
DET	2.37 [Own simulation]	0

With the adiabatic invariant Eq. (2.7) and Eq. (2.3), the relation

$$\theta_z = \arcsin\left(\sqrt{\sin^2(\theta_z) B_S / B_z \cdot p_z^2 / p_S^2}\right)$$

arises. With the identification of the relativistic energy-momentum relation Eq. (2.5), and a as defined above, this lends

$$\theta_S = \arcsin\left(\sqrt{\sin^2(\theta_z) \cdot a}\right)$$

and therefore

$$\frac{d\theta_S}{d\theta_z} = \frac{a\cos(\theta_z)\sin(\theta_z)}{\sqrt{a\sin^2(\theta_z)} \cdot \sqrt{1 - a\sin^2(\theta_z)}} \, .$$

With the range for θ_S given from the calculation above and the assumed magnetic field strengths and electric potentials from Table A.1, this now allows the calculation of the PDF of background and signal electron angles at the detector for electrons starting at WGTS or AP.

B Overview over further spectra

In this section, further datasets are presented that were analyzed over the course of this thesis but not necessarily presented in its the main part. These datasets were mostly not measured for this thesis and are currently part of unpublished analysis. For each dataset, plots and a short description of their context are given in Fig. B.1 to B.9. No selection for significance of effects like the ion peak was performed.

The KNM2 $m_{\overline{\nu}_e}$ dataset used for investigations in Section 7.4 uses a total measurement time of 555085 s. Since the following datasets all feature less measurement time, the following FPD plots show total counts per pixel with information on measurement time to enable estimation of uncertainty on all plots. Bin widths of histograms with low counts are increased for readability. Histograms include event rates of all working pixels in blue and of combined KNM1 and KNM2 golden pixel selections in orange.

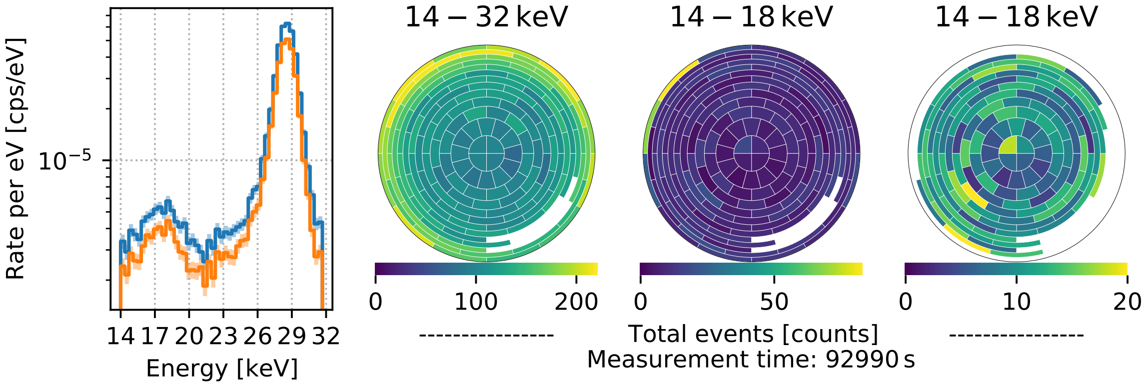

Figure B.1: All background measurements during KNM1 SAP measurements combined, including background measurements during tritium β^- decay scans. Measurement took place from 13th to 17th May 2019. Histogram bin width: approx. 0.36 keV. Corresponding ELOG: `https://ikp-neu-katrin.ikp.kit.edu/elog/KNM1/184`

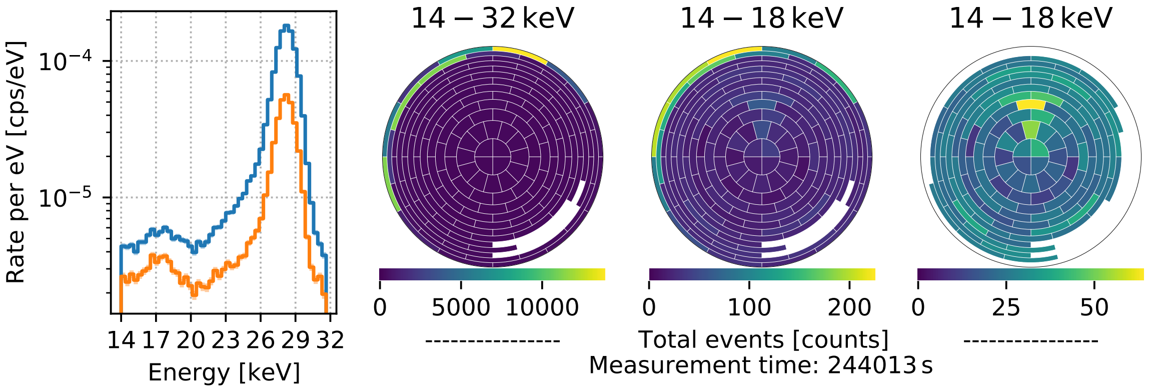

Figure B.2: All background measurements during KNM2 SAP measurements combined. Measurement took place from 11th to 15th September 2019. Histogram bin width: approx. 0.36 keV. Corresponding ELOGs: `https://ikp-neu-katrin.ikp.kit.edu/elog/KNM2/22`, `https://ikp-neu-katrin.ikp.kit.edu/elog/KNM2/25`

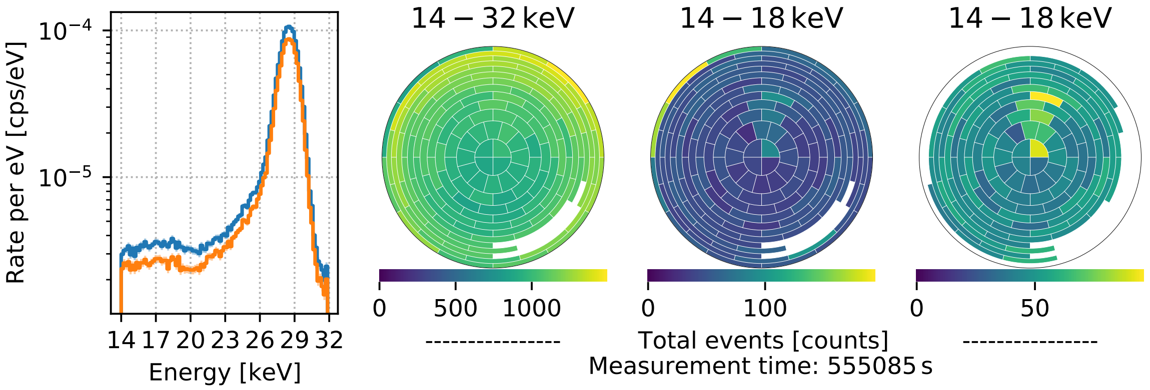

Figure B.3: All background measurements during KNM2 $m_{\overline{\nu}_e}$ measurements combined. Measurement took place from 2nd October to 14th November 2019. Histogram bin width: approx. 0.18 keV.

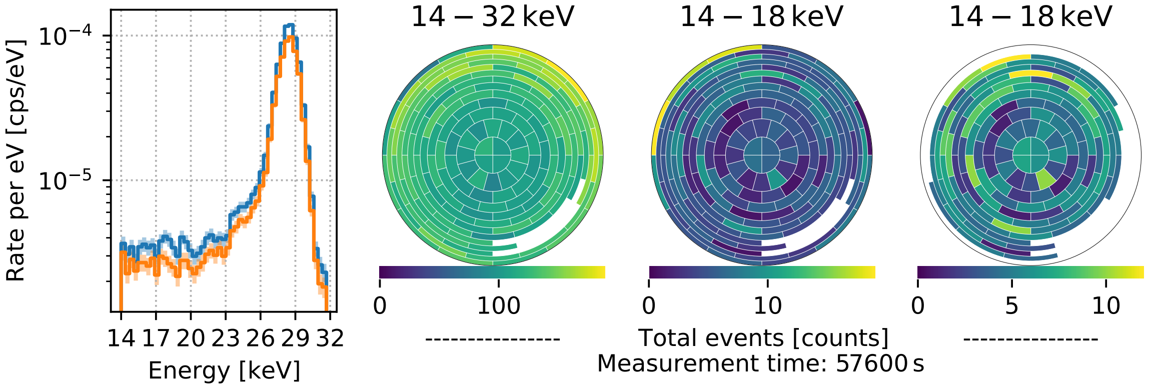

Figure B.4: Background measurements with elevated argon pressure. Measurement took place on 19th November 2019. Histogram bin width: approx. 0.36 keV. Corresponding ELOG: `https://ikp-neu-katrin.ikp.kit.edu/elog/knm2/119`

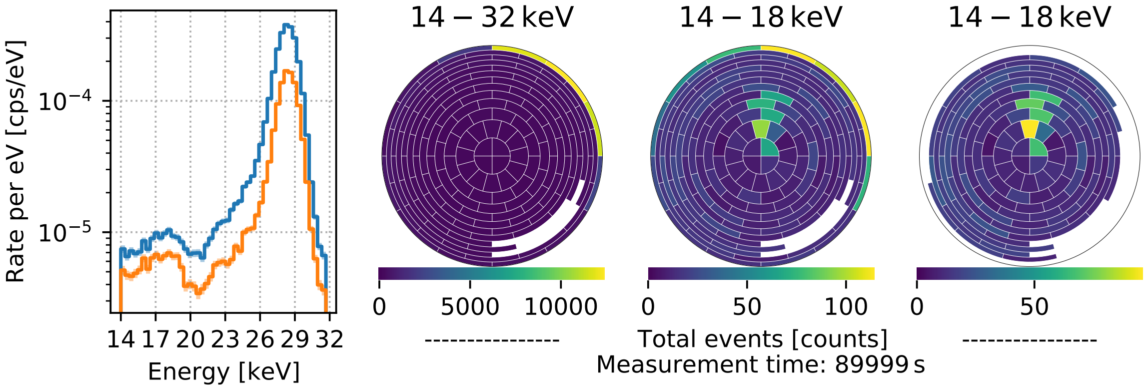

Figure B.5: “Longitudinal scan” background measurements. Measurement took place on 10th and 11th January 2020. Histogram bin width: approx. 0.36 keV. Corresponding ELOG: `https://ikp-neu-katrin.ikp.kit.edu/elog/KNM2/172`

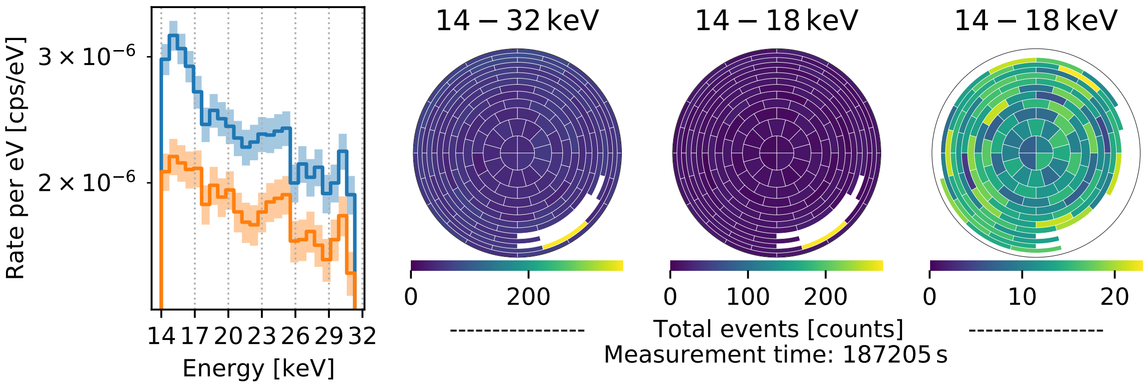

Figure B.6: Measurement of detector background. Measurement took place on 9th March 2020. Histogram bin width: approx. 0.72 keV. Corresponding ELOG: `https://ikp-neu-katrin.ikp.kit.edu/elog/KNM2/173`

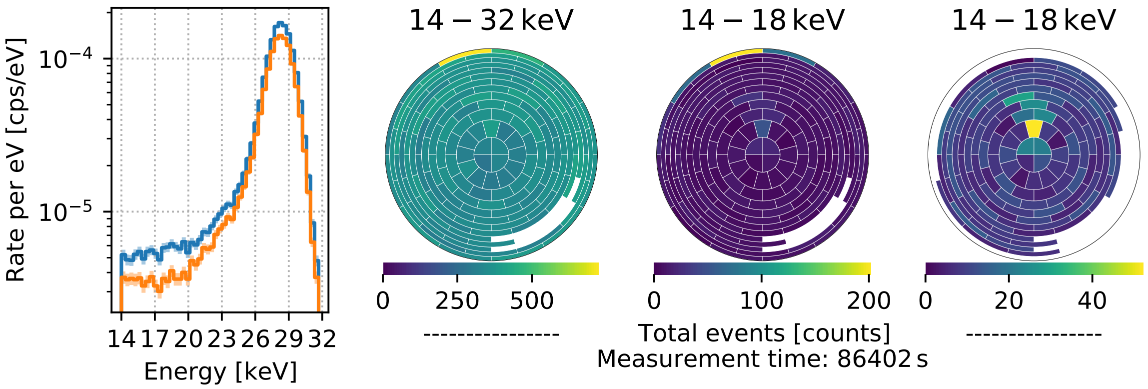

Figure B.7: Background measurements with warm baffles and setting “KNM2 nominal”. Measurement took place on 26th March 2020. Histogram bin width: approx. 0.36 keV. Corresponding ELOG: `https://ikp-neu-katrin.ikp.kit.edu/elog/KNM3/7`

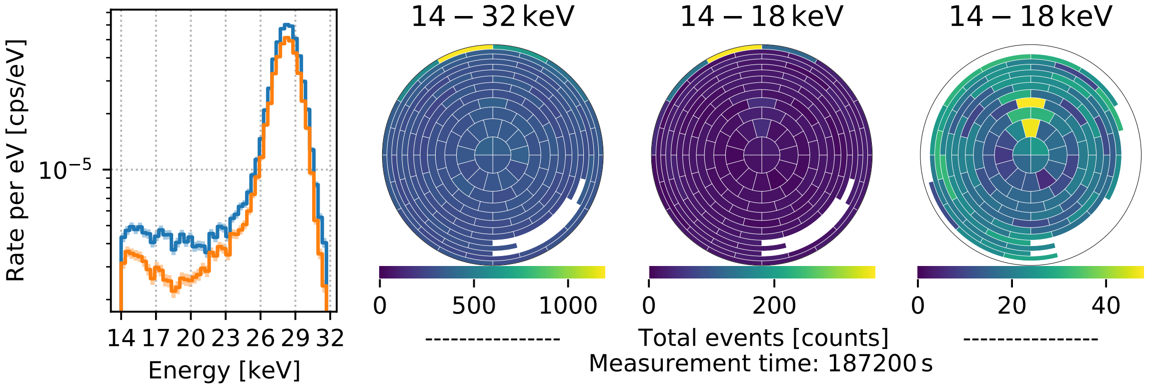

Figure B.8: Background measurements with warm baffles and SAP setting. Measurement took place on 26th March 2020. Histogram bin width: approx. 0.36 keV. Corresponding ELOG: `https://ikp-neu-katrin.ikp.kit.edu/elog/KNM3/7`

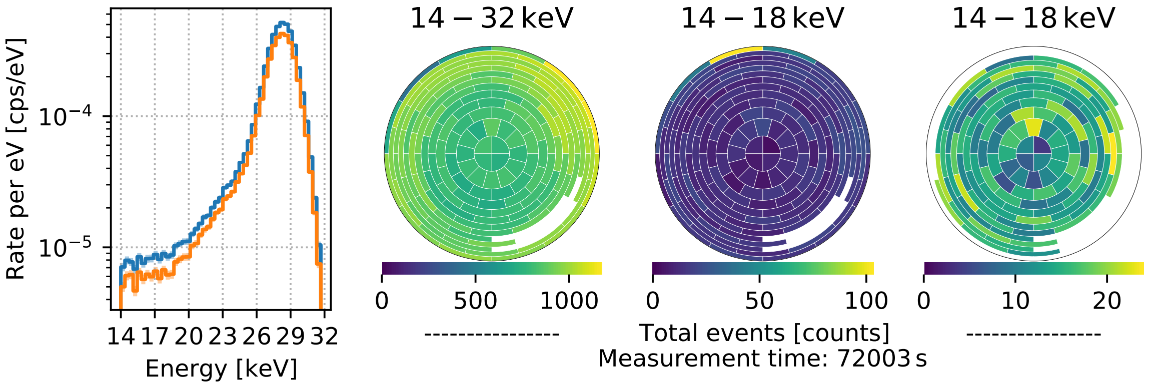

Figure B.9: Background measurements with warm baffles and elevated argon pressure. Measurement took place on 30th March 2020. Histogram bin width: approx. 0.36 keV. Corresponding ELOG: `https://ikp-neu-katrin.ikp.kit.edu/elog/KNM3/8`

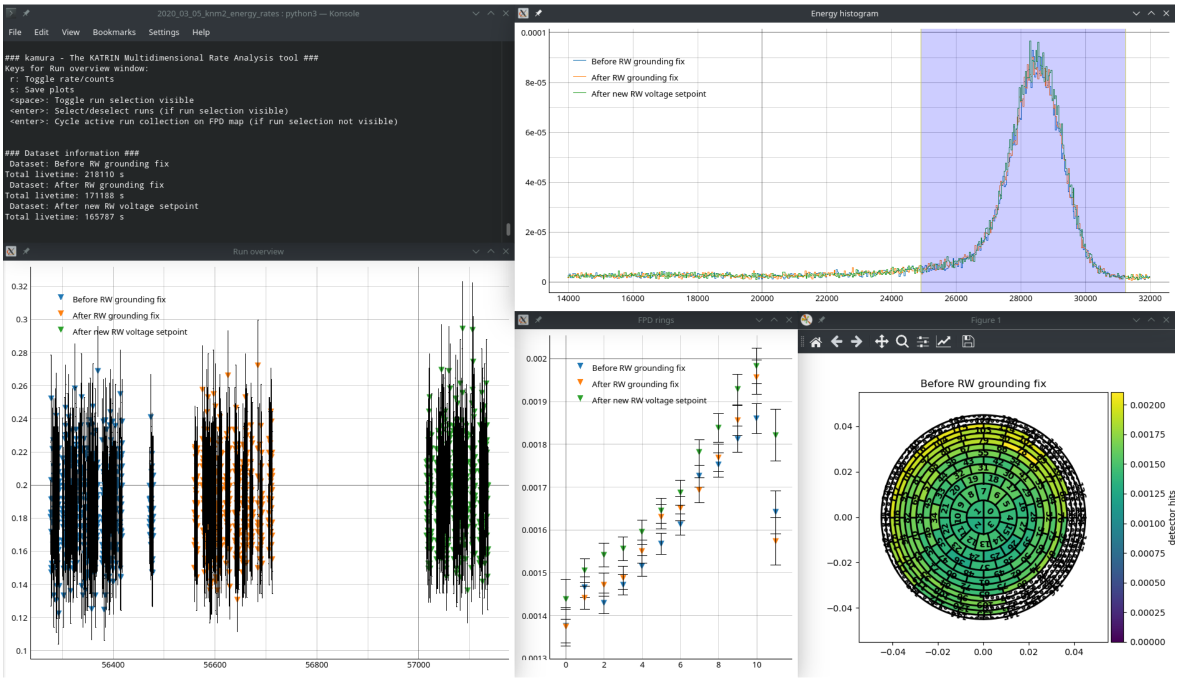

```
### kamura - The KATRIN Multidimensional Rate Analysis tool ###
Keys for Run overview window:
 r: Toggle rate/counts
 s: Save plots
 <space>: Toggle run selection visible
 <enter>: Select/deselect runs (if run selection visible)
 <enter>: Cycle active run collection on FPD map (if run selection not visible)


### Dataset information ###
 Dataset: Before RW grounding fix
Total livetime: 218110 s
 Dataset: After RW grounding fix
Total livetime: 171188 s
 Dataset: After new RW voltage setpoint
Total livetime: 165787 s
```

Figure B.10: Screenshot of multi-window application `kamura`. “Run overview”, “Energy Histogram” and the FPD plot are interactive, allowing quick data cuts.

For initial investigations on these datasets, the GUI application `kamura` was developed, a screenshot of which can be found in Fig. B.10.

C Downstream dependency for full rings

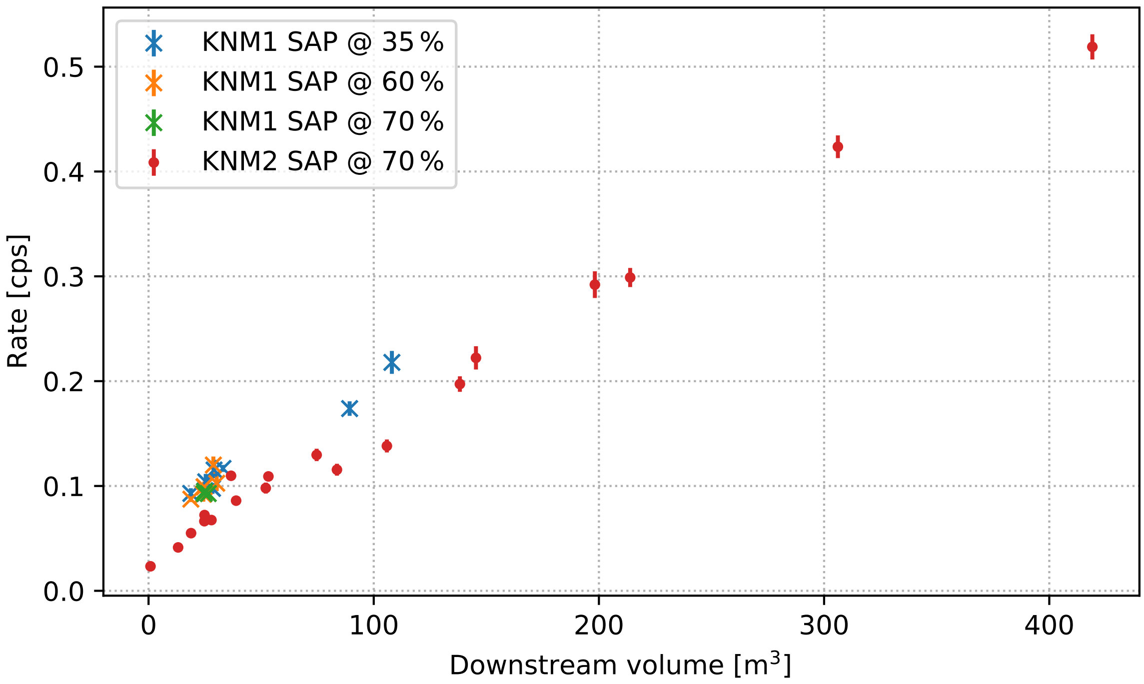

Figure C.1: Measured rates against downstream volume for SAP measurement campaigns during KNM1 and KNM2. Calculated downstream volumes include volume reduction by excluded detector pixels. Calculations are performed axisymmetrically. Only rings without excluded pixels in both KNM1 and KNM2 golden pixel selections.

Figure 8.2 shows measured rate against simulated downstream volume for a 5 mm detector offset. It can be compared against Fig. 8.1, but due to its simulation algorithm, it has a different pixel selection that only contains full rings. For comparison, Fig. C.1 provides a similar calculation as Fig. 8.1 with the same pixel cut as Fig. 8.2.

D Extended fit results

In this chapter, further information is given on fits presented in the main part of this thesis.

D.1 Linear fits

Model a) Three surfaces with equal minimal distance from the walls of 2 m, 3 m and 4 m divide the spectrometer into four volumes.

With the segment IDs from Fig. D.1, the following background rate densities per element yield the setting with the least red. χ^2, the residuals of which can be found in Fig. D.2:

`Segment 0:` `1.54 mcps/m`^{3}, `Segment 1:` `1.32 mcps/m`^{3},
`Segment 2:` `1.09 mcps/m`^{3}, `Segment 3:` `0.81 mcps/m`^{3},
$c_0 \approx$`1.13 mcps/m`^{3}

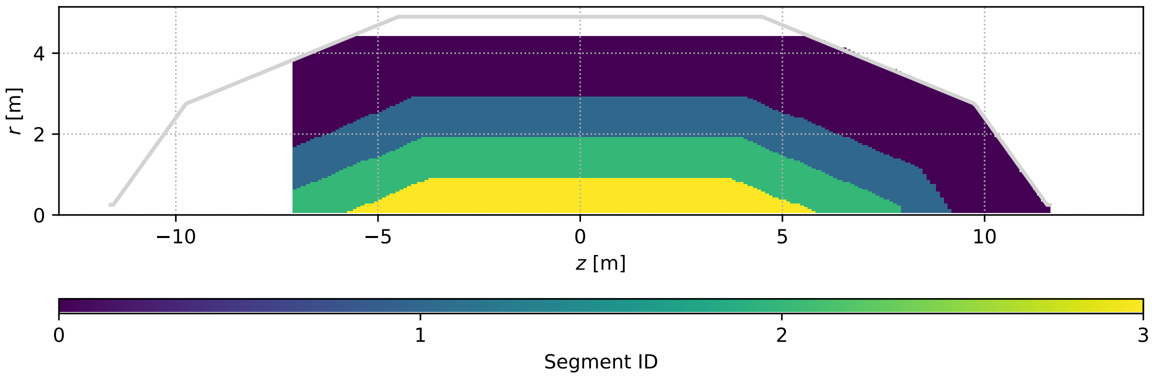

Figure D.1: Segment IDs for model a) from Fig. 8.4

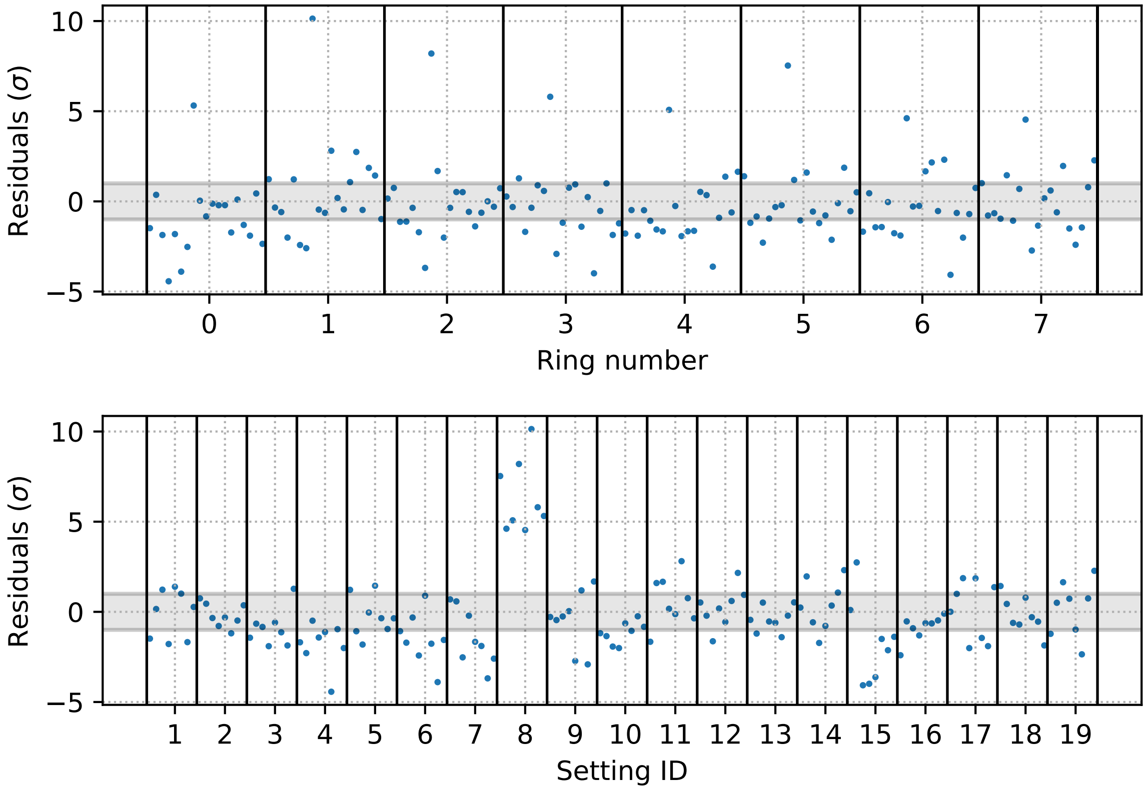

Figure D.2: Standardized residuals for model a) from Fig. 8.4. Residuals are shown clustered by their respective fitted detector pixel ring and their setting.

Model b) Two surfaces with equal z of -1 m and 4 m divide the spectrometer into three volumes.

With the segment IDs from Fig. D.3, the following background rate densities per element yield the setting with the least red. χ^2, the residuals of which can be found in Fig. D.4:

`Segment 0:` $1.31\,\mathrm{mcps/m^3}$, `Segment 1:` $0.86\,\mathrm{mcps/m^3}$,

`Segment 2:` $1.68\,\mathrm{mcps/m^3}$, $c_0 = 0\,\mathrm{mcps/m^3}$

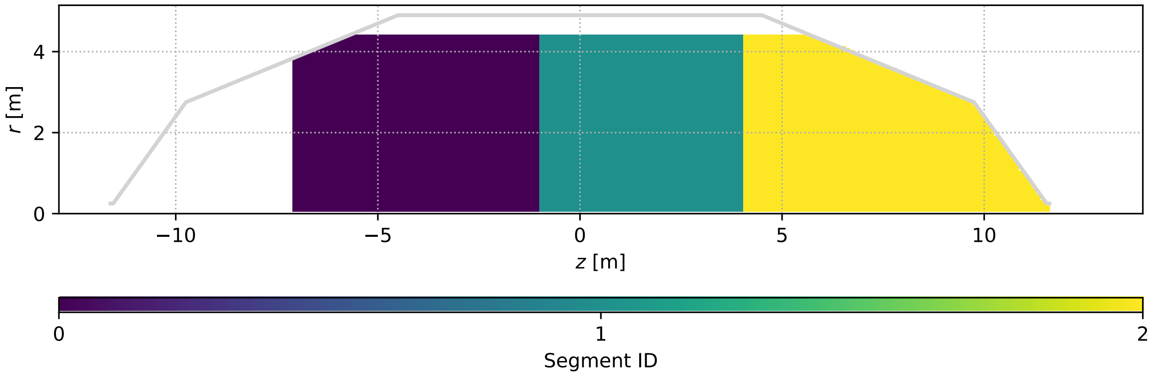

Figure D.3: Segment IDs for model b) from Fig. 8.4

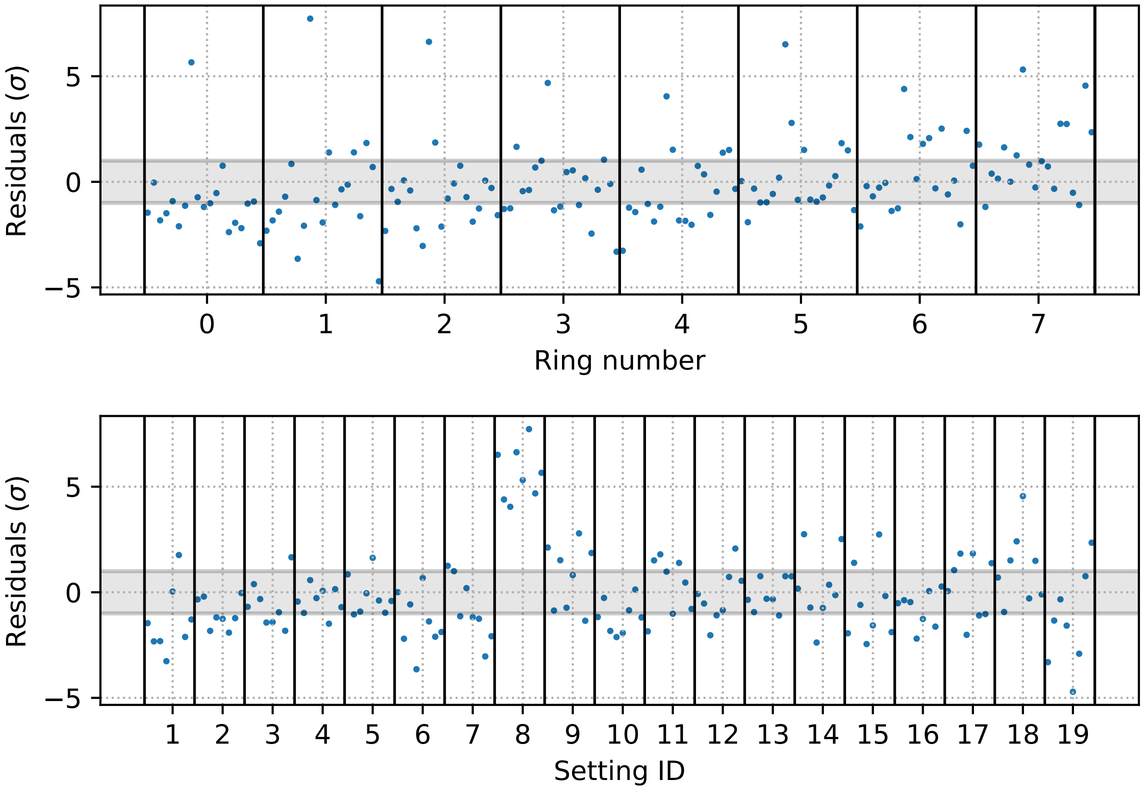

Figure D.4: Standardized residuals for model b) from Fig. 8.4. Residuals are shown clustered by their respective fitted detector pixel ring and their setting.

Model c) Two surfaces with equal z of -1 m and 4 m divide the spectrometer into three volumes.

With the segment IDs from Fig. D.5, the following background rate densities per element yield the setting with the least red. χ^2, the residuals of which can be found in Fig. 8.5:

`Segment 0:` 1.50 mcps/m^3, `Segment 1:` 0.84 mcps/m^3,
`Segment 2:` 1.57 mcps/m^3, `Segment 3:` 1.46 mcps/m^3,
`Segment 4:` 1.11 mcps/m^3, `Segment 5:` 1.15 mcps/m^3,
`Segment 6:` 0.73 mcps/m^3, `Segment 7:` 0.67 mcps/m^3,
`Segment 8:` 1.85 mcps/m^3, `Segment 9:` 1.63 mcps/m^3,
`Segment 10:` 1.57 mcps/m^3, `Segment 11:` 0.29 mcps/m^3,
c_0 = 0 mcps/m^3

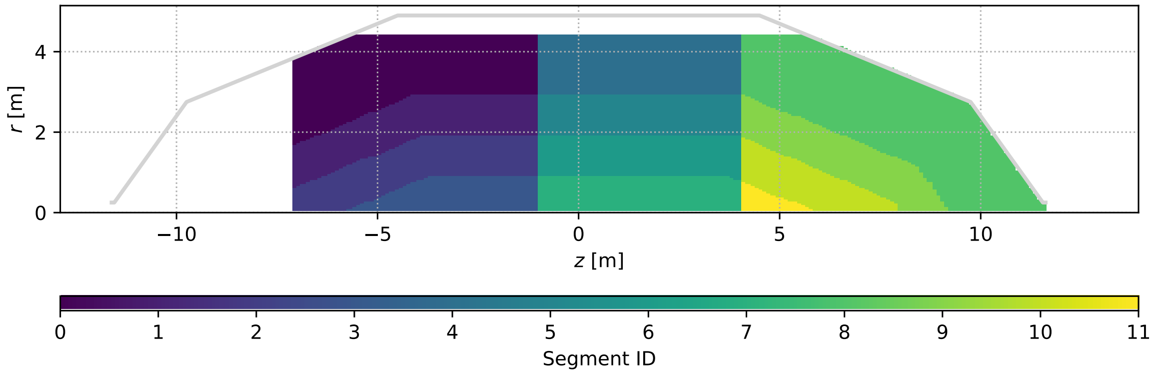

Figure D.5: Segment IDs for model c) from Fig. 8.4

D.2 Exponential fits

Model a) Isotropic emission into vessel volume.

The best reduced χ^2 was found with the following parameter values, yielding the residuals shown in Fig. 8.8:

$a \approx 1.46$, $b \approx 3.27\,\mathrm{m}$.

Model b) Isotropic emission and constant volume dependent background density d.

The best reduced χ^2 was found with the following parameter values, yielding the residuals shown in Fig. D.6:

$a \approx 1.45$, $b \approx 3.27\,\mathrm{m}$, $d \approx 0.014\,\mathrm{mcps}$.

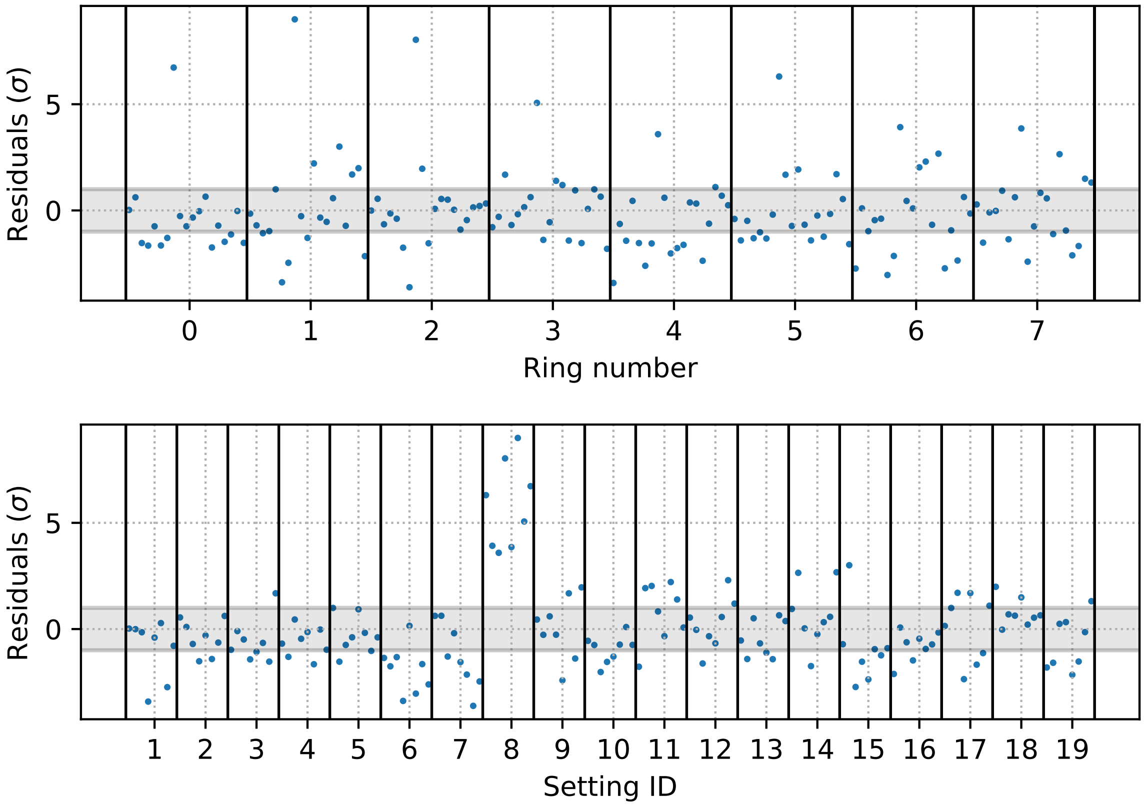

Figure D.6: Standardized residuals for model b) from Fig. 8.6. Residuals are shown clustered by their respective fitted detector pixel ring and their setting.

Model c) Angular distribution assumed for sputtering processes and constant volume dependent background density d.

The best reduced χ^2 was found with the following parameter values, yielding the residuals shown in Fig. D.7:

$a \approx 0.82$, $b \approx 0.72\,\mathrm{m}$, $d \approx 0.83\,\mathrm{mcps}$.

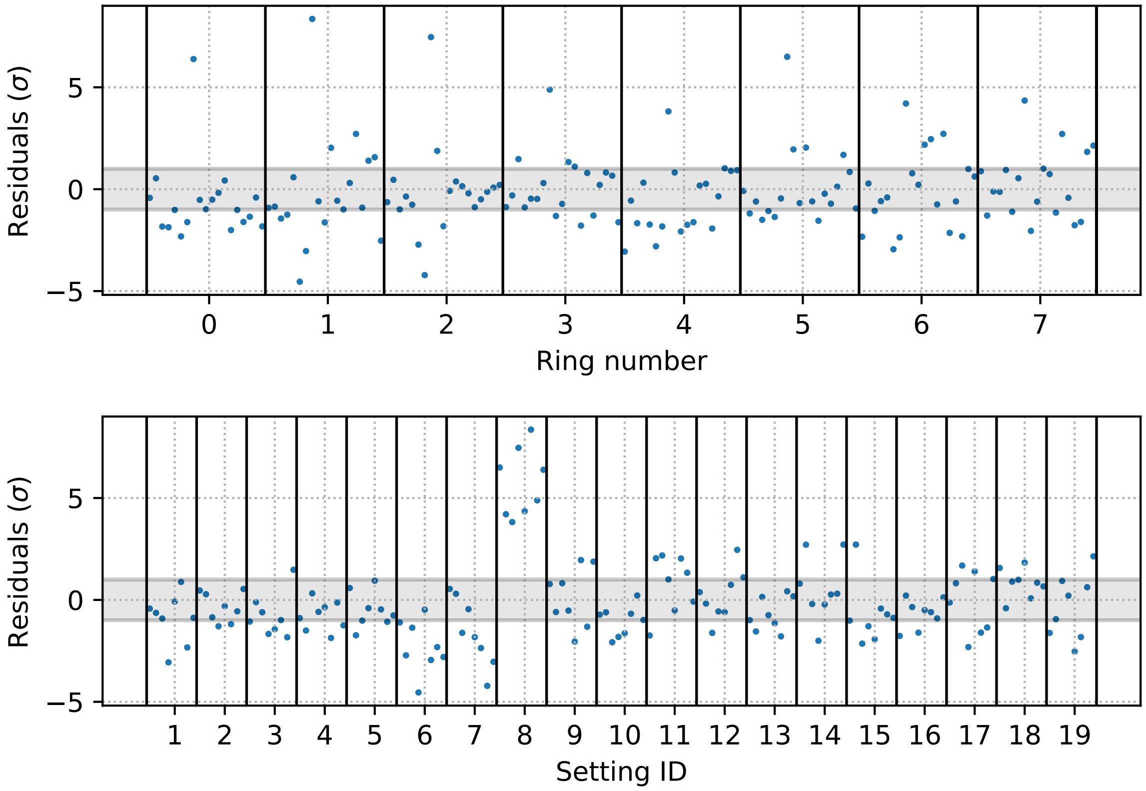

Figure D.7: Standardized residuals for model c) from Fig. 8.6. Residuals are shown clustered by their respective fitted detector pixel ring and their setting.

E Retarding potential dependent background slope

This chapter shows auxiliary figures of the analysis presented in Section 8.2.

The background slope arises from electrons starting in or near the analyzing plane. A part of these electrons are reflected at the pinch magnet. The different magnetic field strengths prevalent in the analyzing plane of settings "KNM2 nominal" and "KNM2 SAP a" are visualized in Fig. E.1. This allows interpretation of Fig. E.2, which shows the maximal transmitted angle of electrons at the pinch magnet in dependence on their initial kinetic energies, retarding potential and magnetic field strength.

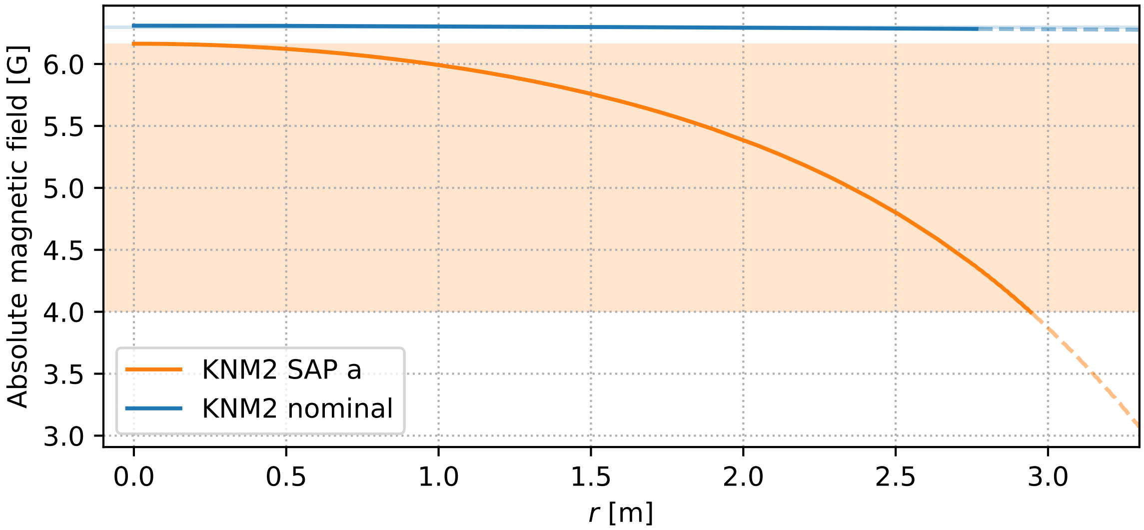

Figure E.1: Radial distributions of magnetic field over the analyzing plane for settings "KNM2 SAP a" und "KNM2 nominal" in axisymmetric simulation. Dotted lines show the fields and potentials outside the fluxtube. Colored areas show the range of potentials and magnetic fields over the analyzing plane.

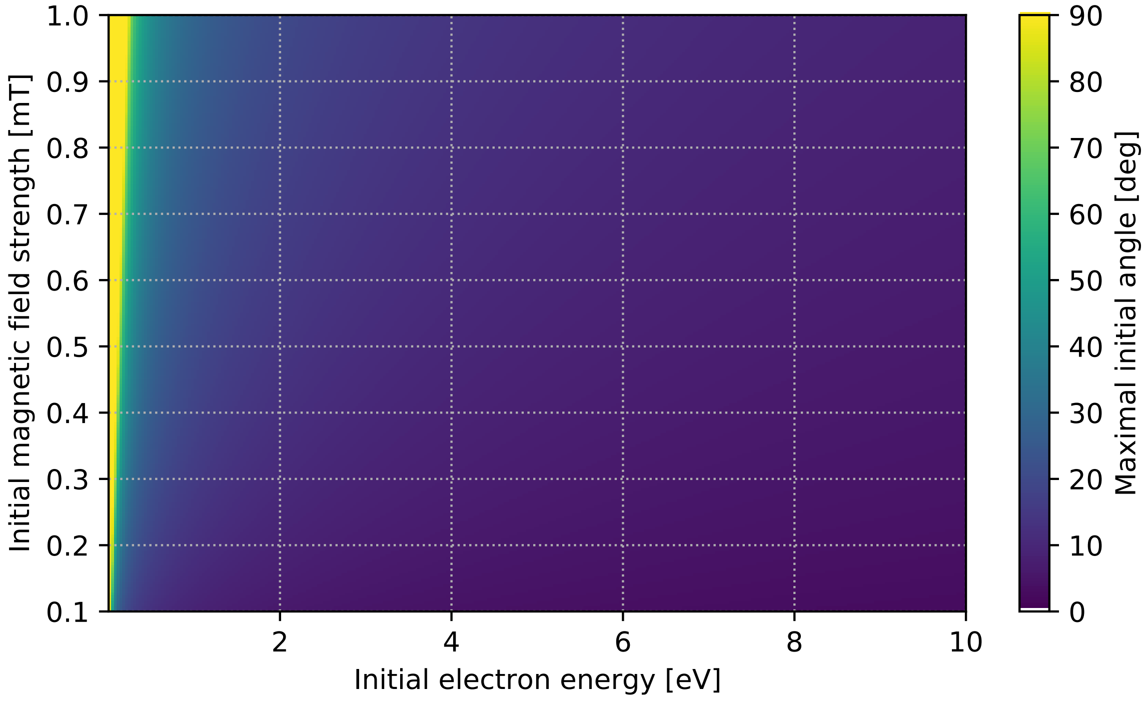

(a) -1 kV retarding potential

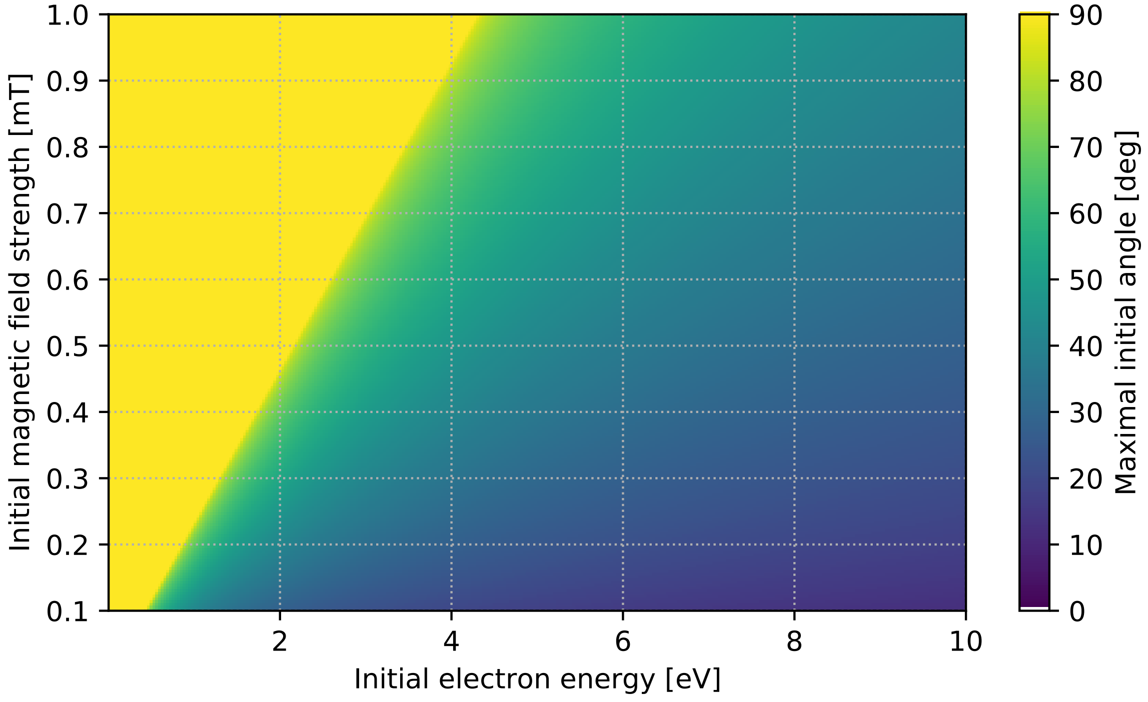

(b) -18 kV retarding potential

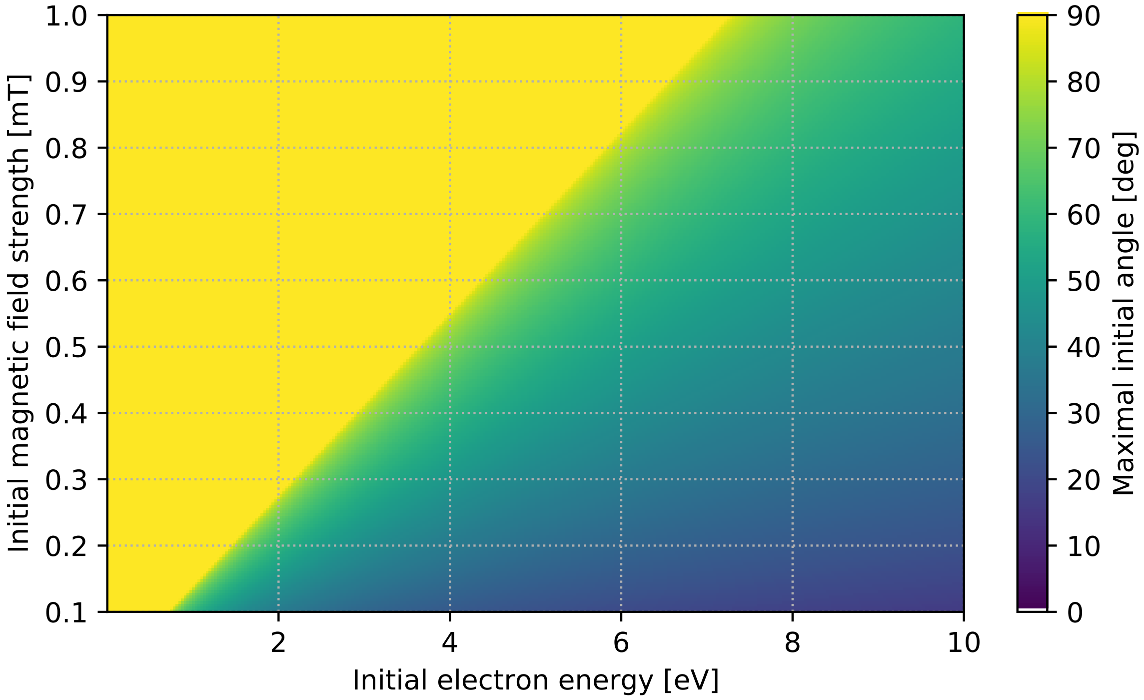

(c) -30 kV retarding potential

Figure E.2: Maximal initial angle transmitted according to the transmission condition. Calculated for 1000 initial electron energies between 0.01 eV and 10 eV and 1000 initial magnetic field strengths from 0.1 mT to 1 mT for three retarding potentials. Assuming retardation at the pinch magnet with 4.24 T [Ake+19].

In the main part of the thesis, Fig. 8.10 showed the fraction of electrons starting isotropically on the axis of symmetry at a point z that reach the detector. Figure E.3 and Fig. E.4 accompany these plots, breaking it into the fraction of electrons emitted towards the source and towards the detector side respectively.

Finally, the retarding potential dependent background slope is plotted in Fig. E.5 for comparison between settings “KNM2 nominal” and “KNM2 SAP a” with vessel potentials of -18 kV and -19 kV.

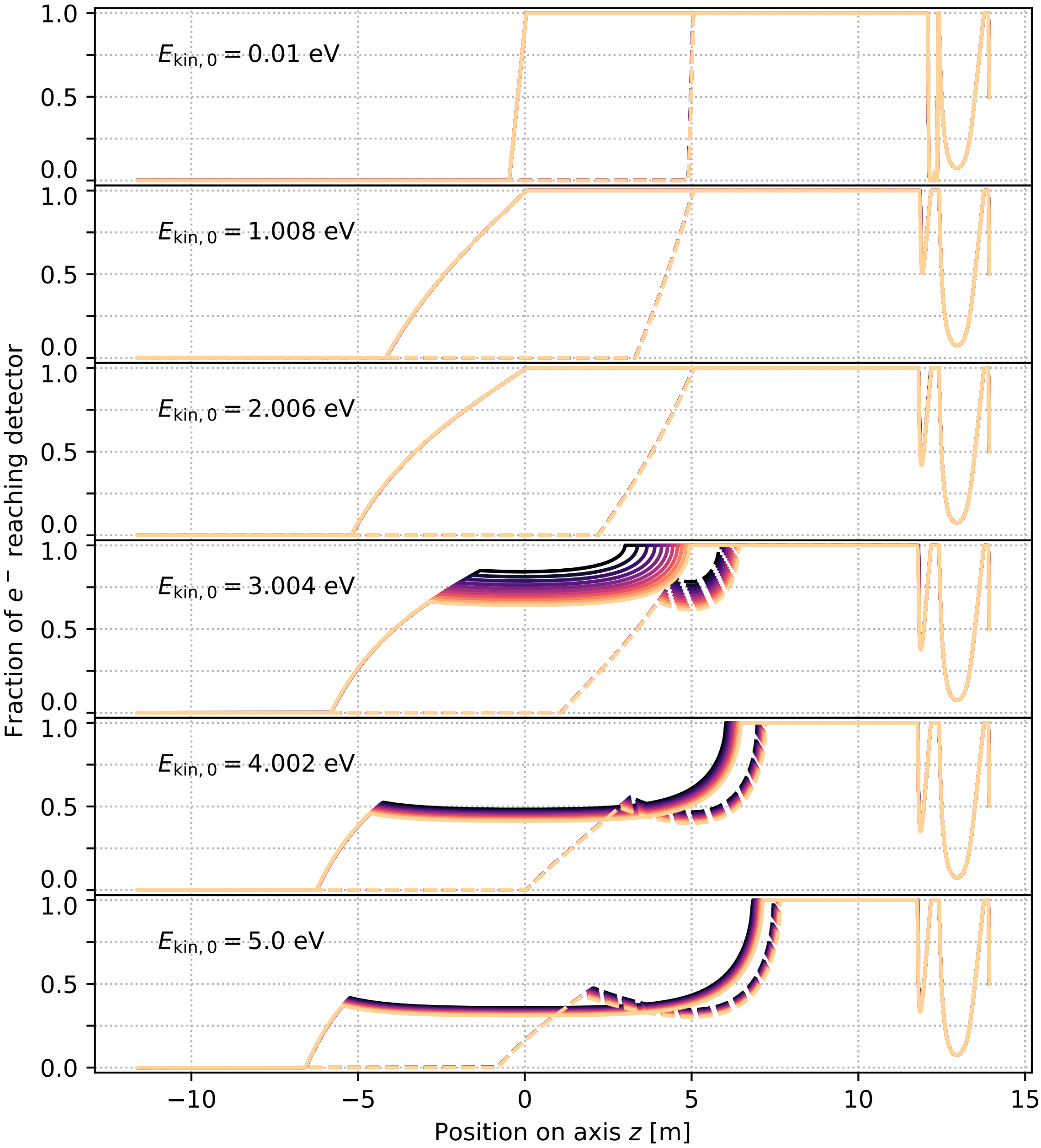

Figure E.3: Fraction of electrons reaching the FPD from emission into downstream direction at initial on-axis position z. Settings "KNM2 SAP a" (dashed line) and "KNM2 nominal" (continuous line) are shown. The fraction is calculated for 1000 equidistant points along z.

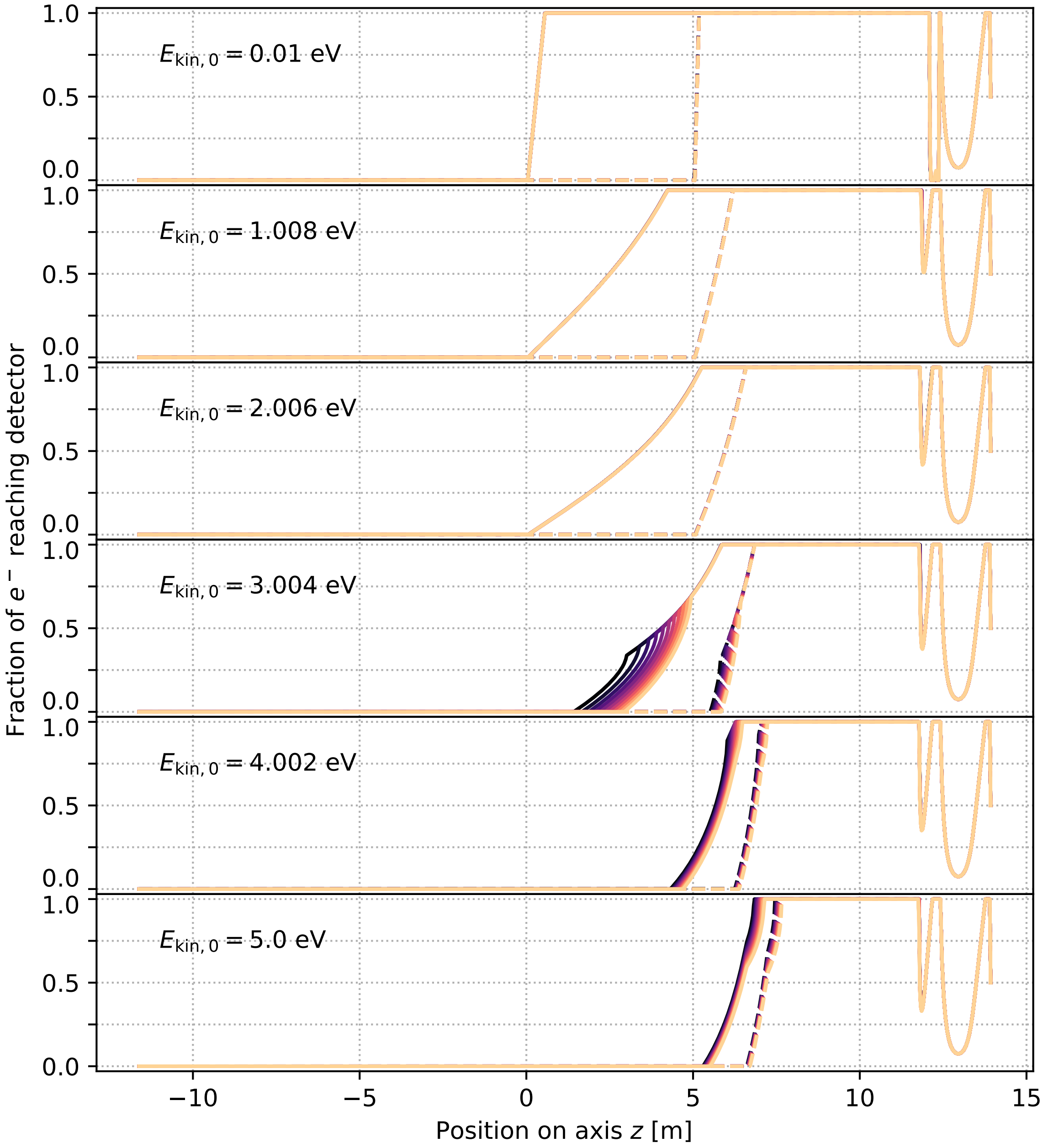

Figure E.4: Fraction of electrons reaching the FPD from emission into upstream direction at initial on-axis position z. Electrons are considered that are reflected on their way to $z = -12.1\,\mathrm{m}$ before the detector entrance. Settings “KNM2 SAP a” (dashed line) and “KNM2 nominal” (continuous line) are shown. The fraction is calculated for 1000 equidistant points along z.

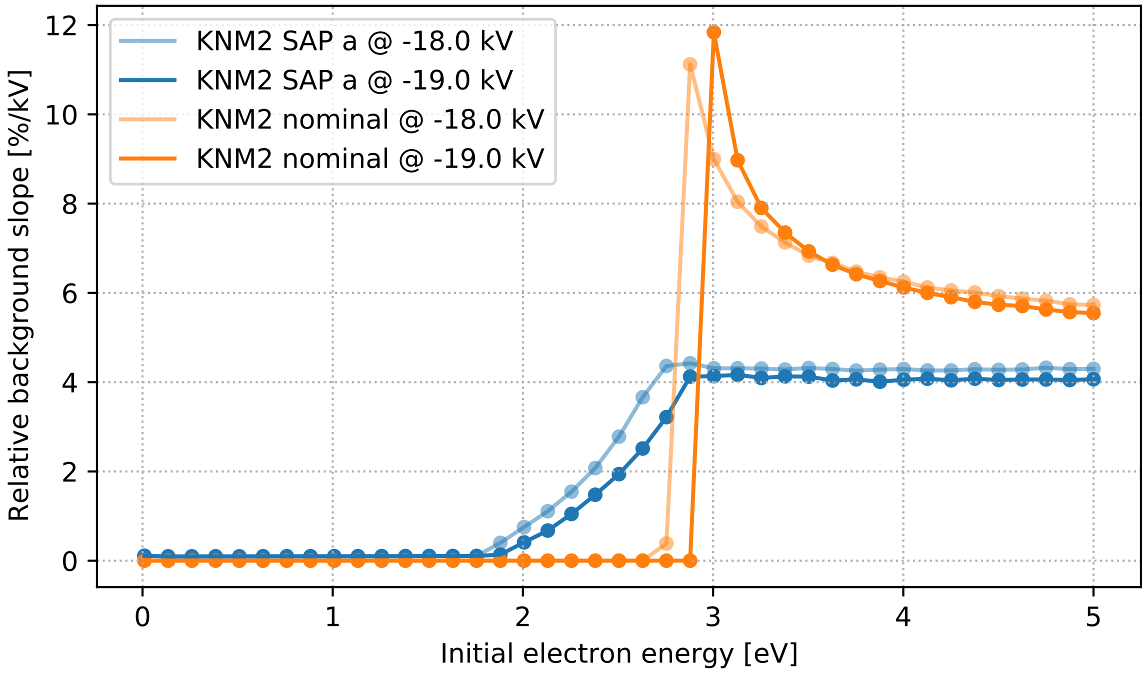

Figure E.5: Expected background slopes from simulation for setting “KNM2 nominal” and “KNM2 SAP a”. Relative change $(c(U_i) - c(U_i + 0.1\,\mathrm{kV}))/c(U_i)/(0.1\,\mathrm{kV})$ of detector counts $c(U_i)$ for two vessel potentials U_i of -18 kV and -19 kV are plotted.

Bibliography

[Aar+20] MG Aartsen et al. “Development of an analysis to probe the neutrino mass ordering with atmospheric neutrinos using three years of IceCube DeepCore data”. In: *The European Physical Journal C* 80.1 (2020), pp. 1–16 (cit. on p. 4).

[Ahm+01] Q. R. Ahmad et al. “Measurement of the Rate of $\nu_e + d \to p + p + e^-$ Interactions Produced by ^8B Solar Neutrinos at the Sudbury Neutrino Observatory”. In: *Phys. Rev. Lett.* 87 (7 July 2001), p. 071301. DOI: `10.1103/PhysRevLett.87.071301` (cit. on p. 4).

[Ake+19] M. Aker et al. “Improved Upper Limit on the Neutrino Mass from a Direct Kinematic Method by KATRIN”. In: *Phys. Rev. Lett.* 123 (22 Nov. 2019), p. 221802. DOI: `10.1103/PhysRevLett.123.221802` (cit. on pp. 1, 5, 8, 14, 17, 78, 95).

[Ake+20] Aker, M. et al. “Suppression of Penning discharges between the KATRIN spectrometers”. In: *Eur. Phys. J. C* 80.9 (2020), p. 821. DOI: `10.1140/epjc/s10052-020-8278-y` (cit. on p. 8).

[Ale20] Alexey Lokhov for the SAP team. *SAP measurements in KNM3*. Internal document. WWU Münster. June 9, 2020. URL: `https://ikp-katrin-wiki.ikp.kit.edu/katrin/images/d/df/2020-06-09-SAP_analysis_short_report.pdf` (cit. on p. 61).

[Alt+19] K. Altenmüller et al. “Muon-induced background in the KATRIN main spectrometer”. In: *Astroparticle Physics* 108 (2019), pp. 40–49. ISSN: 0927-6505. DOI: `10.1016/j.astropartphys.2019.01.003` (cit. on p. 17).

[Ams+15] J.F. Amsbaugh et al. “Focal-plane detector system for the KATRIN experiment”. In: *Nuclear Instruments and Methods in Physics Research Section A: Accelerators, Spectrometers, Detectors and Associated Equipment* 778 (2015), pp. 40–60. ISSN: 0168-9002. DOI: `https://doi.org/10.1016/j.nima.2014.12.116`. URL: `https://arxiv.org/abs/1404.2925` (cit. on pp. 8, 24, 26, 49).

[Ann19] Anna Schaller. *Background peak at 18 keV*. Internal document. TU München. Mar. 26, 2019. URL: `https://ikp-katrin-wiki.ikp.kit.edu/katrin/images/0/07/Background_peak_at_18_kV.pdf` (cit. on p. 52).

[Are+16] M. Arenz et al. "Commissioning of the vacuum system of the KATRIN Main Spectrometer". In: *Journal of Instrumentation* 11.04 (Apr. 2016), P04011–P04011. DOI: `10.1088/1748-0221/11/04/p04011` (cit. on p. 14).

[Are+18] M. Arenz et al. "The KATRIN superconducting magnets: overview and first performance results". In: *Journal of Instrumentation* 13.08 (Aug. 2018), T08005–T08005. DOI: `10.1088/1748-0221/13/08/t08005` (cit. on p. 7).

[Arn+03] C. Arnaboldi et al. "Bolometric Bounds on the Antineutrino Mass". In: *Phys. Rev. Lett.* 91 (16 Oct. 2003), p. 161802. DOI: `10.1103/PhysRevLett.91.161802` (cit. on p. 5).

[Ase+11] V. N. Aseev et al. "Upper limit on the electron antineutrino mass from the Troitsk experiment". In: *Phys. Rev. D* 84 (11 Dec. 2011), p. 112003. DOI: `10.1103/PhysRevD.84.112003` (cit. on p. 5).

[BA72] E.H.S. Burhop and W.N. Asaad. "The Auger Effect". In: Advances in Atomic and Molecular Physics 8 (1972). Ed. by D.R. Bates and Immanuel Esterman, pp. 163–284. ISSN: 0065-2199. DOI: `https://doi.org/10.1016/S0065-2199(08)60021-4` (cit. on p. 19).

[Bar97] Herbert Barth. "Bestimmmung einer Obergrenze für die Masse des Elektron-Antineutrinos aus dem Tritium-β-Zerfall". German. PhD thesis. Karlsruher Institut für Technologie (KIT), 1997 (cit. on pp. 24, 25).

[BD76] John N. Bahcall and Raymond Davis. "Solar Neutrinos: A Scientific Puzzle". In: *Science* 191.4224 (1976), pp. 264–267. ISSN: 0036-8075. DOI: `10.1126/science.191.4224.264` (cit. on p. 4).

[Beh+17] Behrens, J. et al. "A pulsed, mono-energetic and angular-selective UV photo-electron source for the commissioning of the KATRIN experiment". In: *Eur. Phys. J. C* 77.6 (2017), p. 410. DOI: `10.1140/epjc/s10052-017-4972-9` (cit. on p. 6).

[Bie17] Benedikt Bieringer. "Designing and optimizing the UV illumination of the rear wall at the KATRIN experiment by simulation". Bachelor's thesis. WWU, Münster, 2017 (cit. on p. 6).

[Bot12] Richard Bottesch. “Set-up of the motion control and characterization of the ablation laser for the condensed 83mKr conversion electron source of the KATRIN experiment”. PhD thesis. 2012 (cit. on p. 7).

[Cam20] L. et al Campagnola. *PyQtGraph. Scientific Graphics and GUI Library for Python.* Version 0.11.0. June 9, 2020. URL: `https://www.pyqtgraph.org` (cit. on p. 37).

[CC BY 3.0] *Creative Commons Attribution 3.0 Unported License.* Creative Commons. URL: `http://creativecommons.org/licenses/by/3.0/` (cit. on pp. 7, 18, 20).

[CC BY-SA 4.0] *Creative Commons Attribution-ShareAlike 4.0 International License.* Creative Commons. URL: `http://creativecommons.org/licenses/by-sa/4.0/` (cit. on p. 22).

[Cor14] Thomas Corona. “Methodology and Application of High Performance Electrostatic Field Simulation In the Katrin Experiment”. PhD thesis. 2014. DOI: `10.17615/gts6-gp54` (cit. on p. 8).

[Cow+56] C. L. Cowan et al. “Detection of the Free Neutrino: a Confirmation”. In: *Science* 124.3212 (1956), pp. 103–104. ISSN: 0036-8075. DOI: `10.1126/science.124.3212.103` (cit. on pp. 1, 3).

[Dan+62] Gaillard Danby et al. “Observation of high-energy neutrino reactions and the existence of two kinds of neutrinos”. In: *Physical Review Letters* 9.1 (1962), p. 36 (cit. on p. 4).

[Ell19] Enrico Ellinger. “Development and investigation of the Forward Beam Monitor for the KATRIN experiment”. PhD thesis. 2019. DOI: `10.25926/r160-7a40` (cit. on p. 7).

[Esf+17] Ali Ashtari Esfahani et al. “Determining the neutrino mass with cyclotron radiation emission spectroscopy—Project 8”. In: *Journal of Physics G: Nuclear and Particle Physics* 44.5 (Mar. 2017), p. 054004. DOI: `10.1088/1361-6471/aa5b4f` (cit. on p. 5).

[Fla01] Björn Flatt. “Designstudien für das KATRIN-Experiment”. German. MA thesis. Johannes Gutenberg-Universität Mainz, 2001 (cit. on p. 33).

[For14] J.A. Formaggio. “Direct neutrino mass measurements after PLANCK”. In: *Physics of the Dark Universe* 4 (2014). DARK TAUP2013, pp. 75–80. ISSN: 2212-6864. DOI: `10.1016/j.dark.2014.10.004` (cit. on p. 5).

[Frä+11] F.M. Fränkle et al. “Radon induced background processes in the KATRIN pre-spectrometer”. In: *Astroparticle Physics* 35.3 (2011), pp. 128–134. ISSN: 0927-6505. DOI: `10.1016/j.astropartphys.2011.06.009` (cit. on p. 18).

[Fre74] M S Freedman. “Atomic Structure Effects in Nuclear Events”. In: *Annual Review of Nuclear Science* 24.1 (1974), pp. 209–248. DOI: `10.1146/annurev.ns.24.120174.001233` (cit. on pp. 19, 20).

[FS03] Y. Farzan and A.Yu. Smirnov. “On the effective mass of the electron neutrino in beta decay”. In: *Physics Letters B* 557.3 (2003), pp. 224–232. ISSN: 0370-2693. DOI: `https://doi.org/10.1016/S0370-2693(03)00207-7` (cit. on p. 5).

[Fuk+98] Y. Fukuda et al. “Evidence for Oscillation of Atmospheric Neutrinos”. In: *Phys. Rev. Lett.* 81 (8 Aug. 1998), pp. 1562–1567. DOI: `10.1103/PhysRevLett.81.1562` (cit. on p. 4).

[Ful+] Alexander Fulst et al. “Time-Focusing Time-of-Flight, a new method to turn a MAC-E-filter into a quasi-differential spectrometer”. arXiv: `2007.01020` (cit. on p. 30).

[FUL18] Alexander FULST. *The Condensed Krypton Source (CKrS) as Calibration Tool for KATRIN.* June 2018. DOI: `10.5281/zenodo.1300532` (cit. on p. 7).

[Fur+17] Daniel Furse et al. “Kassiopeia: a modern, extensible C++ particle tracking package”. In: *New Journal of Physics* 19.5 (May 2017), p. 053012. DOI: `10.1088/1367-2630/aa6950` (cit. on p. 32).

[Gil20] Woosik Gil. *Internal document: eLFCS_inputfile_Magfield3_Rev2_20200515.pdf.* 2020 (cit. on p. 14).

[Glü+13] Ferenc Glück et al. “Electromagnetic design of the large-volume air coil system of the KATRIN experiment”. In: *New Journal of Physics* 15.8 (Aug. 2013), p. 083025. DOI: `10.1088/1367-2630/15/8/083025` (cit. on pp. 13, 14, 32, 39, 40).

[Glü11a] Ferenc Glück. “Axisymmetric Electric Field Calculation with Zonal Harmonic Expansion”. In: *Progress In Electromagnetics Research B* 32 (2011), pp. 319–350. DOI: `10.2528/pierb11042106` (cit. on p. 35).

[Glü11b] Ferenc Glück. “Axisymmetric Magnetic Field Calculation with Zonal Harmonic Expansion”. In: *Progress In Electromagnetics Research B* 32 (2011), pp. 351–388. DOI: `10.2528/pierb11042108` (cit. on p. 35).

[Gör14] Stefan Görhardt. “Background Reduction Methods and Vacuum Technology at the KATRIN Spectrometers”. 51.02.01; LK 01. PhD thesis. 2014. DOI: `10.5445/IR/1000038050` (cit. on p. 21).

[Gri12] David J. Griffiths. *Introduction to Electrodynamics (4th Edition)*. Pearson, Oct. 2012. ISBN: 9780321856562 (cit. on p. 35).

[Har12] Fabian Harms. “Assembly and First Results of the KATRIN Focal-Plane Detector System at KIT”. Diploma thesis. KIT, Karlsruhe, 2012 (cit. on p. 8).

[Har15] Fabian Thomas Harms. “Characterization and Minimization of Background Processes in the KATRIN Main Spectrometer”. 51.03.01; LK 01. PhD thesis. 2015. DOI: `10.5445/IR/1000050027` (cit. on p. 19).

[HH76] T. Hsu and J. L. Hirshfield. “Electrostatic energy analyzer using a nonuniform axial magnetic field”. In: *Review of Scientific Instruments* 47.2 (1976), pp. 236–238. DOI: `10.1063/1.1134594` (cit. on p. 9).

[HK17] Florian Heizmann and Hendrik Seitz-Moskaliuk for the KATRIN collaboration. “The Windowless Gaseous Tritium Source (WGTS) of the KATRIN experiment”. In: *Journal of Physics: Conference Series* 888 (Sept. 2017), p. 012071. DOI: `10.1088/1742-6596/888/1/012071` (cit. on p. 6).

[Hug08] Karen Hugenberg. “Design of the electrode system for the KATRIN main spectrometer”. PhD thesis. 2008 (cit. on p. 14).

[Hun07] J. D. Hunter. “Matplotlib: A 2D graphics environment”. In: *Computing in Science & Engineering* 9.3 (2007), pp. 90–95. DOI: `10.1109/MCSE.2007.55` (cit. on p. 50).

[Jac99] John David Jackson. *Classical electrodynamics; 3rd ed.* New York, NY: Wiley, 1999. URL: `http://cds.cern.ch/record/490457` (cit. on p. 11).

[Jan15] Alexander Jansen. “The Cryogenic Pumping Section of the KATRIN Experiment - Design Studies and Experiments for the Commissioning”. PhD thesis. 2015. DOI: `10.5445/IR/1000047146` (cit. on p. 7).

[KAT05] KATRIN Collaboration. *KATRIN design report 2004*. Tech. rep. 51.54.01; LK 01. Forschungszentrum, Karlsruhe, 2005. 245 pp. DOI: `10.5445/IR/270060419` (cit. on pp. 1, 3, 6, 8, 17).

[KAT17] F.M. Fraenkle for the KATRIN collaboration. “Background processes in the KATRIN main spectrometer”. In: *Journal of Physics: Conference Series* 888 (Sept. 2017), p. 012070. DOI: `10.1088/1742-6596/888/1/012070` (cit. on p. 18).

[Kir20] Rebecca Kirchgässner. “Simulations and characteristics of radon-induced background in the KATRIN main spectrometer”. German. Bachelor’s thesis. KIT, Karlsruhe, 2020 (cit. on pp. 20, 28).

[Kle+19] M Kleesiek et al. “β-Decay spectrum, response function and statistical model for neutrino mass measurements with the KATRIN experiment”. In: *The European Physical Journal C* 79.3 (2019), pp. 1–24 (cit. on pp. 6, 10, 11, 13).

[Kle14] Marco Kleesiek. “A Data-Analysis and Sensitivity-Optimization Framework for the KATRIN Experiment”. PhD thesis. 2014. DOI: `10.5445/IR/1000043301` (cit. on p. 49).

[Kra+05] Kraus, Ch et al. “Final results from phase II of the Mainz neutrino mass search in tritium β decay”. In: *Eur. Phys. J. C* 40.4 (2005), pp. 447–468. DOI: `10.1140/epjc/s2005-02139-7` (cit. on p. 5).

[Kra88] Kenneth S Krane. *Introductory nuclear physics.* New York, NY: Wiley, 1988. ISBN: 047180553X. URL: `https://cds.cern.ch/record/359790` (cit. on p. 19).

[KT73] C A Kapetonakos and A W Trivelpiece. “Numerical studies of charged particle trapping in a time varying magnetic mirror field”. In: *Plasma Physics* 15.4 (Apr. 1973), pp. 317–322. DOI: `10.1088/0032-1028/15/4/007` (cit. on p. 28).

[LS85] V.M. Lobashev and P.E. Spivak. “A method for measuring the electron antineutrino rest mass”. In: *Nuclear Instruments and Methods in Physics Research Section A: Accelerators, Spectrometers, Detectors and Associated Equipment* 240.2 (1985), pp. 305–310. ISSN: 0168-9002. DOI: `https://doi.org/10.1016/0168-9002(85)90640-0` (cit. on p. 9).

[Mer+13] S. Mertens et al. “Background due to stored electrons following nuclear decays in the KATRIN spectrometers and its impact on the neutrino mass sensitivity”. In: *Astroparticle Physics* 41 (2013), pp. 52–62. ISSN: 0927-6505. DOI: `10.1016/j.astropartphys.2012.10.005` (cit. on pp. 18, 21).

[Mer12] Susanne Mertens. “Study of Background Processes in the Electrostatic Spectrometers of the KATRIN Experiment”. PhD thesis. 2012. DOI: `10.5445/IR/1000027058` (cit. on pp. 8, 19).

[MN11] José Luis Morales and Jorge Nocedal. “Remark on “Algorithm 778: L-BFGS-B: Fortran Subroutines for Large-Scale Bound Constrained Optimization””. In: *ACM Trans. Math. Softw.* 38.1 (Dec. 2011). ISSN: 0098-3500. DOI: `10.1145/2049662.2049669` (cit. on p. 63).

[MNS62] Ziro Maki, Masami Nakagawa, and Shoichi Sakata. “Remarks on the Unified Model of Elementary Particles”. In: *Progress of Theoretical Physics* 28.5 (Nov. 1962), pp. 870–880. ISSN: 0033-068X. DOI: `10.1143/PTP.28.870` (cit. on p. 4).

[Nob1515] *The Nobel Prize in Physics 2015.* Press release. Nobel Media AB. Oct. 6, 2015. URL: `https://www.nobelprize.org/prizes/physics/2015/press-release/` (cit. on p. 1).

[Nor63] Theodore G. Northrop. “Adiabatic charged-particle motion”. In: *Reviews of Geophysics* 1.3 (1963), pp. 283–304. DOI: `10.1029/RG001i003p00283` (cit. on p. 31).

[Pau30] Wolfgang Pauli. *Pauli letter collection: letter to Lise Meitner.* Typed copy. 1930. URL: `http://cds.cern.ch/record/83282` (cit. on p. 3).

[Pic+92] A. Picard et al. “A solenoid retarding spectrometer with high resolution and transmission for keV electrons”. In: *Nuclear Instruments and Methods in Physics Research Section B: Beam Interactions with Materials and Atoms* 63.3 (1992), pp. 345–358. ISSN: 0168-583X. DOI: `https://doi.org/10.1016/0168-583X(92)95119-C` (cit. on p. 9).

[Pon57] B. Pontecorvo. “Mesonium and anti-mesonium”. In: *Sov. Phys. JETP* 6 (1957), p. 429 (cit. on p. 4).

[Pra+12] M Prall et al. “The KATRIN pre-spectrometer at reduced filter energy”. In: *New Journal of Physics* 14.7 (July 2012), p. 073054. DOI: `10.1088/1367-2630/14/7/073054` (cit. on p. 31).

[PyQ20] PyQT5. *PyQt5 Reference Guide.* Version 5.15.0. 2020. URL: `http://www.riverbankcomputing.com/static/Docs/PyQt5/` (cit. on p. 37).

[RAP75a] M. S. Rapaport, F. Asaro, and I. Perlman. “K-shell electron shake-off accompanying alpha decay”. In: *Phys. Rev. C* 11 (5 May 1975), pp. 1740–1745. DOI: `10.1103/PhysRevC.11.1740` (cit. on p. 19).

[RAP75b] M. S. Rapaport, F. Asaro, and I. Perlman. “L- and M-shell electron shake-off accompanying alpha decay”. In: *Phys. Rev. C* 11 (5 May 1975), pp. 1746–1754. DOI: `10.1103/PhysRevC.11.1746` (cit. on p. 19).

[Rei09] Jan Reich. “Magnetfeldmessungen und Designarbeiten für das EMCS Luftspulensystem am KATRIN Hauptspektrometer”. German. Diploma thesis. Universität Karlsruhe (TH), 2009 (cit. on p. 32).

[Rei13] Jan Christoph Reich. “Magnetic Field Inhomogeneities and Their Influence on Transmission and Background at the KATRIN Main Spectrometer”. PhD thesis. 2013. DOI: `10.5445/IR/1000033076` (cit. on p. 32).

[San19] Sanshiro Enomoto. *Veto, Event Multiplicity, ROI.* Internal document. University of Washington. Oct. 1, 2019. URL: `https://ikp-katrin-wiki.ikp.kit.edu/katrin/images/2/2d/20191001v2-Knm2VetoMpcRoi.pdf` (cit. on p. 52).

[Sch16] Kerstin Schönung. “Development of a Rear Wall for the KATRIN Rear Section and investigation of tritium compatibility of Rear Section components”. PhD thesis. Karlsruher Institut für Technologie (KIT), 2016. 336 pp. DOI: `10.5445/IR/1000056077` (cit. on p. 6).

[Sin+13] Balraj Singh et al. “Nuclear Data Sheets for A = 215”. In: *Nuclear Data Sheets* 114.12 (2013), pp. 2023–2078. ISSN: 0090-3752. DOI: `10.1016/j.nds.2013.11.003` (cit. on p. 19).

[Ste+13] Nicholas Steinbrink et al. “Neutrino mass sensitivity by MAC-E-Filter based time-of-flight spectroscopy with the example of KATRIN”. In: *New Journal of Physics* 15.11 (Nov. 2013), p. 113020. DOI: `10.1088/1367-2630/15/11/113020` (cit. on p. 30).

[Tan+18] M. Tanabashi et al. “Review of Particle Physics”. In: *Phys. Rev. D* 98.3 (2018), p. 030001. DOI: `10.1103/PhysRevD.98.030001` (cit. on pp. 4, 5).

[Thé+15] Erwan Thébault et al. “International Geomagnetic Reference Field: the 12th generation”. In: *Earth, Planets and Space* 67.1 (May 2015). Accessed via `https://www.ngdc.noaa.gov/geomag/calculators/magcalc.shtml?#igrfwmm`. DOI: `10.1186/s40623-015-0228-9` (cit. on p. 32).

[Tro19] Nikolaus Rainer-Maria Trost. “Modeling and measurement of Rydberg-State mediated Background at the KATRIN Main Spectrometer”. 51.03.01; LK 01. PhD thesis. Karlsruher Institut für Technologie (KIT), 2019. 178 pp. DOI: `10.5445/IR/1000090450` (cit. on p. 22).

[Val09] Kathrin Valerius. “Spectrometer-related background processes and their suppression in the KATRIN experiment”. PhD thesis. Munster U., 2009 (cit. on p. 8).

[Val10a] K. Valerius. “The wire electrode system for the KATRIN main spectrometer”. In: *Progress in Particle and Nuclear Physics* 64.2 (2010). Neutrinos in Cosmology, in Astro, Particle and Nuclear Physics, pp. 291–293. ISSN: 0146-6410. DOI: `10.1016/j.ppnp.2009.12.032` (cit. on p. 14).

[Val10b] Kathrin Valerius. “Spektrometeruntergrund und seine Unterdrückung beim KATRIN Experiment”. PhD thesis. 2010. URL: `http://nbn-resolving.de/urn:nbn:de:hbz:6-28479494638` (cit. on p. 40).

[VCV11] Stefan Van Der Walt, S Chris Colbert, and Gael Varoquaux. “The NumPy array: a structure for efficient numerical computation”. In: *Computing in Science & Engineering* 13.2 (2011), p. 22 (cit. on p. 34).

[VD09] Guido Van Rossum and Fred L. Drake. *Python 3 Reference Manual.* Scotts Valley, CA: CreateSpace, 2009. ISBN: 1441412697 (cit. on pp. 34, 37).

[Vir+20] Pauli Virtanen et al. “SciPy 1.0: Fundamental Algorithms for Scientific Computing in Python”. In: *Nature Methods* 17 (2020), pp. 261–272. DOI: `10.1038/s41592-019-0686-2` (cit. on p. 63).

[Wan+13] N Wandkowsky et al. “Modeling of electron emission processes accompanying radon-α-decays within electrostatic spectrometers”. In: *New Journal of Physics* 15.8 (Aug. 2013), p. 083040. DOI: `10.1088/1367-2630/15/8/083040` (cit. on pp. 18–20).

[WKM06] Qi Wei, Sabre Kais, and Nimrod Moiseyev. “New stable multiply charged negative atomic ions in linearly polarized superintense laser fields”. In: *The Journal of Chemical Physics* 124.20 (2006), p. 201108. DOI: `10.1063/1.2207619` (cit. on p. 20).

[WOL09] Joachim WOLF. “Size Matters: The Vacuum System of the KATRIN Neutrino Experiment”. In: *Journal of the Vacuum Society of Japan* 52.5 (2009), pp. 278–284. DOI: `10.3131/jvsj2.52.278` (cit. on p. 22).

[Wu07] S.-C. Wu. “Nuclear Data Sheets for A = 216”. In: *Nuclear Data Sheets* 108.5 (2007), pp. 1057–1092. ISSN: 0090-3752. DOI: `10.1016/j.nds.2007.04.001` (cit. on p. 19).

[Zac15] Michael Zacher. “High-field electrodes design andan angular-selective photoelectron sourcefor the KATRIN spectrometers”. PhD thesis. 2015 (cit. on p. 12).

Acknowledgements

During the work on this thesis, I experienced support from many people. The following is the result of my attempt to unsystematically thank those who were most involved:

Christian Weinheimer for providing the ability to work on this topic in his lively group, his guidance, active engagement in physics discussions, his willingness to discuss open questions in nearly any thinkable situation and his general support.

Anton Andronic for agreeing to referee this thesis and previously providing extensive introduction to gas detectors, which became of frequent use to me.

Alexey Lokhov for extensive and interesting physics discussions, be it to review a simulation or to give insights into a topic, his guidance and for countless physics motivated fun moments that often enough led to actual findings.

Ferenc Glück for explaining, providing and writing simulation code, enabling and extending the use of highly efficient zonal harmonics simulations in this thesis, and for providing insights into MAC-E filter setting design, both theoretically and practically in the control room.

The KNM1 and KNM2 on-shift SAP teams for intense physics discussions and intense support in the control room, e.g. by providing near-time analysis. It was an amazing experience to participate.

Stephan Dyba for providing knowledge from former SAP measurements and introducing many design specifics in hardware and control, avoiding much potential for confusion.

The entire SAP and Background teams and the KATRIN collaboration for measurement and inspection of SAP settings, valuable remarks, the ability to use their data and the ability to participate.

Sanshiro Enomoto, Jan Behrens and Alexander Fulst for insights into and discussions about the `Kasper` simulation software and scientific code in general.

My office 213 and the KATRIN Münster group for the comfortable though fun work atmosphere.

Alexey Lokhov, Sonja Schneidewind and Kevin Gauda for their support in reviewing this thesis.

Volker Hannen for his general organization, physics input and always being able to give orientation in the organization of our university.

Lutz Althüser for being available for discussions as non-KATRIN physicist and scientific programmer, his insights in scientific procedures in general and for providing the LaTeX template used as base of this document.

My family and friends for their great support and motivation, and for just being there. All of that is absolutely invaluable.

It is impossible for this list to be complete because of the supportive and friendly atmosphere in the KATRIN collaboration and in both the working group of Christian Weinheimer and the entire IKP. Examples of manifestations of which include bouldering with KATRIN members, random rambling during a Collaboration Dinner with e.g. Kathrin Valerius about the beauty of telescope experiments and Sanshiro Enomoto about a combination of bouldering and design decisions in software, and relaxed evenings with members of the KATRIN experiment, the institute and the working group. Further, the possibility to travel to e.g. the amazing Astroparticle School in Obertrubach, the large DPG Frühjahrstagung, an informative and fun GRK Retreat and of course the KATRIN experiment provided a huge value for me personally.